Fall 2014

Efficient and coherent frequency conversions and nonlinear interference in optical parametric and atomic Raman processes

Yu Ding
Purdue University

Graduate School Form 30
(Updated 11/20/2014)

PURDUE UNIVERSITY
GRADUATE SCHOOL
Thesis/Dissertation Acceptance

This is to certify that the thesis/dissertation prepared

By Yu Ding

Entitled
EFFICIENT AND COHERENT FREQUENCY CONVERSIONS AND NONLINEAR INTERFERENCE IN OPTICAL PARAMETRIC AND ATOMIC RAMAN PROCESSES

For the degree of Doctor of Philosophy

Is approved by the final examining committee:

Zhe-Yu Jeff Ou

Sergei Savikhin

Ricardo Decca

Gautam Vemuri

Marvin D. Kemple

To the best of my knowledge and as understood by the student in the Thesis/Dissertation Agreement, Publication Delay, and Certification/Disclaimer (Graduate School Form 32), this thesis/dissertation adheres to the provisions of Purdue University's "Policy on Integrity in Research" and the use of copyrighted material.

Zhe-Yu Jeff Ou

Approved by Major Professor(s): _____

_____

Approved by: Ricardo Decca 11/21/2014

Head of the Department Graduate Program Date

EFFICIENT AND COHERENT FREQUENCY CONVERSIONS AND NONLINEAR INTERFERENCE IN OPTICAL PARAMETRIC AND ATOMIC RAMAN PROCESSES

A Dissertation

Submitted to the Faculty

of

Purdue University

by

Yu Ding

In Partial Fulfillment of the

Requirements for the Degree

of

Doctor of Philosophy

December 2014

Purdue University

West Lafayette, Indiana

TABLE OF CONTENTS

LIST OF FIGURES

Figure Page

Figure Page

Figure Page

ABSTRACT

Ding,Yu Ph.D., Purdue University, December 2014. Efficient and coherent frequency conversions and nonlinear interference in optical parametric and atomic Raman processes. Major Professor: Zhe-Yu Jeff Ou.

By implementing a parametric down-conversion process with a strong signal field injection, we demonstrate that frequency down-conversion from pump photons to idler photons can be a coherent process. Contrary to a common misconception, we show that the process can be free of quantum noise. With an interference experiment, we demonstrate that coherence is preserved in the conversion process. This technique could lead to a high-fidelity quantum state transfer from a high-frequency photon to a low-frequency photon and connect a missing link in quantum networks.

Coherent and efficient nonlinear interaction and frequency conversion are of great interest in many areas of quantum optics. Traditionally, the low efficiency of Raman scattering is improved by a high-finesse optical resonator or stimulated Raman conversion. It was recently found that the atomic spin wave initially built through electromagnetically induced transparency or a weak Raman process can actively enhance the Raman frequency conversion. An experimental demonstration of an efficient Raman conversion scheme with coherent feedback of both pump and Stokes fields is presented. The temporal profile of the generated Raman pulse shows that the coherence time of the atomic spin wave is $\sim$1.8 ms. A laser-like power threshold is observed and its low threshold is attributed to the long coherence time of the atomic spin wave. The mechanism of the conversion enhancement process is discussed and the conversion efficiency of a single pass of the beams is compared with that of double passes. Finally, a beat signal is observed between the two Stokes fields and its Fourier transform shows that the frequency difference is caused by the AC Stark effect.

Precision phase measurement is traditionally restricted by the standard quantum limit. However, this limit is not as fundamental as the Heisenberg limit and can be circumvented by use of nonclassical quantum states and structure modification of the interferometers. Several examples of nonlinear interferometers are proposed and implemented. The wave propagation equations for the nonlinear interferometers are solved. The interference fringes are measured and compared with that of linear interferometers. The first nonlinear interferometer presented is based on second harmonic generation and degenerate parametric down-conversion. The second nonlinear interferometer is composed of two parametric amplifiers. The idea of nonlinear beam splitters is introduced as an analogy to traditional beam splitters. We show that a nonlinear interferometer can be built alternatively by using only one parametric amplifier. Type II phase-matched crystals can be used to increase the amplification factor. An interferometer based on a Raman amplifier is analyzed for its application to sensitive magnetic field measurement.

1. INTRODUCTION

In past decades, a broad range of discoveries have been made in the field of quantum information science [1]. These advances include both theoretical analysis and physical implementations in areas of quantum computing, quantum communication and metrology [2].

A general quantum network was proposed that consists of spatially separated nodes and quantum communication channels that connect the nodes [3]. A notional picture of a quantum network is shown in Figure1.1. In such a network, quantum information is stored and processed locally in the nodes. These nodes are linked by quantum channels, which transport quantum states among the nodes. The nodes can also serve as quantum repeaters to preserve coherence and increase the fidelity of quantum states over long distance transmission. Quantum networks could accomplish tasks that are impossible in classical networks. Moreover, such quantum systems are potential simulators of quantum many-body systems and can be used to test the fundamental laws of quantum mechanics [4].

In physical implementation of such a network, atoms are suited for storing and processing information as a quantum memory, while photons are good at transmitting information. Quantum information is constantly transferred between photons and atoms, and transmitted between atoms via photons. Because quantum information is susceptible to environmental losses, minimizing losses is crucial to successfully set up the network. However, in current technology, atoms interact best with photons of wavelength around $0.8\mu m$, whereas optical telecommunication systems have low losses at wavelength $1.6\mu m$. So there is a mismatch between the atomic transition wavelength and the optical transmission wavelength. As a result, it is required to convert photons from one wavelength to another in order to accomplish the quantum network.

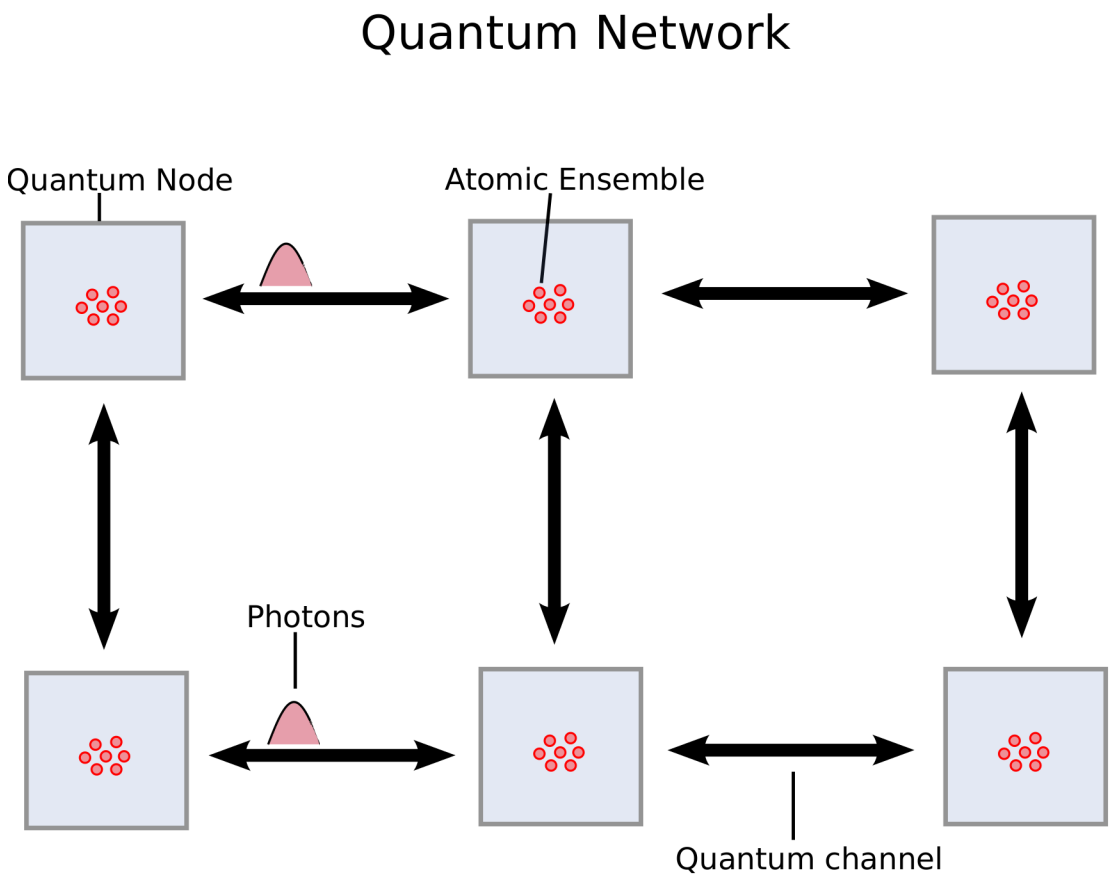

Figure 1.1. A quantum network comprises quantum nodes that store and process quantum information and quantum channels that transmit quantum information. Photons are good quantum information carriers for transmission. Atoms are used to store and process quantum information locally.

Quantum information transfer between photons and atoms was realized in frequency up-conversion process years ago [5–7]. However, a lossless frequency down-conversion process has not been reported. Currently, research in this field focuses on up-converting photons from the telecommunication wavelength $1.6\mu m$ to its half wavelength (double frequency) $0.8\mu m$. This is because detectors for photon counting at $1.6\mu m$ are much noisier than those at $0.8\mu m$. Moreover, it is believed that the quantum noise caused by spontaneous emission is unavoidable in a parametric down-conversion process. As a result, it is believed that a high-fidelity transfer of quantum states is impossible in a frequency down-conversion process.

Therefore, frequency down-conversion seems to be the missing link in this quantum network. Contrary to the common misunderstanding, we demonstrate in this thesis that a noise-free photon frequency down-conversion is achievable. A proof-of-principle experiment is implemented.

In such a quantum network, parametric up-conversion and down-conversion provide links between a high-frequency photon and a low-frequency photon. These photons are transmitted in quantum channels and can carry quantum information which can be mapped to atoms in the quantum nodes. This mapping requires strong interactions between photons and atoms. Currently, many physical systems are being investigated [8], out of which two research areas are explored actively: cavity quantum electrodynamics (CQED) [9] and atomic spin waves in atomic ensembles [10].

In the CQED method, it is critical to have a strong coupling between single atoms and single photons. Trapping and coherent controlling of single atoms in a tiny optical resonator add a tremendous amount of complexity to the experiment. On the other hand, the atomic spin wave method only requires coherent laser passages through atomic ensembles, which can be contained in a glass vapor cell that is at a much larger scale (order of magnitude in centimeters, as in contrast to micrometers in the CQED method). Because it is relatively easy to prepare and control the system in such a method, most practical quantum network schemes are based on the atomic spin wave method. It was demonstrated that a quantum state can be transferred from

photons to atoms and later retrieved in atomic ensembles [11]. Collective atomic qubits, entangled states between photons and atomic spin waves, and between two atomic spin waves have all been successfully demonstrated [12].

An atomic spin wave can be created through the method of Electromagnetically Induced Transparency (EIT), or a weak Raman process. However, the efficiency of Raman conversion is usually quite low. Traditionally, the conversion efficiency could be improved by using a high-finesse optical resonator allowing the light beam to pass through the Raman medium multiple times. The efficiency can also be improved with a stimulated Raman process by deliberately seeding the system with some initial Stokes field. The seeding field can be a weak Stokes field initially generated by spontaneous Raman scattering or injected from another laser source. In these methods, the atoms in the Raman medium only play a passive role in the Raman conversion process. Recently, it has been discovered that Raman conversion can be greatly enhanced by using the atomic coherence in an atomic ensemble. The atomic spin wave is created before the Raman process and acts as a seed to actively enhance the Raman conversion. High frequency conversion efficiency is achieved with the help of an atomic coherence prepared via EIT [46]. High Raman conversion efficiency is also reported with the help of atomic spin wave created by another Raman laser in Rb-87 vapor cell [47].

We show an experimental demonstration of efficient Raman conversion with a coherent feedback of both the pump field and the Stokes field. Our atomic system is based on diluted cesium-133 gas inside a paraffin-coated glass vapor cell. Atomic spin wave is initially created by the Raman process in the first passage of the pump beam. The atomic spin wave acts as a seed to coherently enhance the Raman amplification process in the second passage of the pump beam and the Stokes beam. The high Raman conversion efficiency with a relatively simple experimental setup could lead to many applications in the areas of quantum optics and nonlinear optics.

Quantum metrology is the study of highly precise measurement of physical quantities taking advantage of quantum mechanics theories. Precise interferometric phase

measurement is of particular interest because of its potential application to gravitational wave detection. Classically, the precision of an interferometric phase measurement is limited by the so-called Standard Quantum Limit (SQL). This limit can be circumvented by preparing non-classical input quantum states such as squeezed states and entangled states. It has been recently found that altering interferometer structure can also improve the phase measurement precision. By replacing the traditional beam splitters with nonlinear beam splitters such as parametric amplifiers and Raman amplifiers, we can turn a traditional interferometer into a nonlinear interferometer.

In this thesis we propose and experimentally realize several nonlinear interferometers. The concept of nonlinear beam splitter (NBS) is introduced and several examples of NBS are demonstrated. Wave propagation equations are solved for the nonlinear interferometer. The results from nonlinear interferometers are compared with those of traditional interferometers in the same experimental setup. Nonlinear interferometers based on two parametric amplifiers are discussed and analyzed in detail. As a potential sensitive magnetometer, a nonlinear interferometer based on a Raman frequency conversion process is analyzed and experimental results are discussed.

The thesis is organized as follows:

In the chapter "Nonlinear Optics," a general knowledge of nonlinear optics and relevant topics are first introduced. Several examples of nonlinear processes are given, out of which second harmonic generation (SHG) is highlighted in the explanation. The wave-propagation equations of a sum frequency generation are solved. From the position-dependent equation of the generated field, we see that the phase matching condition has to be satisfied in order to have a sufficient output. Quasi-phase matching is also discussed. As a special case of nonlinear optical process, Raman scattering is introduced. Finally, a quantum mechanical description of the three-wave mixing processes is analyzed. The interaction Hamiltonian is described and the evolution equations of the operators in the Heisenberg picture are solved.

Following the chapter "Nonlinear Optics," three main experiments are described in respective chapters. The first one is a coherent frequency conversion in a parametric down-conversion process. The second is an experiment of efficient Raman conversion implemented by reflecting back the pump field and Stokes field to the atomic spin wave created in the first passage. Third, several schemes of nonlinear interferometers are implemented for precision phase measurement. In each chapter, a research background is first given. Experimental procedures and results are then explained. They are followed by discussions of possible improvement for the experiment and potential applications.

2. NONLINEAR OPTICS

Before the invention of the first laser in 1960, it was perceived that the optical response of a medium to passing light was linear and the wavelength of light remained unchanged before and after it passed through a medium. One light beam would never interact with or alter the wavelengths of other light beams in the same medium.

It was not until 1961, when Franken and coworkers [13] observed second-harmonic generation, that people started to realize that optical responses of media could be nonlinearly dependent on the intensities of the passing light beams [14]. As a result, light beams passing through the same medium might interact with each other and one light beam could alter the frequencies of the others. Nonlinear effects provided methods of generating coherent radiation at wavelengths that otherwise no laser transitions could provide.

Nonlinear optical processes can be generally divided into two categories: parametric and non-parametric processes. In a parametric process, the quantum states of the media remain the same during the process of interaction. Plus, there is no direct energy transfer between the medium and the light beams. An example of a parametric process is a three-wave mixing process, which includes parametric down-conversion, parametric up-conversion and parametric amplification. On the other hand, a non-parametric process will change the quantum state as well as the energy of the medium. This thesis will focus only on parametric processes, which will be introduced and discussed in detail later in this chapter.

This chapter is organized as follows: In the first section, a mathematical formalism of nonlinear optics is introduced. Several important nonlinear effects are reviewed. Among them are second harmonic generation, sum frequency generation, difference frequency generation, and four wave mixing processes. Phase matching conditions need to be satisfied in order to have reasonable converting efficiency. The birefrigence

of a crystal is always utilized to achieve such conditions. Lastly, a technique called quasi-phase matching is introduced. This technique induces some complexity into the fabrication.

In the second section, the atomic Raman process is introduced. Some basics of atomic physics are reviewed. The quantum structure of cesium atoms, as used in our experiment, is examined.

In the third section, a quantum mechanical description of three wave mixing Process is given. It is shown that by treating the collective spin excitation as a wave mode, three wave mixing can be generalized to describe the Raman process as well.

2.1 General Formalism of Nonlinear Optics

As we know, the optical response of a medium to applied electromagnetic fields can be expressed in terms of its polarization density $\vec{P}$. In a linear dielectric medium, the polarization can be written linearly as

$$\vec{P} = \varepsilon_0 \chi \vec{E}, \tag{2.1}$$

where ε_0 is the vacuum permittivity, χ is the linear electric susceptibility, and $\vec{E}$ is the applied electric field. In a nonlinear material, since the nonlinearity is typically weak, the polarization can be expanded in a Taylor series [54–56]. By using the Einstein summation notation, a component P_i of the polarization vector can generally be written as

$$P_i = \varepsilon_0(\chi_{ij}^{(1)} E_j + \chi_{ijk}^{(2)} E_j E_k + \chi_{ijkl}^{(3)} E_j E_k E_l + ...), \tag{2.2}$$

where the indices i,j and k refer to the Cartesian components of the fields and can independently take on the values x, y and z. The electric susceptibilities are expressed in terms of tensors: $\chi^{(1)}$ is a second-rank tensor and $\chi^{(2)}$ is a third-rank tensor, etc. In Equation 2.2, the first term is the linear term and corresponds to the linear polarization $P_i^{(1)}$

$$P_i^{(1)} = \varepsilon_0 \chi_{ij}^{(1)} E_j. \tag{2.3}$$

The rest are nonlinear terms. The first nonlinear term $P_i^{(2)}$ is of particular interest here

$$P_i^{(2)} = \varepsilon_0 \chi_{ijk}^{(2)} E_j E_k. \tag{2.4}$$

2.1.1 Examples of Nonlinear Processes

In this section, we will describe some common effects of nonlinear optical processes qualitatively. We start with the most common nonlinear effect: Second-Harmonic Generation (SHG), which is also the first optical nonlinear phenomenon discovered in history.

Assume we apply an optical field with its electric component $\vec{E}$ in a medium with the nonlinear susceptibility of $\chi^{(2)}$. Without loss of generality, we set up the Cartesian coordinates in such a way that the electric field is pointing in the $\hat{z}$ direction $\vec{E} = (Ae^{-i\omega t} + c.c.)\hat{z}$. Here A is the field amplitude at a given position and *c.c.* stands for "complex conjugate." By plugging $\vec{E}$ into Equation 2.4, we can find out that the summation reduces to only one term, i.e. $j = k = z$.

$$P_i^{(2)} = \varepsilon_0 \chi_{izz}^{(2)} (A^2 e^{-i2\omega t} + c.c.) + 2\epsilon_0 \chi_{izz}^{(2)} |A|^2. \tag{2.5}$$

From the first term of Equation 2.5 we immediately see that a field with double frequency 2ω is generated. This process is thus called frequency doubling or second-harmonic generation. The second term is optical rectification. It creates a static electric field across the medium. Note that the value of $\chi_{ijk}^{(2)}$ is relatively small. Thus a high intensity input field is required in order to have reasonable frequency conversion efficiency.

Second-harmonic generation only requires one input field to generate a double frequency component. We further look into the case of two applied optical fields, $\vec{E}_1$ and $\vec{E}_2$, at the same location inside a nonlinear crystal. For simplicity, we assume

the two fields are collinear and in phase. The same principles also apply for two fields in a noncollinear fashion. The Cartesian coordinates system is set up in such a way that both electric fields are pointing in the $\hat{z}$ direction. $\vec{E}_1 = (A_1 e^{-i\omega_1 t} + c.c.)\hat{z}$. $\vec{E}_2 = (A_2 e^{-i\omega_2 t} + c.c.)\hat{z}$. The net electric field is $\vec{E}_{net} = \vec{E}_1 + \vec{E}_2$. By plugging $\vec{E}_{net}$ into Equation 2.4, we find that

$$P_i^{(2)} = \varepsilon_0 \chi_{izz}^{(2)}(A_1^2 e^{-i2\omega_1 t} + A_2^2 e^{-i2\omega_2 t} + 2A_1 A_2 e^{-i(\omega_1+\omega_2)t} + 2A_1 A_2^* e^{i(\omega_1-\omega_2)t} + c.c.) \\ +2\varepsilon_0 \chi_{izz}^{(2)}(|A_1|^2 + |A_2|^2). \tag{2.6}$$

There are five terms in the equation. The first term and second term give the second-harmonic frequencies $2\omega_1$ and $2\omega_2$ of each field. The third term generates the sum frequency $(\omega_1 + \omega_2)$ and the fourth term generates the difference frequency $(\omega_1 - \omega_2)$. The last term is optical rectification. In this equation, it seems that double frequency, sum frequency and difference frequency are all generated in the same medium. In the next section, we will show that only one of them may survive after propagation in the medium.

Explanations given so far for the nonlinear optical effects are all classical. These effects may also be understood in the language of photon absorption and emission. Second-harmonic, sum frequency and difference frequency generations are visualized in the photon-atom interaction pictures, as illustrated in Figure 2.1. In Part (a) of Figure 2.1, two photons of frequency ω are destroyed. In the mean time, a photon of frequency 2ω is simultaneously created in a single quantum-mechanical process. So it represents the frequency doubling process. In Part (b) of Figure 2.1, a photon of frequency ω_1 and a photon of frequency ω_2 are destroyed while a photon of frequency ω_3 is created. Energy conservation requires that $\omega_3 = \omega_1 + \omega_2$. Thus it is sum frequency generation. In Part (c) of Figure 2.1, a photon of frequency ω_1 is destroyed while two photons with respective frequencies of ω_2 and ω_3 are created. It represents a difference frequency generation. Part (d) of Figure 2.1 represents another nonlinear optical process, i.e. the Raman process. In this process, a Raman pump photon

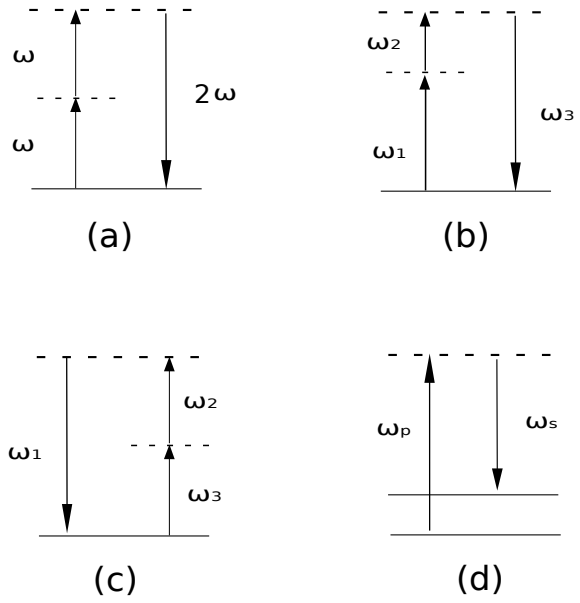

Figure 2.1. Energy-level pictures of (a)second-harmonic generation (b)sum frequency generation (c)difference frequency generation and (d)stimulated Raman process. ω_p is the Raman pump frequency and ω_s is the Stokes frequency. Dashed lines represent virtual states and solid lines represent electronic ground states.

of frequency ω_p is destroyed while a Stokes photon of frequency ω_s is created. The energy difference between the pump photon and Stokes photon goes into the vibration mode of atoms or other energy forms of the medium. The solid lines in the figure represent atomic energy states, in comparison with the dashed lines that represent virtual states. Virtual states are not real energy levels of the atoms. The lifetime of a virtual state is very short compared with that of a real energy state.

Following the same method, we can derive the equation for the third-order nonlinear polarization by plugging three input fields $\vec{E}_1, \vec{E}_2$ and $\vec{E}_3$ into Equation 2.7

$$P_i^{(3)} = \varepsilon_0 \chi_{ijkl}^{(3)} E_j E_k E_l. \tag{2.7}$$

The third-order nonlinear susceptibility $\chi^{(3)}$ is responsible for this process [15]. In general, this equation is very complicated. $\chi_{ijkl}^{(3)}$ is a fourth-rank tensor and has 81 components! However, the symmetry of the medium would reduce the number of independent terms dramatically. Naturally, one would predict that the third-order nonlinear susceptibility is much smaller than the second-order nonlinear susceptibility. Readers can find tables of $\chi^{(2)}$ and $\chi^{(3)}$ for different materials in Reference [56]. For condensed matter, a typical value of $\chi^{(2)}$ is in the order of $10^{-12} m/V$ while a typical value of $\chi^{(3)}$ is of the order of $10^{-24} m^2/V^2$.

The third-order nonlinear polarization leads to many interesting phenomena such as third harmonic generation, two-photon absorption and intensity dependent refractive index known as the optical Kerr effect [56].

2.1.2 Wave-Equation Description

From the last section, we see that under electromagnetic radiation, the nonlinear medium develops oscillating dipole moments at double frequency, sum frequency and difference frequency. These oscillating dipole moments in the medium in turn radiate, and the radiation propagates in the medium. Because there is an enormous amount of atoms in the medium, the electromagnetic waves radiated in different parts the

medium could interfere constructively if they are in phase, and destructively if they are out of phase. Furthermore, the generated sum frequency may convert back to the original frequency by a difference frequency in the subsequent nonlinear interactions in the medium. To see clearly how the waves evolve in a nonlinear medium, we mathematically derive the wave equation below.

We begin with the Maxwell's equations

$$\nabla \cdot \vec{D} = \rho \tag{2.8}$$

$$\nabla \cdot \vec{B} = 0 \tag{2.9}$$

$$\nabla \times \vec{E} = -\frac{\partial \vec{B}}{\partial t} \tag{2.10}$$

$$\nabla \times \vec{H} = \vec{J} + \frac{\partial \vec{D}}{\partial t} \tag{2.11}$$

By taking the curl of Equation 2.10 and using vector identities and substitutions, we have the wave equation

$$\nabla^2 \vec{E} - \frac{1}{\epsilon_0 c^2} \frac{\partial^2 \vec{D}}{\partial t^2} = 0 \tag{2.12}$$

Here $\vec{D} = \epsilon_0 \vec{E} + \vec{P}$. By splitting $\vec{P}$ into its linear term and nonlinear term

$$\vec{P} = \vec{P}^{(1)} + \vec{P}^{(NL)}, \tag{2.13}$$

and rewriting the electric displacement as a linear part and a nonlinear part

$$\vec{D} = \vec{D}^{(1)} + \vec{P}^{(NL)} \tag{2.14}$$

$$\vec{D}^{(1)} = \epsilon_0 \epsilon^{(1)} \vec{E}, \tag{2.15}$$

the wave equation in the nonlinear medium becomes

$$\nabla^2 \vec{E} - \frac{\epsilon_r^{(1)}}{c^2} \frac{\partial^2 \vec{E}}{\partial t^2} = \frac{1}{\epsilon_0 c^2} \frac{\partial^2 \vec{P}^{(NL)}}{\partial t^2} \tag{2.16}$$

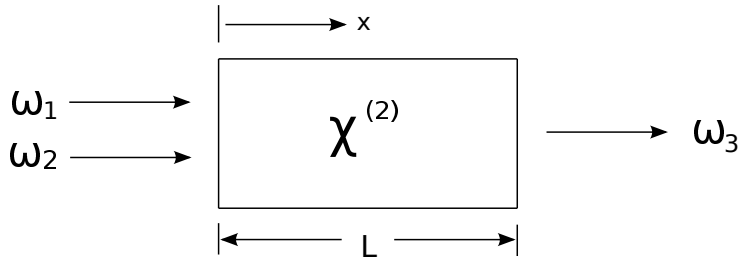

Figure 2.2. Sum frequency generation.

Here $\epsilon_r^{(1)}$ is the first order relative permittivity.

Without loss of generality, we consider a sum-frequency generation with monochromatic wave input at frequencies ω_1 and ω_2 with the waves propagating in the x direction. $\vec{E_1} = (A_1 e^{i(k_1 x - \omega_1 t)} + c.c.)\hat{r}$. $E_2 = (A_2 e^{i(k_2 x - \omega_2 t)} + c.c.)\hat{r}$. The sum frequency generated is $\omega_3 = \omega_1 + \omega_2$, as shown in Figure 2.2. With a small nonlinear effect, we expect the generated sum frequency to take the form

$$\vec{E_3}(x,t) = (A_3(x) e^{i(k_3 x - \omega_3 t)} + c.c.)\hat{r} \tag{2.17}$$

We also know from Equation 2.6,

$$\vec{P_3}(x,t) = (2\epsilon_0 \chi^{(2)}_{xxx} A_1 A_2 e^{i((k_1+k_2)x - \omega_3 t)} + c.c.)\hat{r}. \tag{2.18}$$

By plugging Equations 2.17 and 2.17 into the wave equation 2.16, and making a slowly varying amplitude approximation,

$$\frac{d^2 A_3}{dx^2} \ll |k_3 \frac{dA_3}{dx}| \tag{2.19}$$

the wave equation becomes

$$\frac{dA_3}{dx} = \frac{i\chi^{(2)}_{xxx}\omega_3^2}{k_3 c^2} A_1 A_2 e^{i\Delta k x} \tag{2.20}$$

Here $\Delta k = k_1 + k_2 - k_3$ is the phase mismatch. By repeating the same process, we derive the equations for ω_1 and ω_2.

$$\frac{dA_1}{dx} = \frac{i\chi^{(2)}_{xxx}\omega_1^2}{k_1 c^2} A_3 A_2^* e^{-i\Delta k x} \tag{2.21}$$

$$\frac{dA_2}{dx} = \frac{i\chi^{(2)}_{xxx}\omega_2^2}{k_2 c^2} A_3 A_1^* e^{-i\Delta k x} \tag{2.22}$$

Equations 2.20, 2.21 and 2.22 are a set of equations that couple the amplitudes and show the dynamics of the propagation and interactions of the three waves.

2.1.3 Phase Matching Condition

From Equation 2.6, we see that double frequency, sum frequency and difference frequency are all generated at the same time. As a matter of fact, these effects usually can not be generated from the same crystal. Only one of these frequencies may survive after considering the propagation of the waves in the crystal. The so-called phase matching condition needs to be satisfied. In other words, the relative phase between the input field and the generated field needs to be kept constant as the light propagates through the crystal. So for example, if the phase matching condition is satisfied for double frequency generation, it will not be satisfied for sum frequency and difference frequency generations, thus only double frequency survives at the output of the crystal. To see this more clearly, we include the position dependence of the optical fields in our equations. We start with one input field at angular frequency ω and wave vector $\vec{k}_\omega$ propagating in $+\hat{z}$ direction. Its electric field pointing $+\hat{x}$ direction can be written as

$$\vec{E}(z,t) = (Ae^{-i(k_\omega z - \omega t)} + c.c.)\hat{x}. \tag{2.23}$$

After plugging Equation 2.23 into Equation 2.4, we find that

$$P_i^{(2)}(z,t) = \varepsilon_0 \chi_{ixx}^{(2)}(A^2 e^{-i(2k_\omega z - 2\omega t)} + c.c.) + 2\epsilon_0 \chi_{ixx}^{(2)} A^2. \tag{2.24}$$

The second harmonic term $\epsilon_0 \chi_{ixx}^{(2)}(A^2 e^{-i(2k_\omega z - 2\omega t)} + c.c.)$ shows that at each position z, the generated second harmonic field radiates at the angular frequency 2ω. We name the wave vector of second harmonic field $k_{2\omega}$. It is straightforward that its wave vector $k_{2\omega}$ would be equal to its angular frequency multiplied by the refractive index over speed of light. That is

$$k_{2\omega} = 2\omega n_{2\omega}/c. \tag{2.25}$$

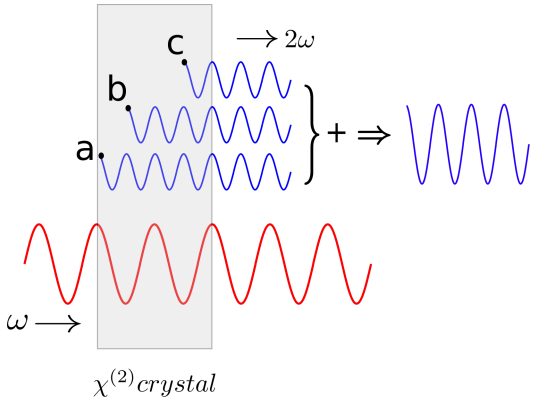

Figure 2.3. An input field at fundamental frequency (the red line) ω propagates in a $\chi^{(2)}$ crystal. Second harmonic frequency (the blue line) 2ω is generated through the medium. When the phase matching condition is satisfied, the waves of second harmonic generation at different locations propagate in phase with each other and amplitudes add constructively.

Here $n_{2\omega}$ is the refractive index of the medium for the field at frequency 2ω. c is the speed of light in vacuum. On the other hand, the same equation applies to the input field at frequency ω as well.

$$k_\omega = \omega n_\omega / c. \tag{2.26}$$

To satisfy the phase matching condition, $2k_\omega$ needs to be matched with $k_{2\omega}$, i.e. $2k_\omega = k_{2\omega}$. This is also expected from the conservation of momentum point of view, $\hbar\vec{k}_1 + \hbar\vec{k}_2 = \hbar\vec{k}_3$. In the degenerate and collinear case, it simply reduces to $2k_\omega = k_{2\omega}$. By combining Equation 2.25 and Equation 2.26 we obtain the equivalent statement of phase matching condition $n_\omega = n_{2\omega}$. On the other hand, if $2k_\omega \neq k_{2\omega}$, it is called phase mismatched.

When the phase matching condition is satisfied, second harmonic fields generated in different locations of the crystal contribute constructively and get amplified as they propagate through the crystal. For an illustrative purpose, we assume second harmonic fields are generated in three different locations a, b and c as shown in Figure 2.3. When the phase matching condition is satisfied, these three waves are in

phase as they propagate through the crystal. So the intensity of the harmonic wave would increase exponentially if we do not consider the depletion of the pump field and various losses.

Otherwise, if the phase matching condition is not satisfied, the generated second harmonics at different locations will interfere destructively, causing the direction of energy flow between ω and 2ω in the crystal to periodically change. Figure 2.4 shows the intensity of the generated second harmonic field as a function of propagation distance in the crystal. The solid line in the figure represents intensity of the second harmonic generation when the phase matching condition is satisfied. The dashed line represents the intensity of the second harmonic generation when the phases are mismatched. It shows that the energy of second harmonic generation oscillates at low amplitude.

To satisfy the phase matching condition in second harmonic generation, we know from previous analysis that $n_{2\omega}$ has to be equal to n_ω. However, in the spectrum of optical waves (with the exception at near resonance frequency), most materials have normal dispersion, i.e., the refractive index n increases with the increase of the frequency of input field. Thus the refractive index $n_{2\omega}$ would not be equal to n_ω.

To solve this problem, the most common procedure is to use the birefringence many materials display. In a birefringent uniaxial crystal, light rays with polarization perpendicular to the optical axis have an ordinary refractive index n_o and light rays with polarization parallel with the optical axis have an extraordinary refractive index, denoted as n_e. Subscript o, e stand for ordinary and extraordinary rays respectively. In Figure 2.5, both n_o and n_e are increasing functions of ω. And in general, when the angle between the optic axis and the direction of propagation θ ranges from 0° to 90°, the value of refractive index varies from n_o to n_e, i.e.,$n_o < n_e(\theta) < n_e$. So by adjusting the incident angle θ of the light beam on the crystal, we may shift the function line of $n_e(\theta)$ (the middle line in the figure) in between n_e and n_o to achieve n_ω (point A) equal to $n_{2\omega}$ (point B), and thus satisfy the phase matching condition.

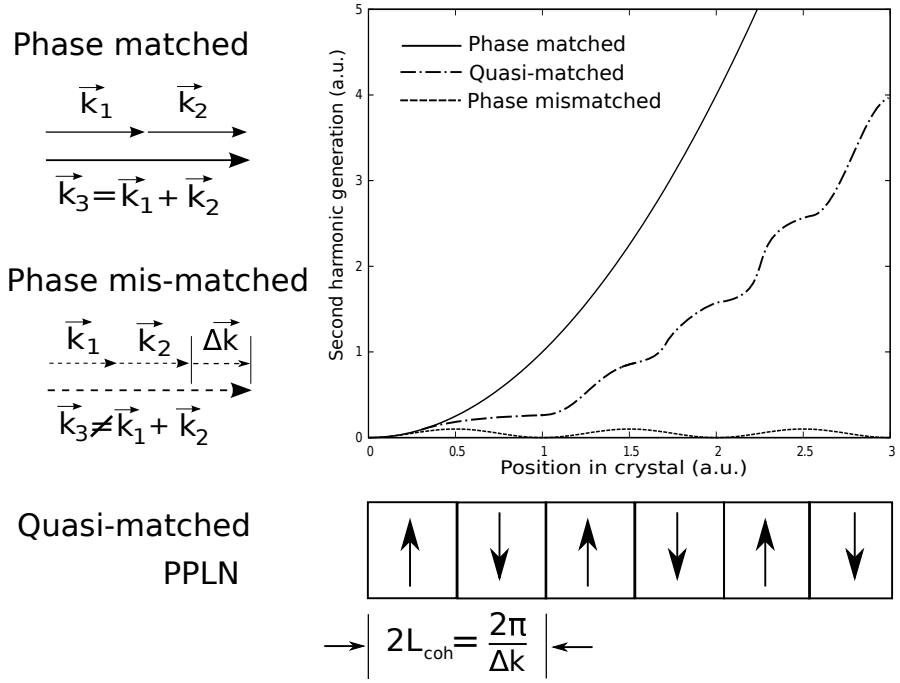

Figure 2.4. Comparision of second harmonic generation when it is phase-matched, quasi-phase-matched and phase mismatched. The amplitude of second harmonic fields accumulates exponentially when the phase matching conditioin is satisfied (the solid line). When the phase is not matched, second harmonic generation oscillates at low amplitude and there is hardly any output field (the dashed line). Quasi-phase matching is a technique that crystal orientation is alternated periodically so that the energy can still positively flow from the fundamental frequency field to the second harmonic frequency field (the dash-dot line). PPLN: Periodically Poled Lithium Niobate.

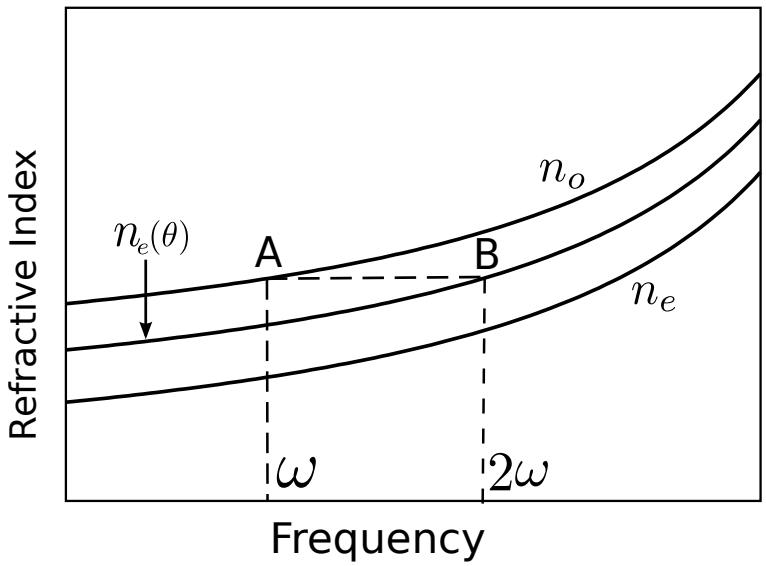

Figure 2.5. Refractive index n as a function of angular frequency for the o-ray and e-ray. Refractive index for the e-ray (n_e) is a function of θ, the angle between the optic axis and the propagation direction of the light. By adjusting the incident angle θ, we can shift the function line $n_e(\theta)$ up and down. Through this method, we may make n_o at 2ω (point A) equal to $n_e(\theta)$ at ω (point B), and satisfy the phase matching condition.

Besides using angle tuning, temperature tuning is a second method to meet the phase matching condition $n_{2\omega}(T) = n_{\omega}(T)$, T being the temperature. There are several pros and cons for using temperature tuning. One advantage of temperature tuning is that it can avoid spatial beam walk-off. i.e., when the light beam propagates with some angle to the optic axis, as is required in angle tuning, the Poynting vector is no longer perpendicular to its wave front, causing the energy of the beam to "drift away" from its wave vector and degrade the beam quality. Some disadvantages of using temperature tuning are that the tuning range may be relatively small compared with angle tuning, and the nonlinear conversion efficiency is sensitive to a small temperature fluctuation. In our experiment, temperature of the nonlinear crystal $KNbO_3$ is controlled using a thermo-electric cooling (TEC) to reach its maximum converting efficiency.

2.1.4 Quasi-Phase Matching

In some circumstances, it may not be suitable to achieve a perfect phase-matching in a birefringent crystal. For example, some crystals display little birefrigence at certain wavelengths, making it impossible to find that n_o at 2ω equals to $n_e(\theta)$ at ω. In such cases, a technique known as quasi-phase matching (QPM) can be applied to achieve sufficient nonlinear conversion.

We already know that when the phase is mis-matched, the energy flows periodically in between the fundamental frequency and the second harmonic. The idea of quasi-phase matching is to periodically flip the orientation of the crystalline axes whenever the energy is about to flow back from the generated harmonic to the fundamental frequency. This technique ensures that there is always positive energy flow from the fundamental frequency to the second harmonic even though they are not phase locked with each other. The length of each period is given $2L_{coh} = \frac{2\pi}{\Delta k}$. Here L_{coh} is the coherence length and Δk is the amount of phase that is not matched $\Delta k = k_3 - k_1 - k_2$.

There are several advantages of using quasi-phase matching. First, there is no spatial walk-off or influence from temperature fluctuation as discussed in angle tuning and temperature tuning. Second, in perfect phase matching, the fundamental frequency and second harmonic have different polarizations. While in quasi-phase matching, both of the frequencies can have the same polarization. This allows us to exploit the largest component of the tensor $\chi^{(2)}_{ijk}$. This may increase the conversion efficiency even higher than perfect phase-matching. Third, it is possible to allow phase matching in non-birefringent materials. A comparison of phase-matched, phase-mismatched and quasi-phase matched conditions is shown in Figure 2.4.

In our lab, the quasi-phase matching technique is applied in periodically poled lithium niobate (PPLN) for efficiently doubling the laser frequency (halving the wavelength) from $1560nm$ to $780nm$.

2.2 Raman Processes

In this section, a general Raman process will be first introduced. Spontaneous Raman Scattering is a very weak process. The conversion efficiency can be increased by stimulated Raman scattering. We further take a close look at the Raman process in our specific cesium atomic system. To fully understand how Raman lasers interact with cesium atoms, we review some basic knowledge of atomic physics including notational conventions of quantum numbers, fine structure, and hyperfine structure of cesium energy levels.

2.2.1 Spontaneous and Stimulated Raman Scatterings

When light propagates in the sky, the most predominant scattering, as we know, is Rayleigh scattering. Rayleigh scattering is elastic scattering. The wavelength of the scattered light is unchanged in Rayleigh scattering. In the process, a small portion of the scattered light could either gain or lose energy from molecules of the medium, causing a shift of the wavelength. This inelastic scattering phenomenon was

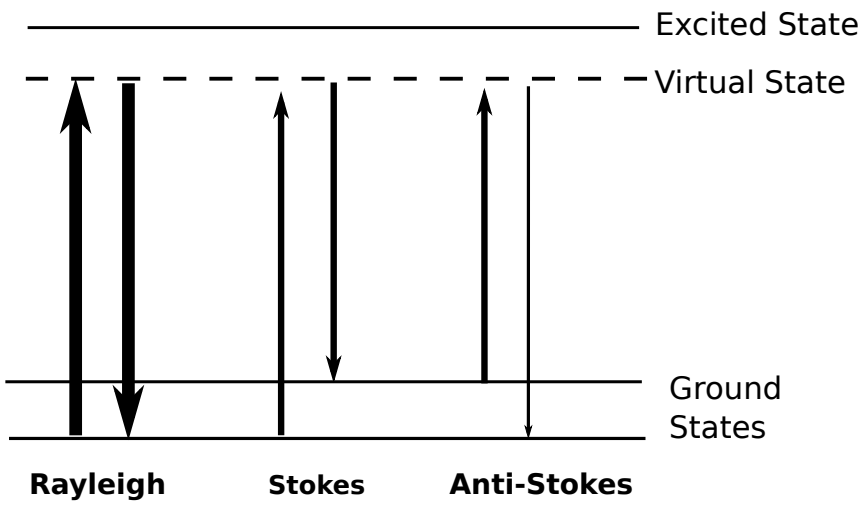

Figure 2.6. An energy level digaram compares Rayleigh scattering with Raman scattering. There is no energy change and the scattering strength is strong in Rayleigh scattering. Stokes Raman scattering occurs when the photons lose energy. Anti-Stokes Raman scattering occurs when the photons gain energy. The strengths of the Stokes and anti-Stokes scatterings are quite low.

first discovered by C.V. Raman in 1928 and named as Raman scattering [17]. In the scattering process, if the incident photons lose energy to molecules, the effect is called Stokes effect. On the other hand, if the incident photons gain energy from molecules, the effect is called anti-Stokes effect. An energy level picture of Rayleigh scattering, Stokes and anti-Stokes Raman scattering is shown in Figure 2.6. In a typical Raman process, the light interacts with vibrational or translational modes of molecules. A virtual state is detuned from the electronic state of molecules. The virtual state can be understood as a short-lived distortion of the electron distribution by the electric field of the incident light.

Spontaneous Raman scattering is typically a very weak process. Approximately one in 10^6 photons is a Stokes photon through every centimeter of solid medium [56]. The rate of anti-Stokes scattering is even weaker by several orders of magnitude.

In contrast, the stimulated Raman process could be much stronger. By deliberately injecting Stokes field together with the Raman pump field, a conversion rate of

10% or more can be reached [18, 19]. Stimulated Raman scattering is a nonlinear-optical effect. The induced Stokes field is nonlinearly dependent on the strength of the Raman pump field. This process can be used in Raman amplifiers and Raman lasers [20]. Raman scattering also offers a simple way of extending the wavelength range of laser systems.

Both spontaneous and stimulated Raman processes are used in our experiments. First, with a strong Raman pump field input, initial Stokes photons are generated by spontaneous Raman scattering. After that, those Stokes photons propagate to induce stimulated Raman scattering in the subsequent part of the medium.

Raman scattering has not only been investigated intensively in theories, but also enjoyed its broad applications in various areas. Because the energy shift of the Raman field is a direct measurement of the translational or vibrational energies of molecules, Raman spectroscopy is widely used as a technique to provides a fingerprint of some chemical and bio-medical materials [21].

2.2.2 Atomic Raman Process

Recently, the Raman process has also be explored in areas of quantum communication and high-precision spectroscopy. For example, in the so-called DLCZ protocol [10], a Raman pulse is used to 'write' quantum information into an atomic ensemble that is later retrieved by a 'read' pulse [10]. An atomic interferometer has also been demonstrated using stimulated Raman transitions [22].

The atomic Raman process is much like the more common molecular Raman process. Except that, in the molecular Raman process, the energy difference is associated with different vibrational modes, while in the atomic Raman process, the energy difference is more commonly associated with two hyperfine levels or Zeeman splittings.

To carry out Raman transition experiments on atomic ensembles and interpret the experimental results we need a thorough understanding of the atomic energy level structure. Cesium-133 (Cs) atoms are used in our efficient Raman conversion

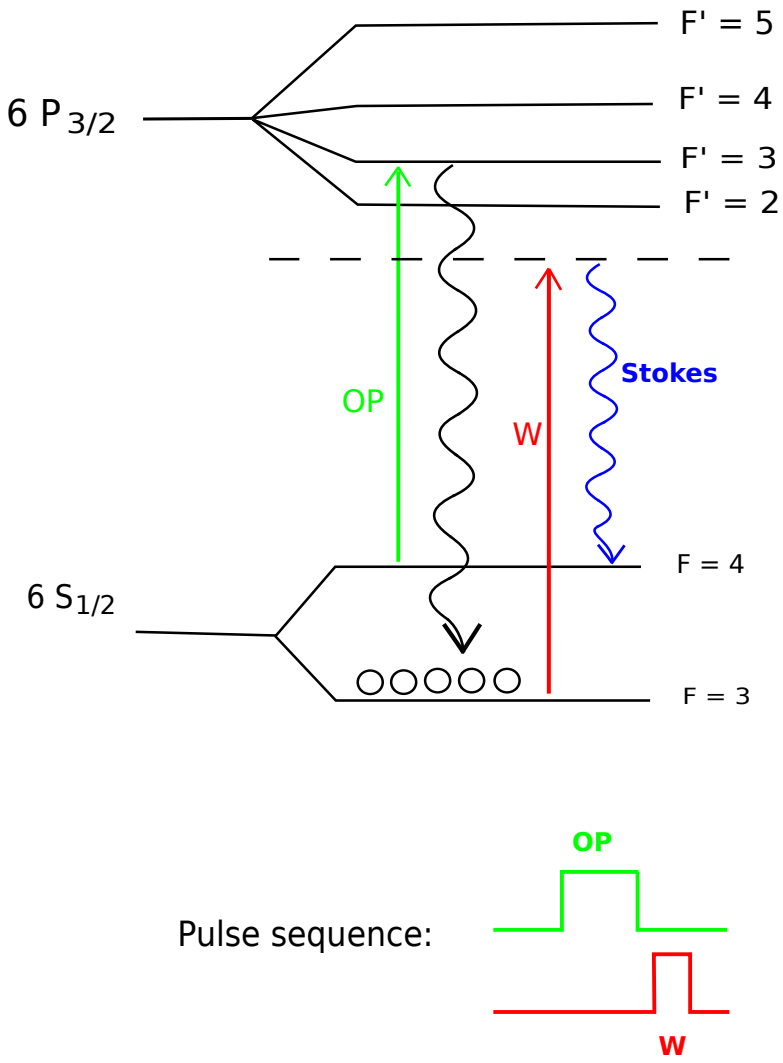

Figure 2.7. Cesium energy levels related to its D2 line. The ground state $6^2S_{1/2}$ has two hyperfine splittings $F = 3, F = 4$. The excited state $6^2P_{1/2}$ has four hyperfine splittings $F' = 2, F' = 3, F' = 4, F' = 5$. The optical pump laser pulse is first applied to pump population from $6^2S_{1/2}, F = 4$ to $6^2S_{1/2}, F = 3$. The W laser pulse is applied shortly after the OP pulse to generate Stokes photons. The W laser is red-detuned to a virtual state close to the excited state.

experiment. Specifically, we use cesium D2 line hyperfine structure as a Λ-level configuration for the Raman process. A brief introduction of cesium atomic energy levels is given.

Cesium is an alkali metal with only one outermost electron located at shell n=6. For its ground state, orbital angular momentum $L = 0$, spin $S = 1/2$, so the total electron angular momentum J can only take the value of 1/2. Its state symbol is given as $6^2S_{1/2}$. Here the spin multiplicity $2S + 1 = 2$ gives S=1/2, and the subscript gives the value of J=1/2. For its first excited state, L = 1 and S = 1/2, so J can take two values, 1/2 or 3/2. The energy line is thus split into two levels, $6^2P_{1/2}$ and $6^2P_{3/2}$. The transition from the ground state $6^2S_{1/2}$ to $6^2P_{1/2}$ is called the D1 line, with its energy difference corresponding to a wavelength of $894nm$. The transition from the ground state $6^2S_{1/2}$ to $6^2P_{3/2}$ is called the D2 line, with its energy difference around $852nm$. Because the D1 and D2 lines have a large separation, generally they are treated separately. We only use D2 lines in our experiment. This doublet (D1 and D2 lines) is called fine structure. Additionally, each of these lines has hyperfine structure, which is a result of the coupling of J with the nuclear spin angular momentum I. For cesium, the quantum number of the nuclear spin angular momentum is I=7/2. For the ground state, J=1/2, the total angular momentum quantum number F can take values of 3 and 4 [16]. For the excited state of the D2 line, F can take values of 2, 3, 4, or 5.

In our efficient Raman experiment, we first use an optical pump (OP) laser to pump all atoms to the ground state $6^2S_{1/2}, F = 3$. After that, a W laser is applied to generate Stokes photons. The optical pump laser is tuned to the resonance frequency of one of the D2 lines. The W laser is either red detuned or blue detuned to off-resonance frequency to generate Raman field, as shown in Figure 2.7.

Considering lots of symbols are used to describe the quantum state of the atoms, a list these symbols are made for a quick reference:

- n, the electron principal quantum number. It can take positive integer values $1, 2, 3 \ldots$
- l, the electron orbital angular momentum quantum number. It can take integer values ranging from 0 to $n - 1$.

- m, the electron magnetic quantum number. It can take integer values ranging from $-l$ to l.

- S, the electron spin quantum number. For cesium, $S = 1/2$. The projection of spin on specified axis can take two values, either spin up $m_s = +1/2$, or spin down $m_s = -1/2$.

- J, total electron angular momentum. The interaction between orbital angular momentum l and spin S result in the $l - S$ coupling. J can take integer values in the range $|l - S| \leq J \leq |l + S|$.

- I, the nuclear spin angular momentum.

- F, the total atomic angular momentum. It is the result of coupling of the total electron angular momentum J and nuclear angular momentum I. It can take integer values $|J - I| \leq F \leq J + I$.

- $^{2S+1}L_J$, atomic term symbol. It is used to describe the state of atom. $2S + 1$ is its spin multiplicity. The nomenclature $S, P, D, F \ldots$ are used respectively to represent $L = 1, 2, 3, 4 \ldots$

Not all transitions are allowed between any two quantum states. Selection rules apply for certain transitions. In general, the interaction strength between atoms and photons is characterized by the electric dipole matrix elements [16]. It determines if the transitions from one state to another are allowed or restricted. Selection rules vary for different types of interactions. In our system, the transition from the hyperfine ground states $6^2S_{1/2}$ to the $D2$ excited hyperfine state $6^2P_{3/2}$ has to follow $\Delta F = 0, \pm 1$. This is simply because the angular momentum of photon can only change the angular momentum quantum number by 0 or ± 1. For example, the atom can not make the transition from $6^2S_{1/2}, F = 3$ to $6^2P_{3/2}, F' = 5$, because $\Delta F = 2$. For the same reason, it cannot go from $6^2S_{1/2}, F = 4$ to $6^2P_{3/2}, F' = 2$ either.

2.3 Quantum Mechanical Description of Three Wave Mixing Process

In quantum mechanics, the three-wave mixing process can be described by the interaction Hamiltonian [57, 58, 60].

$$\hat{H} = i\hbar\eta\hat{a}_p\hat{a}_s^\dagger\hat{a}_i^\dagger - i\hbar\eta^*\hat{a}_s\hat{a}_i\hat{a}_p^\dagger, \tag{2.27}$$

where $\hat{a}$ is the annihilation operator and $\hat{a}^\dagger$ is the creation operator. The operators $\hat{H}$, $\hat{a}$ and $\hat{a}^\dagger$ are in the Heisenberg picture. The subscripts p,s,i stand for pump, signal and idler respectively. η is the coupling coefficient that contains $\chi^{(2)}$. From the equation, we see that for every pump photon created, one signal photon and one idler photon are destroyed and vice versa.

When the signal field is much stronger than the pump and idler field, the field operator $\hat{a}$ can be replaced by its classical amplitude A, and the three-wave mixing process becomes a frequency converter [5]. Its Hamiltonian is given as

$$\hat{H}_{FC} = i\hbar\eta A_s^*\hat{a}_p\hat{a}_i^\dagger - i\hbar\eta^* A_s\hat{a}_i\hat{a}_p^\dagger. \tag{2.28}$$

It converts an idler photon ($\hat{a}_i$) to a pump photon ($\hat{a}_p$) or vise versa. By plugging the Hamiltonian into Heisenberg's equation of motion for both the pump field mode and the idler field mode

$$\begin{aligned} \frac{d}{dt}\hat{a}_p(t) &= \frac{i}{\hbar}[\hat{H}, \hat{a}_p(t)], \\ \frac{d}{dt}\hat{a}_i(t) &= \frac{i}{\hbar}[\hat{H}, \hat{a}_i(t)], \end{aligned} \tag{2.29}$$

and using the commutation relations

$$\begin{aligned} \left[a_i(t), a_j^\dagger(t)\right] &= \delta_{ij}, \\ [a_i(t), a_j(t)] = \left[a_i^\dagger(t), a_j^\dagger(t)\right] &= 0, \end{aligned} \tag{2.30}$$

we can solve the equations and find out the evolution of the operators [58]

$$\hat{a}_p(t) = \cos(|\eta A_s|t)\hat{a}_p + e^{i\varphi_s}\sin(|\eta A_s|t)\hat{a}_i,$$
$$\hat{a}_i(t) = \cos(|\eta A_s|t)\hat{a}_i - e^{-i\varphi_s}\sin(|\eta A_s|t)\hat{a}_p. \tag{2.31}$$

Here $e^{i\varphi_s} \equiv \eta^* A_s/|\eta A_s|$. When $|\eta A_s|t = \pi/2$, we have $\hat{a}_p(t) = e^{i\varphi_s}\hat{a}_i$ and $\hat{a}_i(t) = -e^{-i\varphi_s}\hat{a}_p$. The interaction time t can be controlled by the length of the crystal. So we may achieve a unit conversion between pump field $\hat{a}_p$ and idler field $\hat{a}_i$. Whether the conversion is from pump to idler ($\hat{a}_p \rightarrow \hat{a}_i$) or from idler to pump ($\hat{a}_i \rightarrow \hat{a}_p$) will depend on the input field. With single photon input at the pump field $|1\rangle_p$ and vacuum state at the idler field $|0\rangle_i$, we may convert the pump photon to idler photon at output with unit conversion efficiency and vice versa.

On the other hand, the Raman process can also be treated as a three-wave mixing process. Correspondingly, these three waves are the write field $\hat{a}_w$, the Stokes field $\hat{a}_s$ and the atomic spin wave $\hat{a}_{asw} \equiv (1/\sqrt{N})\sum_i |g\rangle\langle m_i|$. Here N is the total number of atoms in the atomic ensemble. $|g\rangle$ represents all atoms being in the ground state, i.e $|g\rangle \equiv |g...g\rangle$. And $|m_i\rangle$ represents all atoms in the ground g-state except for the ith atom which is in the m-state, i.e. $|m_i\rangle \equiv |g...m(i\text{th})...g\rangle$. In the cesium system, the g-state is $6^2S_{1/2}, F = 3$, and the m-state is $6^2S_{1/2}, F = 4$. In Raman scattering, the input write field is strong and thus can be treated as a classical field with amplitude A_w. The interaction Hamiltonian is then given as

$$\hat{H}_R = i\hbar\eta A_w \hat{a}_s^\dagger \hat{a}_{asw}^\dagger - i\hbar\eta^* A_w^* \hat{a}_s \hat{a}_{asw}. \tag{2.32}$$

Here $\eta = g_{eg}g_{em}^*\sqrt{N}/\Delta$. g_{eg},g_{em} are the coupling coefficients between light fields and atom states and Δ is the detuning of the light field from the excited state. By plugging the Hamiltonian into Heisenberg's equations of motion Equation 2.29 and using the commutation relations Equation 2.30, we can solve the equations and determine the evolution of the operators.

$$\hat{a}_s(t) = \cosh(|\eta A_w|t)\hat{a}_s - e^{i\varphi}\sinh(|\eta A_w|t)\hat{a}_{asw}^\dagger$$
$$\hat{a}_{asw}(t) = \cosh(|\eta A_w|t)\hat{a}_{asw} - e^{i\varphi}\sinh(|\eta A_w|t)\hat{a}_s^\dagger. \tag{2.33}$$

3. FREQUENCY DOWN-CONVERSION FOR A QUANTUM NETWORK

3.1 Research Background

The realization of many basic concepts in quantum information science requires the use of photons as quantum information carriers and atoms as quantum memory elements. Photons are naturally good quantum information carriers, as they are fast and reliable over long distance transmission, and are thus dubbed the "flying qubits." On the other hand, atoms, serving as "stationary qubits," are best for both storing quantum information in their internal states for a long coherence time and processing locally. Therefore, a quantum network usually consists of nodes made of atoms and connected by photons [51]. In the network, quantum information is constantly transferred between photons and atoms, and transmitted between atoms via photons. Because quantum information is sensitive to losses, minimizing losses is critical to achieve the network. However, in current technology, atoms interact best with photons of wavelength around 0.8 μm [51, 52], whereas optical communication systems have low losses at 1.6 μm [53]. So there is a mismatch between the atomic transition wavelength and the optical transmission wavelength. Thus it is necessary to convert photons from one wavelength to another in order to set up the quantum network.

Quantum information transfer between photons and atoms was realized in frequency up-conversion many years ago [69,71,72]. However, frequency down-conversion that is free of quantum noise has not been reported. The current research in this field focuses on up-converting photons from the telecommunication wavelength 1.6 μm to its half wavelength 0.8 μm. This is because, for photon counting in quantum cryptography, detectors at 1.6 μm are far more noisy than those at 0.8 μm [72]. Moreover,

the quantum noise caused by spontaneous emission in the parametric down-conversion process leads to the belief that it is impossible to have high-fidelity quantum state transfer in a frequency down-conversion process [6]. Therefore, frequency down-conversion seems to be the missing link in this quantum network. Contrary to this common misunderstanding, we demonstrate that a noise-free photon frequency down-conversion is achievable, and a proof-of-principle experiment is implemented [68].

From the chapter "Nonlinear Optics," we derived three coupled equations for a general three-wave propagation process, i.e., Equations 2.20, 2.21 and 2.22. In the specific case of parametric down-conversion process, ω_1, ω_2 and ω_3 are signal, idler and pump fields respectively. Under the condition of a strong and undepleted signal field input, we can treat A_1 as a constant and the set of three equations becomes a set of two equations

$$\frac{dA_3}{dx} = \frac{i\chi^{(2)}_{xxx}\omega_3^2}{k_3c^2}A_1A_2e^{i\Delta kx} \tag{3.1}$$

$$\frac{dA_2}{dx} = \frac{i\chi^{(2)}_{xxx}\omega_2^2}{k_2c^2}A_3A_1^*e^{-i\Delta kx} \tag{3.2}$$

When the phase matching condition is satisfied, i.e., $\Delta k = 0$, we can solve these two equations. By solving for A_3 in Equation 3.2 and substituting A_3 into Equation 3.1, we obtain a second order differential equation

$$\frac{d^2A_2}{dx^2} = \frac{-(\chi^{(2)}_{xxx})^2\omega_2^2\omega_3^2}{k_2k_3c^4}|A_1|^2A_2 \tag{3.3}$$

By setting the coefficient

$$\frac{(\chi^{(2)}_{xxx})^2\omega_2^2\omega_3^2}{k_2k_3c^4}|A_1|^2 = \kappa^2, \tag{3.4}$$

the equation simply becomes

$$\frac{d^2A_2}{dx^2} = -\kappa^2A_2. \tag{3.5}$$

The general solution is

$$A_2(x) = C \sin \kappa x + D \cos \kappa x \tag{3.6}$$

C and D are constants that are determined by the initial conditions. By setting the initial condition of the idler field

$$A_2(0) = 0, \tag{3.7}$$

we can get $D = 0$. The coefficient C is determined by the initial condition of the pump field, i.e., $A_3(0)$. Finally we obtain the solution of the generated idler field amplitude as a function of the distance in the nonlinear crystal.

$$A_2(x) = i(\frac{\omega_2 n_3}{\omega_3 n_2})^{1/2} \frac{A_1^*}{|A_1|} A_3(0) \sin \kappa x \tag{3.8}$$

Here n_2 and n_3 are the refractive indices. From the solution, we see that there is a linear relation between the amplitude of the generated idler field and that of the input pump field.

$$A_2(L) \propto A_3(0) \tag{3.9}$$

Here L is the length of the nonlinear crystal. In the following section we will experimentally confirm this linear dependence.

3.2 Experimental Implementation

The experimental setup mainly comprises three stages. First of all, noncollinear parametric up-conversion is realized with angle tuning phase matching. Secondly, based on the result of up-conversion, the up-converted beam is reflected back through the same path so that the incident angle of the pump field can be determined and noncollinear parametric down-conversion is realized. Thirdly, the pump field is attenuated to examine the linear dependence of the signal field on the pump field when the latter is weak. An interference fringe shown between the signal field and original laser light is a direct proof of coherence preservation.

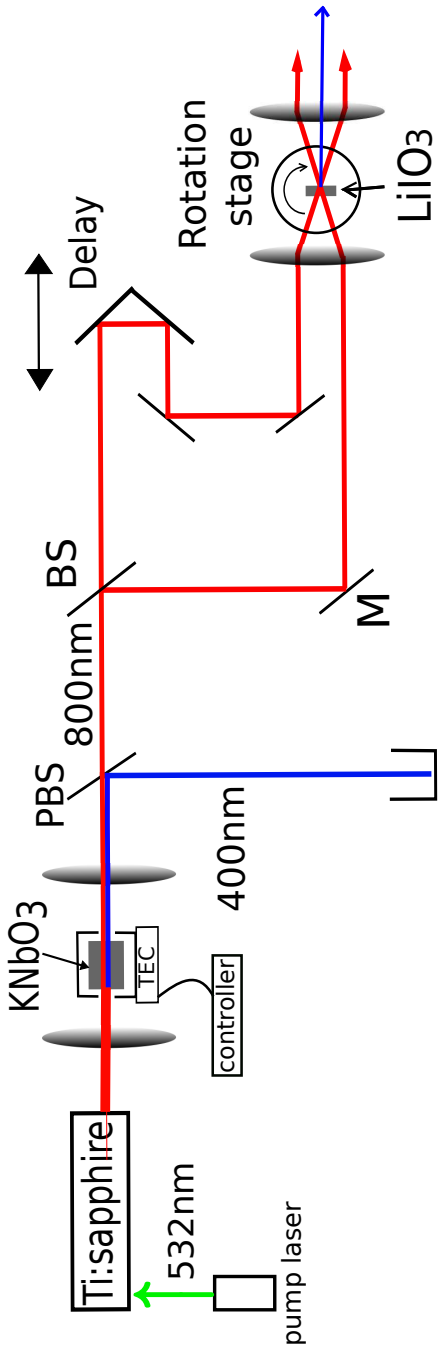

Figure 3.1. A schematic diagram for the first stage of the experiment. TEC: thermo-electric cooler. PBS: polarized beam splitter. BS: beam splitter. M: coated mirror.

In the first stage, the experiment is set up as shown in Figure 3.1. Our Pump laser is a Millennia Pro laser at the wavelength of 532 nm. Our main laser is a tunable femtosecond Ti:Sapphire laser with an output power at around 300 mW and pulse repetition rate of 80 MHz. The pulse duration is 100 fs. The wavelength of the laser source is tuned to 800 nm, as marked in red color in the schematic Figures 3.1,3.3 and 3.4. The laser beam first passed through a nonlinear crystal $KNbO_3$ with temperature controlling for meeting the phase matching condition. In order to adjust the temperature of the crystal and avoid unstable temperature fluctuations caused by air flow, the crystal is placed in a metal housing with two holes cut open just for the laser beam passing through. The housing is stuck on top of a Thermo-Electric Cooler (TEC) by thermal adhesive mixed from two-part epoxy resin. Some thermal paste is also applied between the crystal and the house to increase the heat conduction efficiency. Finally, a TEC controller is used to adjust the electric current applied to the TEC to adjust and stabilize the temperature of the crystal. A pair of lenses is placed on both sides of the crystal to achieve a higher conversion rate while maintaining the profile of the laser beam. When the phase matching condition is satisfied by temperature tuning, the second harmonic field is generated all the way through the crystal. As a result, the IR and the blue beams propagate collimated. A Polarized Beam Splitter (PBS) is used to separate the IR and blue beams since they are in orthogonal polarization. A dichroic mirror is an alternative choice here. The blue beam is kept for future use in the second stage of our experiment. The IR beam is then separated by a Beam Splitter (BS). One of the beams goes to the delay, which is made out of two coated mirrors that are attached to a computer controlled motor stage. The motor stage is scanned back and forth to locate a spot where the two arms of the beams are of equal length so that the two pulses can arrive in the second crystal ($LiIO_3$) overlapped not only in space but also in time. The full width at half maximum (FWHM) of the pulse $\times$ the speed of light shows how precisely we need to control the delay, i.e., $100fs \times 3 \times 10^8 m/s = 30\mu m$.

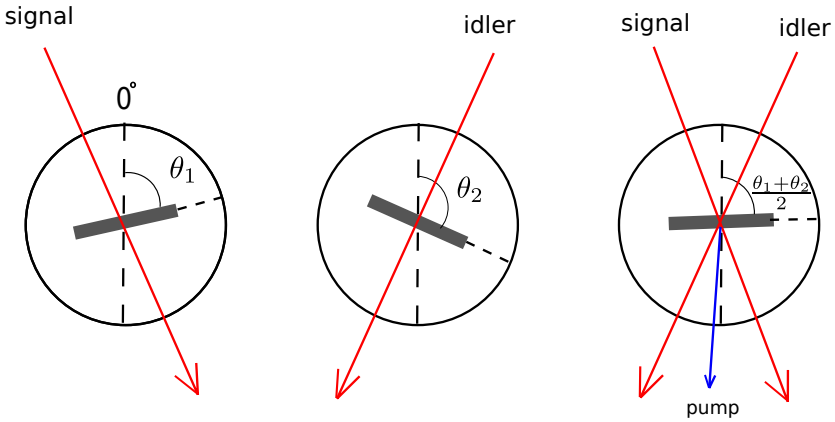

Figure 3.2. A method to find the phase matching angle for non-collinear parametric up-conversion. First, θ_1 is found to be the phase matching angle for the signal field. Second, θ_2 is found to be the phase matching angle for the idler field. Last, the crystal is rotated in such an angle $(\theta_1+\theta_2)/2$ to satisfy phase matching for noncollinear parametric up-conversion.

The phase matching condition is achieved by angle tuning for the second nonlinear crystal $LiIO_3$. The procedure to achieve noncollinear up-conversion is shown in Figure 3.2. The crystal is first placed on a rotational stage with an angle scale. Step one, the crystal is rotated to obtain the phase matching angle for the signal beam and the angle is recorded as θ_1. Step two, the crystal is again rotated to obtain the phase matching angle for the idler beam and the angle is recorded as θ_2. Step three, the crystal is rotated to an angle of $(\theta_1 + \theta_2)/2$. The delay and the lens in front of the crystal are further adjusted to ensure the two focused pulses overlap both in time and space inside the crystal. The sum frequency is then generated at wavelength 400 nm as shown in blue color in the schematic figures.

In the second stage of the experiment, the up-converted blue is reflected back through the same path in order to find the incident angle of the pump. The reason that these steps are necessary is because directly setting up the phase matching angle for down-conversion is much more difficult. Two pinholes are added along the path of the blue beam generated from the $LiIO_3$ crystal as shown in Figure 3.3. By

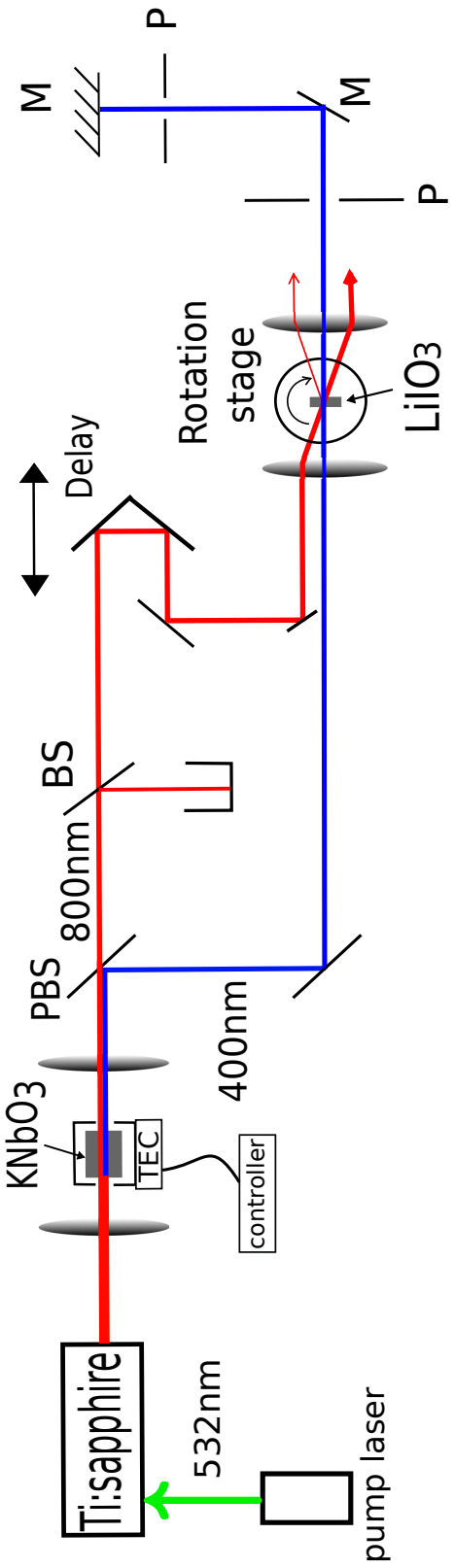

Figure 3.3. A schematic diagram for the second stage of the experiment. TEC: thermo-electric cooler. PBS: polarized beam splitter. BS: beam splitter. M: coated mirror. P: pinhole.

adjusting the mirror at the end, we can reflect the blue beam back through those two pinholes to the mirror below the polarized beam splitter (PBS) as presented in the figure. By further adjustment of the mirror and the PBS, we can make the blue beam separate from the PBS and the blue beam generated from $LiIO_3$ overlap in space when they are outside the crystal. The down-conversion shall be seen at the spot where the original idler light appears when we block one of the IR beams and adjust the delay again in order for the new blue pulse overlapping with the other IR beam in time inside the crystal. As a matter of fact, they can not overlap all the way through the crystal like the two IR beams because their group velocities in the crystal are different. This causes the interaction time of the beams inside the crystal to be shorter thus the conversation rate is lower. We can find the parametric down-conversion by this method because when the phase matching condition is satisfied, the three-wave mixing Hamiltonian tells us that the conversion is processing in both directions. i.e. from one pump photon to a signal photon and idler photon, or from a signal photon and idler photon to pump photon. Which way the conversion happens depends on the initial conditions. In stage one, the pump field is in the vacuum state, so the conversion is from (signal+idler) to pump. In the second stage, the idler field is set at vacuum state, so the conversion is stimulated by signal and energy flow from pump to (signal+idler).

In the third stage of the experiment, we first check the linearity of the detected idler field as a function of the attenuation factor on the incoming pump field, as predicted from Equation 2.31. A photograph of the experimental setup is shown in Figure 3.5.

A step variable neutral density filter is placed in the blue beam to attenuate the intensity of the pump field as shown in Figure 3.4. The down-converted idler light is reflected to an interference filter (IF) and a photo-detector (D). The result is finally shown on an oscilloscope. The data are recorded at the oscilloscope each time after the attenuation is adjusted from 0 dB to 30 dB. The result is shown in Figure 3.6 on a logarithmic scale. The x axis is the transmission factor, which is the reciprocal of

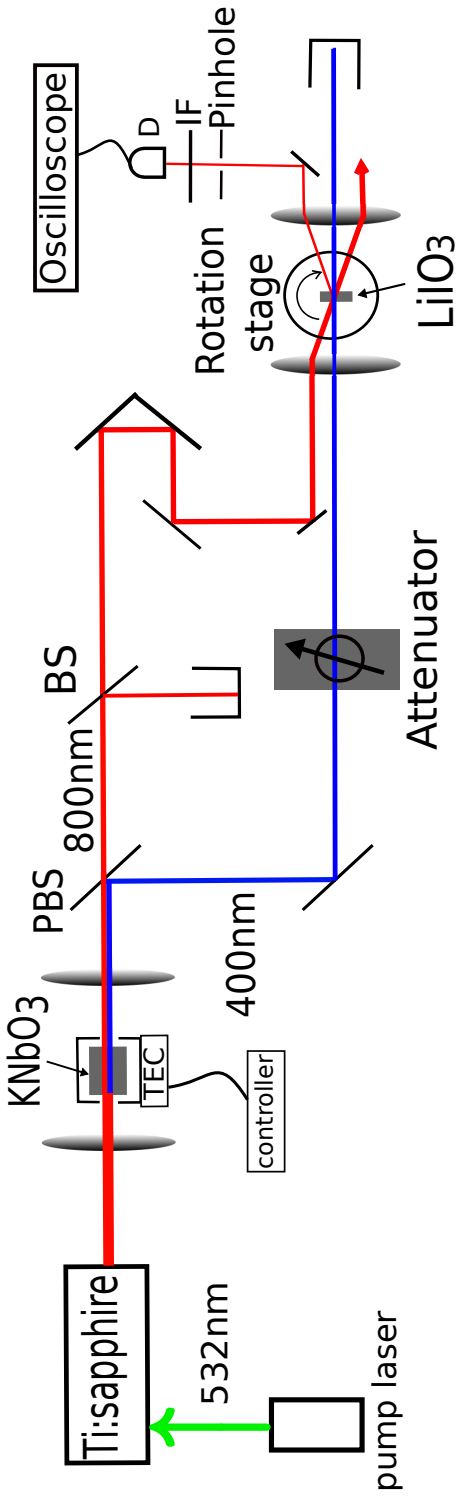

Figure 3.4. A schematic diagram for the third stage of the experiment. TEC: Thermo-Electric Cooler. PBS: Polarized Beam Splitter. BS: Beam Splitter. M: Coated Mirror. P: Pinhole. IF: Interference Filter. D: Detector.

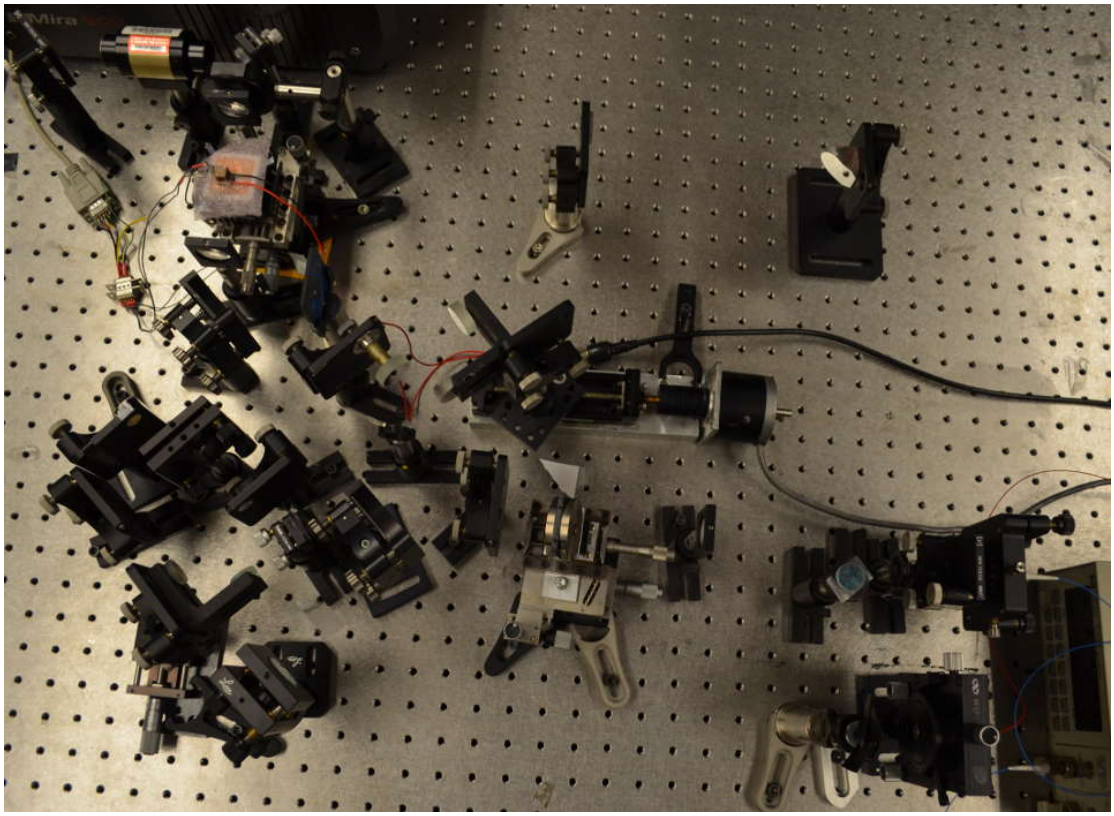

Figure 3.5. A photograph of the experimental setup taken from above the optical table.

the attenuation factor. The y axis is the relative intensity of the idler field recorded from the oscilloscope. The best fit line is given with its slope equal to 1.0. It can be seen that in a range of three orders of magnitude, the detected idler field follows well the linear dependence on the pump field.

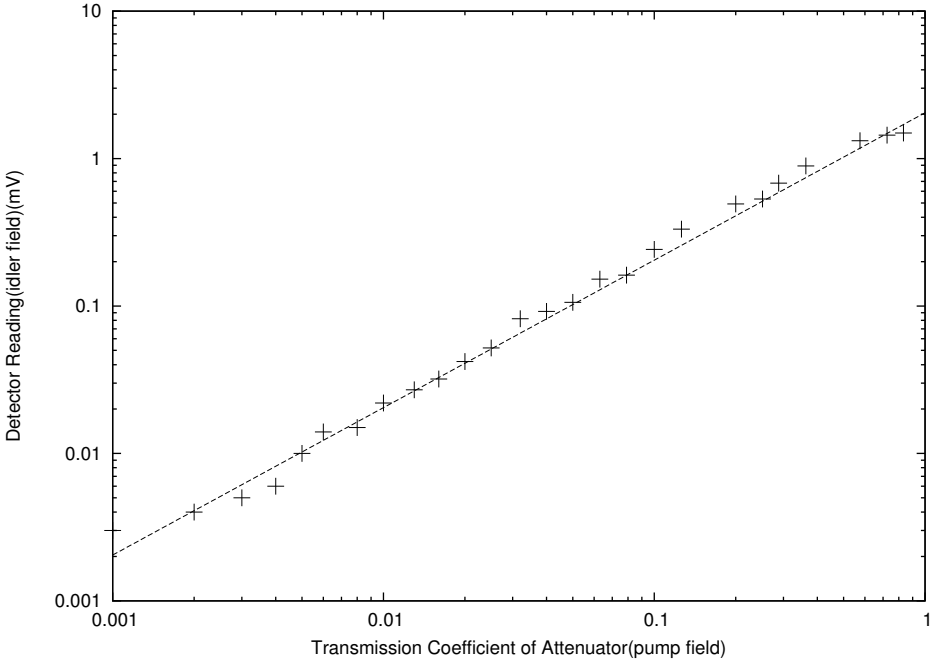

Figure 3.6. The detected idler field power as a function of the transmission coefficient of the attenuator. The slope of the best fit line is equal to 1.0 on the logarithmic scale.

We further investigate Equation 2.31 by rewriting the transformation in a matrix as seen in Equation 3.10. The evolution from input $\begin{pmatrix} \hat{a}_p \\ \hat{a}_i \end{pmatrix}$ to the output $\begin{pmatrix} \hat{a}_p(t) \\ \hat{a}_i(t) \end{pmatrix}$ is an SU(2) transformation.

$$\begin{pmatrix} \hat{a}_p(t) \\ \hat{a}_i(t) \end{pmatrix} = \begin{pmatrix} \cos(|\eta A_s|t) & e^{i\varphi_s}\sin(|\eta A_s|t) \\ -e^{-i\varphi_s}\sin(|\eta A_s|t) & \cos(|\eta A_s|t) \end{pmatrix} \begin{pmatrix} \hat{a}_p \\ \hat{a}_i \end{pmatrix} \tag{3.10}$$

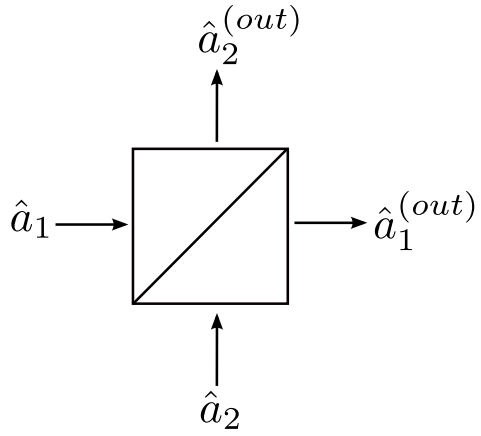

Figure 3.7. A schematic diagram of a beam splitter. $\hat{a}_1$ and $\hat{a}_2$ are the input modes and $\hat{a}_1^{(out)}$ and $\hat{a}_2^{(out)}$ are the output modes.

$$\begin{pmatrix} \hat{a}_p(t) \\ \hat{a}_i(t) \end{pmatrix} = \begin{pmatrix} e^{i(\varphi_s/2)} & 0 \\ 0 & e^{-i(\varphi_s/2)} \end{pmatrix} \begin{pmatrix} \cos(|\eta A_s|t) & \sin(|\eta A_s|t) \\ -\sin(|\eta A_s|t) & \cos(|\eta A_s|t) \end{pmatrix} \begin{pmatrix} e^{i(\varphi_s/2)} & 0 \\ 0 & e^{-i(\varphi_s/2)} \end{pmatrix} \begin{pmatrix} \hat{a}_p \\ \hat{a}_i \end{pmatrix} \tag{3.11}$$

The transformation matrix can be further expressed in terms of three matrices as shown in Equation 3.11. It turns out that the input-output relation of such a system is the same as that of a lossless beam splitter [70]. For a beam splitter as shown in Figure 3.7, the transformation from input modes $\hat{a}_1$ and $\hat{a}_2$ to output modes $\hat{a}_1^{(out)}$ and $\hat{a}_2^{(out)}$ is given in Equation 3.12. The transformation composes three steps. It first shifts the phases by φ between $\hat{a}_1$ and $\hat{a}_2$, then mixes two modes via a rotation, and finally shifts the phases again by φ. The transmittance of the beam splitter is given by $T = cos^2(\alpha)$ and the reflectance is given by $R = sin^2(\alpha)$. $T + R = cos^2(\alpha) + sin^2(\alpha) = 1$.

$$\begin{pmatrix} \hat{a}_1^{(out)} \\ \hat{a}_2^{(out)} \end{pmatrix} = \begin{pmatrix} e^{i(\varphi/2)} & 0 \\ 0 & e^{-i(\varphi/2)} \end{pmatrix} \begin{pmatrix} \cos(\alpha) & \sin(\alpha) \\ -\sin(\alpha) & \cos(\alpha) \end{pmatrix} \begin{pmatrix} e^{i(\varphi/2)} & 0 \\ 0 & e^{-i(\varphi/2)} \end{pmatrix} \begin{pmatrix} \hat{a}_1 \\ \hat{a}_2 \end{pmatrix} \tag{3.12}$$

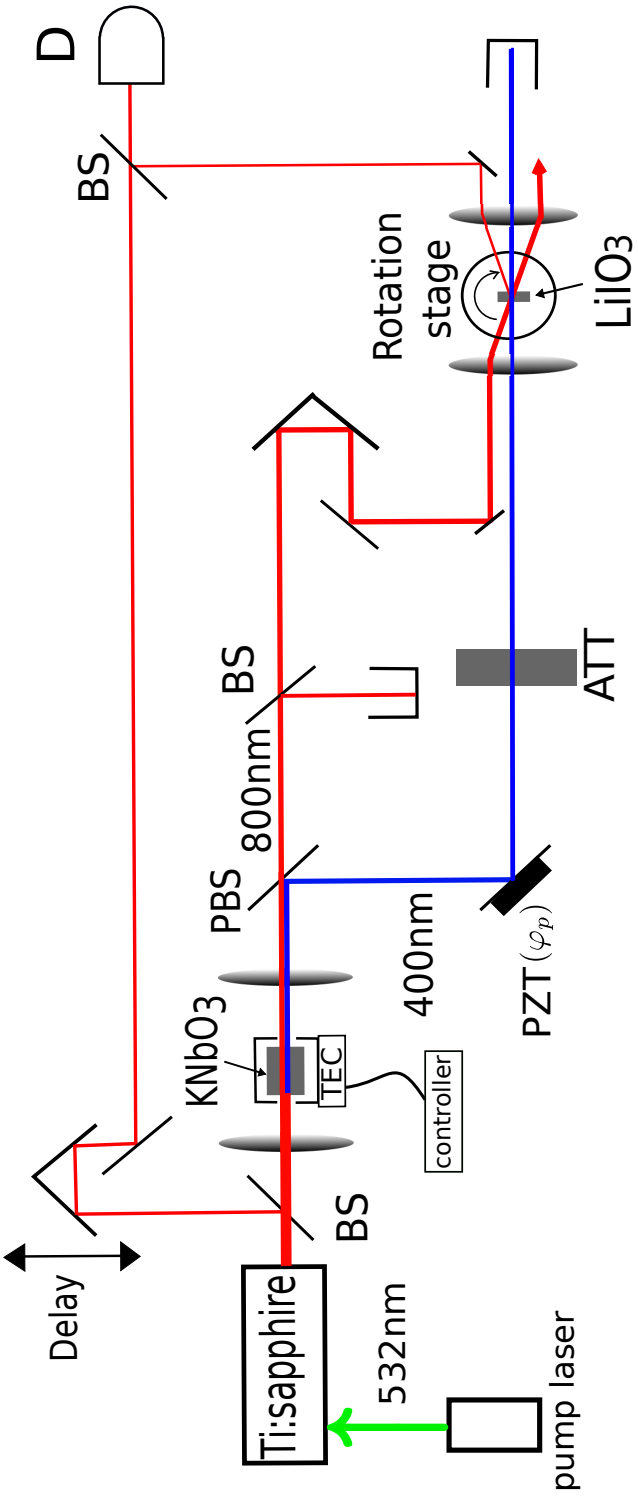

Figure 3.8. A schematic diagram for the demonstration of frequency down-conversion. TEC: Thermo-Electric Cooler. PBS: Polarized Beam Splitter. BS: Beam Splitter. M: Coated Mirror. ATT: Attenuator. IF: Interference Filter. D: Photo-detector. PZT: Piezoelectric Transducer.

Since the relation between the input modes and output modes for the down-conversion system is essentially the same as a beam splitter, coherence should be preserved for our system just like it is when photons pass through a beam splitter.

Following is the experiment to show that coherence is preserved in the conversion from the pump field to the idler field. In Figure 3.8, a small portion of the beam is split from the original laser and combined with the idler field by a beam splitter and then measured by a detector. A delay system is used to make sure pulses from each beam arrive at the detector at the same time. Since the down-conversion process that we are using is a degenerate one with $\omega_s = \omega_i = \omega_p/2$, the generated idler field has the same frequency as that of the laser. Therefore we will be able to see an interference fringe if the idler field has a phase relation with the pump. The phase scan is on the pump field and is achieved by applying a ramp voltage on a piezoelectric transducer (PZT in Figure 3.8). The result of the experiment is shown in Figure 3.9. The sinusoidal change in the detected signal shows interference between the generated idler field and the laser field but with a phase dependence on the pump field. This clearly demonstrates the coherent photon conversion from the pump field to the idler field.

3.3 Type II Phase Matching

The next step of the experiment was planned to reduce the intensity of the pump field to single-photon level and to do photon counting on idler field with an Avalanche Photon Detector (APD). However, when the detector is sensitive at the single-photon level, the scattering of the strong signal beam at the crystal becomes an unavoidable factor. The power of the signal field is at the level of milliwatts. On average, approximately 1 out of 10^8 photons from the signal field is measured by the detector about 0.5 meter away from the crystal, regardless of direction. By considering the frequency of the pulse and the energy of one photon, we can calculate that the detector receives about 100 photons, on average, per pulse from the scattering.

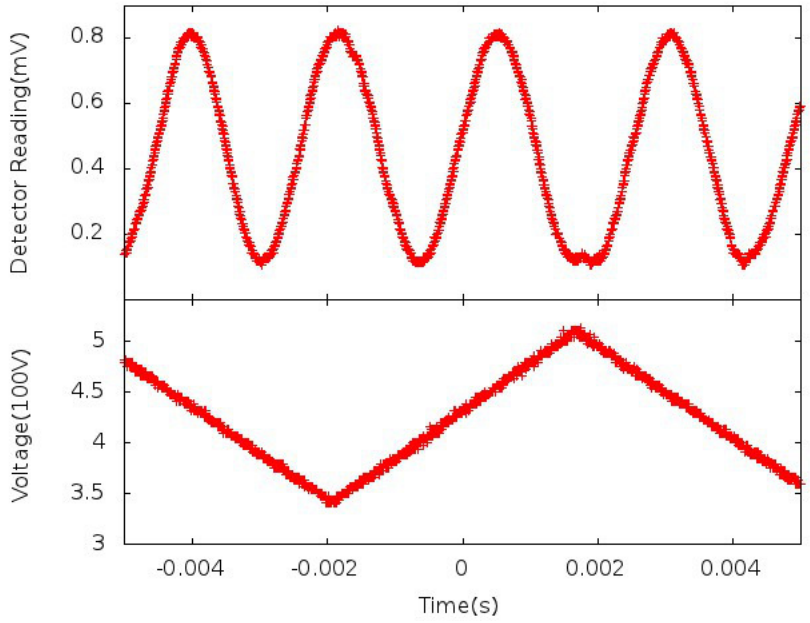

Figure 3.9. The upper trace is the interference fringe between the generated idler field and the original laser field. The lower trace is the ramp signal from the high voltage applied to the PZT for scanning the phase of the pump field.

To reduce the effect of scattering, a second experiment is set up in such a way that polarization of the idler and signal fields are perpendicular. The $LiIO_3$ is replaced by a Type II phase matched Lithium Triborate LiB_3O_5 (LBO) crystal. A Polarized Beam splitter (PBS) is placed in front of the detector to further reduce the scattering to a level about 1000 times smaller than that in the type I configuration. The extinction ratio of the PBS is about 1000:1. The scattering noise is reduced to about one photon per 10 pulses on average. Because the laser emits 80 million pulses per second, there are still millions of photons per second from scattering at the avalanche single-photon detector.

We propose that non-degenerate down-conversion can be performed to further reduce the scattering intensity, i.e., when the frequencies of the signal ω_s and the idler ω_i are not the same, an interference filter in front of the detector can more effectively eliminate the scattered photons.

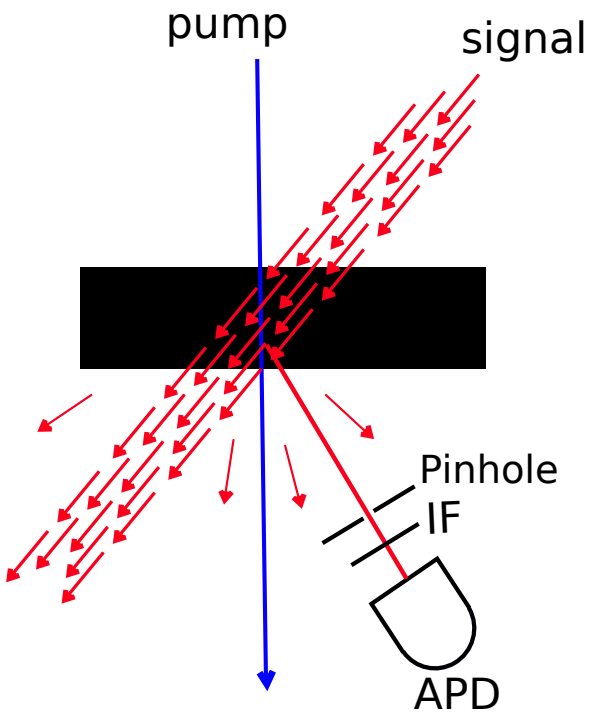

Figure 3.10. The strong signal field scatters when it passes through the crystal. A small portion of the signal photons enters the photo-detector. When the pump is reduced to the single-photon level, the amount of scattered photons is comparable with that of the down-converted photons. IF: Interference Filter. APD: Avalanche Photo-Detector.

In summary, we demonstrated that the frequency down-conversion from a pump photon to an idler photon can be coherent. With a strong signal field input, we showed that the parametric down-conversion is free of quantum noise. An interference experiment was set up to demonstrate the coherence of the frequency conversion process. This could pave the way for quantum state transfer with high fidelity from a high-frequency photon to a low-frequency photon and contribute to the building of a quantum network. Three stages of experimental implementation are described in detail. Both Type I and Type II phase matching crystals are tested for trying to improve the signal-to-noise ratio.

One application of such a system is to generate a superposition state of photons with multiple frequencies from a single pump photon, $|1\rangle_p \rightarrow \sum_k c_k |1_{w_k}\rangle$. This technique is an analogy to the Wavelength-Division Multiplexing (WDM) technique widely used in classical optical fiber communication. Moreover, a single photon is the preferred source to defeat the photon splitting attack in Quantum Key Distribution (QKD) [27]. Thus, in such WDM-QKD system, we can use a single pump photon to generate multiple single-photon sources with different frequencies, just like in classical optical communication. A more detailed description of such application can be found on a paper we published at Reference [68]

4. EFFICIENT RAMAN CONVERSION VIA ATOMIC COHERENCE

4.1 Research Background

In the realization of quantum communication and construction of a quantum networks, information is stored and processed locally in the nodes and transmitted through quantum channels. In order to connect the links between nodes and channels, quantum information is constantly transferred from nodes to channels and retrieved from channels to nodes. A physical implementation of such a quantum network could consist of atomic ensembles representing the nodes and optical fibers providing the photonic channels [28]. Practically, a reliable quantum network may require many quantum repeaters to compensate for losses and correct errors over a long distance. Each repeater requires a further exchange of quantum information between atoms and photons. It is thus critical that the quantum information exchange between atoms and photons is coherent and efficient.

In recent studies, The Raman process has been explored actively for the use of creating entanglement and exchanging information between atomic systems and photons [29,30]. For example, in the so-called DLCZ protocol [10], measurement-induced entanglement between two atomic ensembles is generated through spontaneous Raman scattering. The quantum memory is stored in the atomic ensembles and subsequently retrieved by a light pulse at near-resonance frequency with the atoms.

On the other hand, the nonlinear interaction between photons and atoms typically has a low coupling coefficient. In Raman scattering, in particular, the efficiency of conversion from the Raman pump field to the Stokes field is extremely low. A typical ratio of the conversion is approximately one Stokes photon per tens of millions of pump photons. It is even lower for conversion to the anti-Stokes photons. To increase

the conversion efficiency, people traditionally place the Raman medium into a high-finesse optical resonator so that the photons can pass through the medium multiple times and have a higher conversion efficiency. This method was recently developed to achieve strong couplings between single photons and single atoms in the setting of cavity quantum electrodynamics (CQED) [9, 35, 36]. This technique now serves as a tool for other atomic experiments, such as atom trapping and quantum computation.

The efficiency of conversion can also be increased by a stimulated Raman process. Stimulated Raman was achieved by deliberately injecting some initial Stokes or anti-Stokes photons in the medium to induce Raman conversion. The initial Stokes or anti-Stokes photons could either be seeded from another laser source or generated by the spontaneous Raman photons which are contained in the medium for subsequent conversions.

The use of high-finesse resonator and stimulated Raman process provide two traditional methods to increase conversion efficiency of the Raman transition. In these methods, the atoms in the media only play passive roles. In contrast, it has recently been discovered that Raman conversion can be enhanced greatly by taking advantage of *atomic coherence* in atomic ensembles [46]. We will briefly introduce the concept of atomic coherence and explain how the collective behavior of the atomic ensemble can enhance Raman conversion efficiency.

Let us first consider a two-level atomic system with ground state $|g\rangle$ and excited state $|e\rangle$. When we apply a coherent electromagnetic field at the resonance frequency of the atom energy level, it couples the $|g\rangle$ and $|e\rangle$ states. As a result, the atomic state undergoes a Rabi oscillation [49]. With the initial condition $|\Phi(0)\rangle_{two} = |g\rangle$,

$$|\Phi\rangle_{two} = cos^2(\Omega t/2)\,|g\rangle + sin^2(\Omega t/2)\,|e\rangle\,. \tag{4.1}$$

Here Ω is the resonance Rabi frequency $\Omega = (\vec{d}\cdot\vec{E})/\hbar$. $\vec{d}$ is the transition dipole moment and $\vec{E}$ is the applied electric field.

After the electromagnetic field is applied, a large collection of identical two-level atoms in the atomic ensemble begin the Rabi oscillations at the same time and are

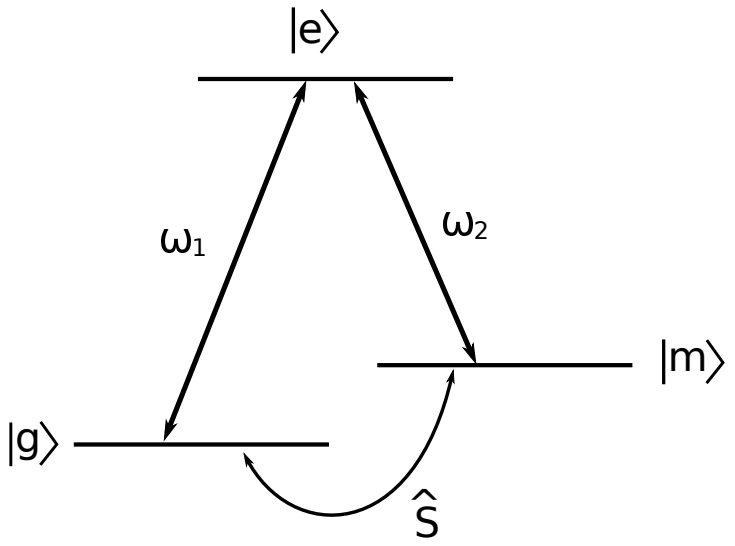

Figure 4.1. Three-level atom in a Λ-configuration. $\hat{S}$ is the atomic spin wave connecting the states $|g\rangle$ and $|m\rangle$.

in phase with each other. Under this condition, the atoms in the ensemble can no longer be treated as a collection of independent atoms. Instead, the atom ensemble as a whole exhibits collective behavior. One example of this is the phenomenon of superradiance, which is a collective emission of an ensemble that scales up the intensity of the light beam by a factor of N^2 [42]. This is because when the emission amplitudes contributed from each atom are in phase, the intensity of the radiation is proportional to the square of the sum of the amplitudes. A coherent multi-atom Rabi oscillation at a frequency of $\sqrt{N}\Omega$ is observed [43]. Here N is the number of atoms in the interaction volume.

The analysis of the atomic coherence can be extended from a two-level system to a three-level system. Consider a three-level system in a Λ-configuration as shown in Figure 4.1. $|g\rangle$ and $|m\rangle$ are two ground states and $|e\rangle$ is the excited state. The transitions $|g\rangle \leftrightarrow |e\rangle$ and $|m\rangle \leftrightarrow |e\rangle$ are dipole allowed and transition $|g\rangle \leftrightarrow |m\rangle$ is dipole forbidden. The Hamiltonian is

$$\hat{H} = \hat{H}_0 + \hat{H}_1 \tag{4.2}$$

with

$$\hat{H}_0 = \hbar\omega_g \left|g\right\rangle \left\langle g\right| + \hbar\omega_m \left|m\right\rangle \left\langle m\right| + \hbar\omega_e \left|e\right\rangle \left\langle e\right| \tag{4.3}$$

$$\hat{H}_1 = -\frac{\hbar}{2}(\Omega_1 e^{-i\omega_1 t} \left|g\right\rangle \left\langle e\right| + \Omega_2 e^{-i\omega_2 t} \left|m\right\rangle \left\langle e\right|) + H.c. \tag{4.4}$$

Here Ω_1 and Ω_2 are the Rabi frequencies of the two applied fields and H.c. stands for Hermitian conjugate. The wave function can be generally written as

$$\left|\Phi\right\rangle_{three} = c_1(t) \left|g\right\rangle + c_2(t) \left|m\right\rangle + c_3(t) \left|e\right\rangle . \tag{4.5}$$

By solving the Schrödinger equation $i\hbar\frac{\partial}{\partial t} \left|\Phi\right\rangle_{three} = \hat{H} \left|\Phi\right\rangle_{three}$ with initial conditions, we can obtain the following solutions for c_1, c_2, and c_3

$$c_1 = \frac{\Omega_2}{\sqrt{\Omega_1^2 + \Omega_2^2}} \tag{4.6}$$

$$c_2 = -\frac{\Omega_1}{\sqrt{\Omega_1^2 + \Omega_2^2}} \tag{4.7}$$

$$c_3 = 0. \tag{4.8}$$

All of the atom populations are trapped in the ground states $\left|g\right\rangle$ and $\left|m\right\rangle$. There is no probability that the atom can be excited to the excited state $\left|e\right\rangle$. This phenomenon is known as coherent population trapping (CPT). In such a state, the atoms can no longer absorb or emit any photons and the medium essentially become transparent to the incoming electromagnetic field even though the applied field is at resonance frequency of the atom transition levels. A strong "coupling" beam and a weak "probe" beam permit the propagation of the "probe" beam through the otherwise opaque medium. This phenomenon is known as electromagnetically induced transparency (EIT) [44]. In the process of EIT, the collective atomic excitation state is created and can be written as follows

$$\left|\Phi\right\rangle = \frac{1}{\sqrt{N}} \sum_j \left|g...m_j...g\right\rangle , \tag{4.9}$$

Here N refers to the total number of atoms in the interaction volume and $|g...m_j...g\rangle$ means that all the atoms are in the ground states except for the j-th atom which is in the metastable state $|m\rangle$. This collective excited state has only one excited atom that is delocalized over the whole ensemble [31, 32]. The collective atomic excitation is also called *atomic spin wave*.

The atomic spin wave can be prepared through the process of EIT to coherently enhance the coupling coefficient and the frequency conversion efficiency [45, 46]. The atomic spin wave can also be prepared through an off-resonance Raman process [33,34] and be used to enhance Raman conversion efficiency. In the Raman enhancement process, the atomic spin wave is generated by an initial Raman process. After that, the atomic spin wave acts as a seed to enhance the later Raman amplification process.

The atomic ensemble as a whole is considered as a single quantum-mechanical system. Under the condition of weak excitation, the atomic spin wave operator $\hat{S}$ can be written as follows

$$\hat{S} = \frac{1}{\sqrt{N}} \sum_j |g...g\rangle \langle g...m_j...g| , \tag{4.10}$$

Here $|g...g\rangle$ is the collective ground state with all the atoms in the ground state $|g\rangle$. And $|g...m_j...g\rangle$ represents all atoms in the ground g-state except for the j-th atom which is in the m-state. Operator $\hat{S}$ is the annihilation operator for the atomic spin wave. The atomic spin wave operators approximately satisfy the bosonic commutation relation $[\hat{S}, \hat{S}^\dagger] \approx 1$. So the generated atomic spin wave can be treated as a bosonic field in a three-wave mixing process. The Hamiltonian is

$$\hat{H} = i\hbar\eta A_1 \hat{S}^\dagger \hat{a}_2^\dagger - i\hbar\eta^* A_1^* \hat{S}\hat{a}_2. \tag{4.11}$$

Here A_1 is the classical amplitude of the strong field, $\hat{a}_2$ and $\hat{a}_2^\dagger$ are the annihilation and creation operators for the weak field, and η is the coupling coefficient.

By taking advantage of the coherence built in the atomic spin wave, we can use the medium actively to enhance the Raman conversion efficiency. In the following

section, we experimentally demonstrate a scheme of efficient Raman conversion that is relatively easy to implement compared with other EIT schemes, while still achieving high conversion efficiency. The experimental setup is illustrated and described. Experiment results are then presented followed by a discussion.

4.2 Experimental Setup

The experimental setup is shown in Figure 4.2. Two diode lasers are used: one is a commercial master-slave laser system from Sacher Lasertechnik company, and the other is a home-built external cavity diode laser (ECDL). The former includes a slave diode laser and a master oscillator power amplifier (MOPA) that can scale the power up to around $400mW$. This laser is used as our Raman pump laser or writer (W) laser, since the function of the laser is to write quantum information into atoms in quantum memory experiments [28]. The ECDL operates at peak power of $25mW$ [23, 24]. It is used as our optical pump (OP) laser. The wavelength of both lasers is tuned to $852nm$ to match the energy level of cesium D2 line. This is achieved by adjusting the diode temperature and input current, and the piezo voltage of the external cavity. A Fabry-Pérot interferometer (FPI) is aligned to monitor the mode hopping of both lasers and ensure that the lasers are stabilized at a single mode (not shown in the figure). Vibrations and temperature fluctuations may also cause the frequency to shift over time. An IR camera is used to monitor that the laser is at resonance frequency with cesium atoms. The temperature and current are controlled by an LDC-500 laser diode controller and a TEC-2000 temperature controller from Thorlabs company.

The stability of the OP laser is achieved by frequency modulation (FM) saturation spectroscopy [25]. A small portion of the main beam is redirected for laser locking as shown on the left top segment of Figure 4.2. The beam is further split into two beams by a 10:90 beam splitter that are sent through a Cesium vapor cell in a counter-propagating manner. A photo-detector is placed at the end of the vapor cell to detect

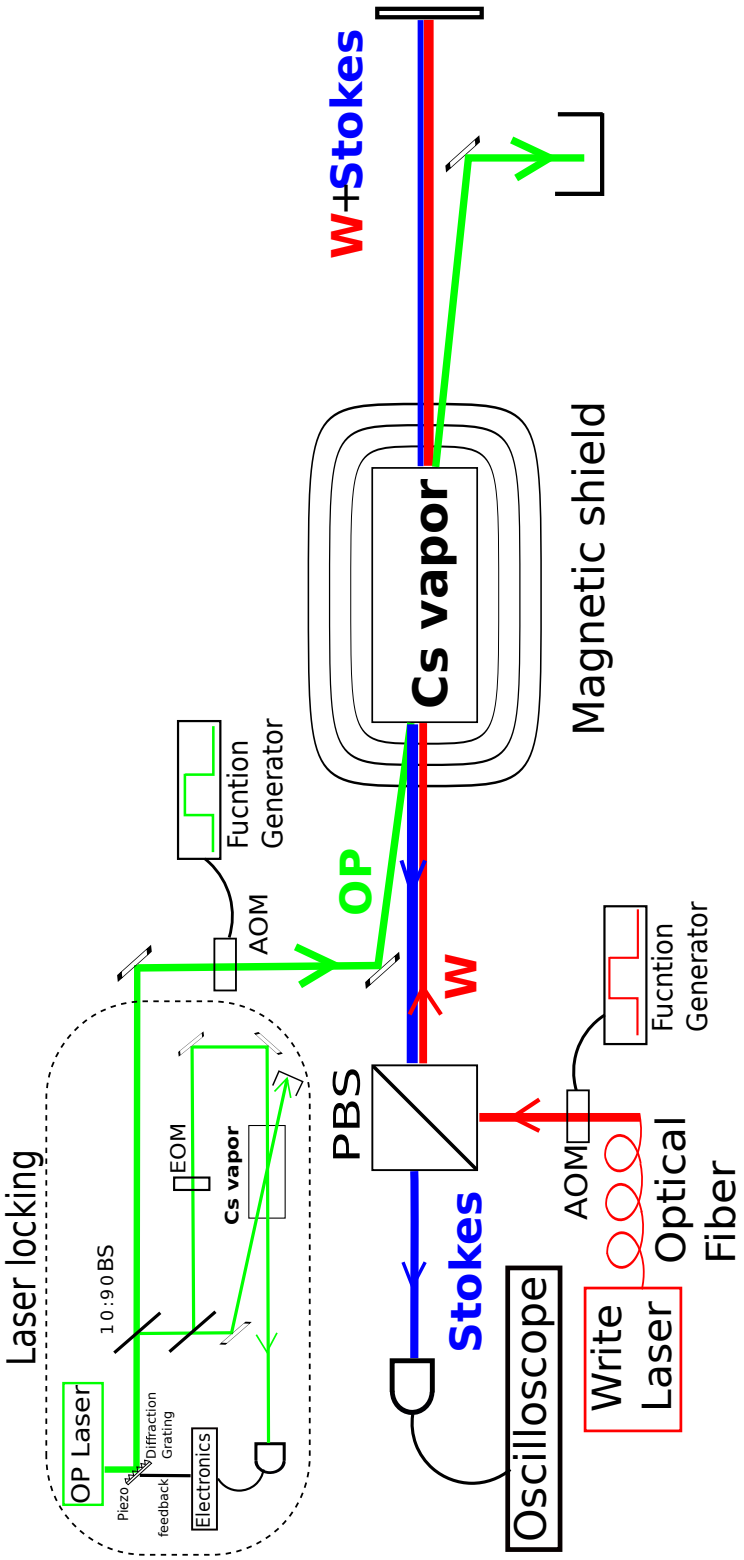

Figure 4.2. A schematic diagram for the efficient Raman conversion experiment. PBS: polarized beam splitter. EOM: electro-optic modulator. AOM: acousto-optic modulator. OP: optical pump laser. W: writer laser.

the absorption profile of the weak beam. The laser frequency is scanned by applying a ramp voltage to the piezo that is attached to the diffraction grating, which plays the role of a mirror in the diode laser external cavity. A snapshot of the absorption line in our experiment is shown in Figure 4.3. The overall dip of the absorption line is due to Doppler broadening and is about $1GHz$ wide. The small peaks are the transition lines of each hyperfine splitting of the excited state (three hyperfine lines and three crossover lines). We could further narrow our voltage scan to the selected peak and eventually lock our laser frequency to that spectrum peak when the electronic feedback is applied to the piezo on the diffraction grating. In our experiment, we choose to lock the laser to the excited state $6^2P_{3/2}, F' = 4$. Additional technical details of the laser locking experimental setup can be found at Reference [26].

Besides its usefulness in laser locking in our experiment, the saturation absorption line in Figure 4.3 is also used to determine whether the transition line is excited from the ground state $6^2S_{1/2}, F = 3$ or $6^2S_{1/2}, F = 4$. This is because the energy difference between ground states $6^2S_{1/2}, F = 3$ and $6^2S_{1/2}, F = 4$ corresponds only about $0.02nm$, which reaches the resolution limit of our optical spectrum analyzer. Also, the mode-hop-free frequency of our laser is less than the difference between these two transition lines. So in order to determine which energy level the laser is resonant with, the separation between hyperfine line peaks is measured and the ratios are calculated. If the atoms are pumped from ground state $6^2S_{1/2}, F = 4$, the separation from the most left peak to the most right peak in the absorption line is 450MHz, and the ratio of two energy gaps is $\frac{F'5-F'4}{F'4-F'3} = \frac{5}{4}$. On the other hand, if the atoms are pumped from ground state $6^2S_{1/2}, F = 3$, the separation from the most left peak to the most right peak in the absorption line is $350MHz$, and the ratio of two energy gaps is $\frac{F'4-F'3}{F'3-F'2} = \frac{4}{3}$ [16]. By measuring and comparing the separations of the peaks in the absorption line or the ratios as mentioned above, we are able to determine the specific transition lines and differentiate the Stokes generation from anti-Stokes generation.

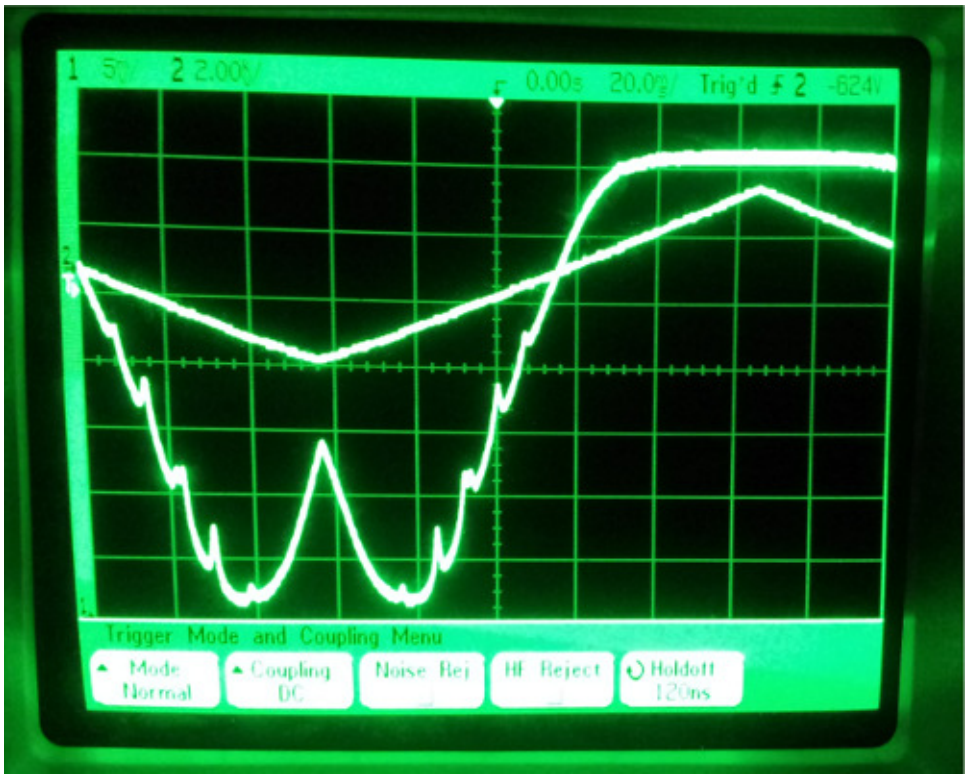

Figure 4.3. A snapshot of the oscilloscope showing the saturation absorption profile of the cesium atoms. The FWHM of the large dip is about $1GHz$ and is caused by the Doppler effect. The small peaks represent its hyperfine energy levels and corresponding crossover lines.

Figure 4.4. The cylindrical cesium vapor cell used in the lab has a radius of $2.5cm$ and length $10cm$. The paraffin coated glass cell is evacuated and filled with a small quantity of cesium. The cesium is in the form of solid particles at room temperature. At low pressure ($\sim 10^{-6}Torr$), a small portion of the Cs vaporizes and the diluted Cs vapor spreads throughout the glass cell.

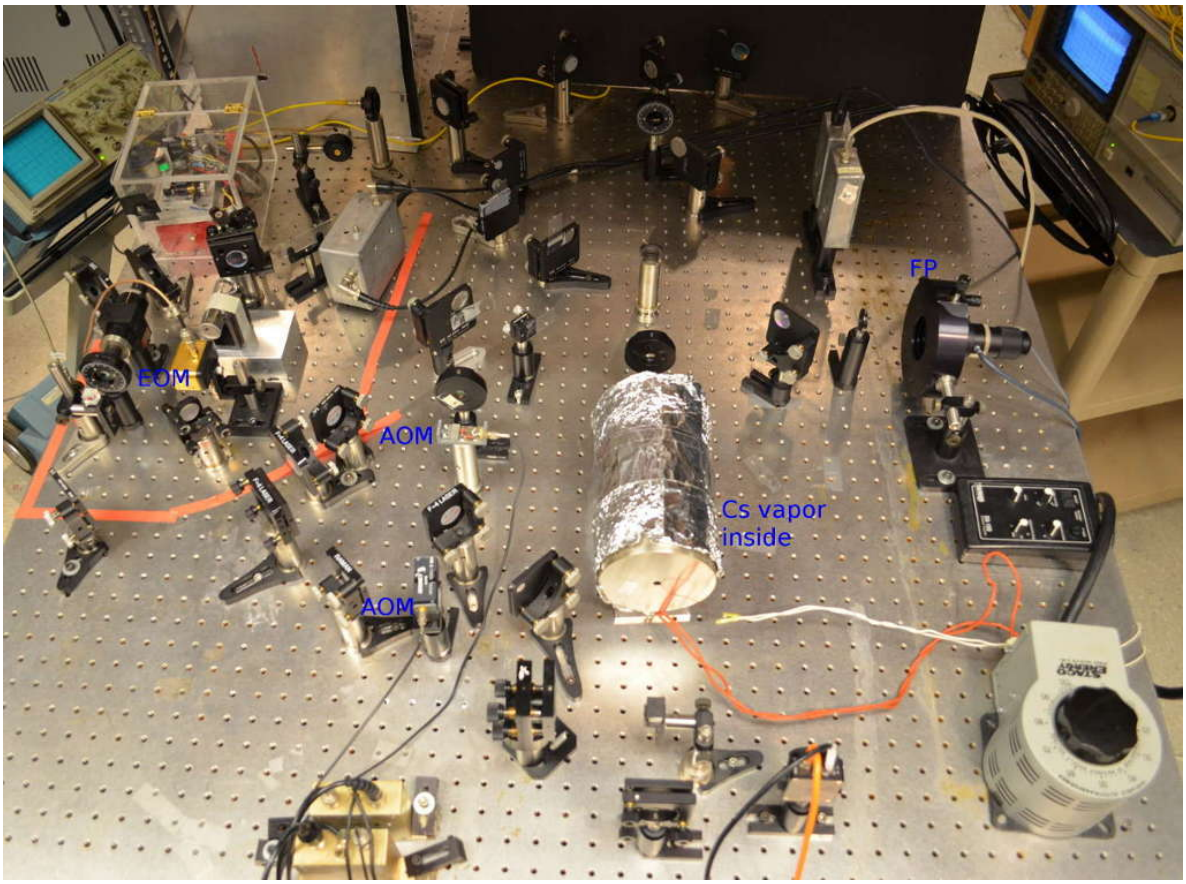

Figure 4.5. A photograph of the experimental setup (Electronic control devices are not included). The left top corner inside the orange line is equipment for laser locking. The W laser is transmitted through an optical fiber (top left). EOM: electro-optic modulator. AOM: acousto-optic modulator. FP: Fabry-Pérot interferometer.

Laser pulses are generated by acousto-optic modulators (AOM). The amplitude and the timing of the pulses are controlled by two synchronized function generators. The pulses are then aligned to the cesium vapor cell.

Several precautions were taken into considerations.

First, cesium atoms depolarize and reduces the coherence time of the atomic ensemble upon collision with the surface of the glass cell. In order to minimize such depolarization effect, paraffin (C_nH_{2n+2}) coating was placed on the inner surface of the cell to prevent wall collisions [48]. In addition, the atoms move out of the interaction volume because of diffusion whose effects can be estimated. For a given temperature, we can use the Maxwell-Boltzmann distribution to calculate the most probable speed of the atoms

$$v_p = \sqrt{\frac{2kT}{m}} \tag{4.12}$$

The diameter of the beam is typically ~ 3 mm. So the average time it takes for an atom to move out of the interaction volume is on the order of $\sim 10^{-5}$s. One way to increase the interaction time is to increase the beam diameter, but this comes at a cost of reducing the light intensity. Another way to increase the interaction time is to mix the cesium with a noble gas [37]. The diffusion time of the Cs atoms with neon gas mixed in has been studied [38]. The diffusion time is given as $t = r^2/4D^2$, where r is the beam radius and D is the diffusion coefficient. We filled the vapor cell with neon buffer gas and prolonged the coherence time of the cesium atomic ensemble to $\sim 1.8ms$ in the experiment.

Second, the Earth's magnetic field may undesirably split cesium energy levels due to the Zeeman effect. Thus, the vapor cell is placed inside a three-layer μ-metal cylinder to shield against stray magnetic fields.

Third, cesium is in the solid state at room temperature (melting point is 28 °C). To increase the density of cesium vapor in the cell, a bifilar resistive heater is wound outside of the μ-metal cylinder to heat the cesium atoms. However, the paraffin coating on the cell starts to melt and become ineffective when the temperature is

above 80 °C. So as a compromise, the temperature was controlled at 70 °C in our experiment. A picture of the vapor cell is shown in Figure 4.4.

And finally, the laser beams are aligned as shown in Figure 4.2. The OP laser only passes through the Cesium vapor once, while the W laser passes through the vapor and is reflected back by a mirror. The forward beam and reflected beam overlap within the cesium vapor cell. The generated Stokes field and the original Raman pump are both reflected back to the cesium vapor cell. The Stokes beam is then separated from the Raman pump by a polarized Beam Splitter (PBS) and received by a photo-detector. A photograph of the equipment setup is shown in Figure 4.5.

4.3 Experimental Results and Discussions

We first verify the experimental setup by examining the frequency shift of the converted Raman field. We align both the W laser beam and the generated Raman beam to a scanning Fabry-Pérot cavity with free spectral range (FSR) of $8.0GHz$. The graphs of both the Stokes and anti-Stokes show a frequency shift of $9.2Ghz$ between the W laser and the Raman beams. $9.2GHz$ matches the frequency separation between the cesium atom energy levels $6^2S_{1/2}, F = 3$ and $6^2S_{1/2}, F = 4$. From the graph, we see that the frequency of the Stokes field is $9.2Ghz$ less than the W laser with the peak shifting to the right; the frequency of the anti-Stokes field is $9.2GHz$ higher than the W laser with the peak shifting to the left as shown in Figure 4.6.

The temporal behavior of the converted field is shown in Figure 4.7. The OP laser pulse is first turned on for $\sim 2ms$ to pump all cesium atoms to the ground state of $6^2S_{1/2}, F = 3$ in the case of the Stokes generation, and the state of $6^2S_{1/2}, F = 4$ in the case of the anti-Stokes generation. After the OP pulse is turned off for a short time ($\sim 0.3ms$), the W laser pulse is turned on for $\sim 5ms$ to interact with the cesium ensemble and to generate the Stokes field. The intensity of the Stokes field peaks quickly and then decays due to atomic decoherence. The cause of the decoherence could be understood as that the cesium atoms diffuse out of the laser-interaction

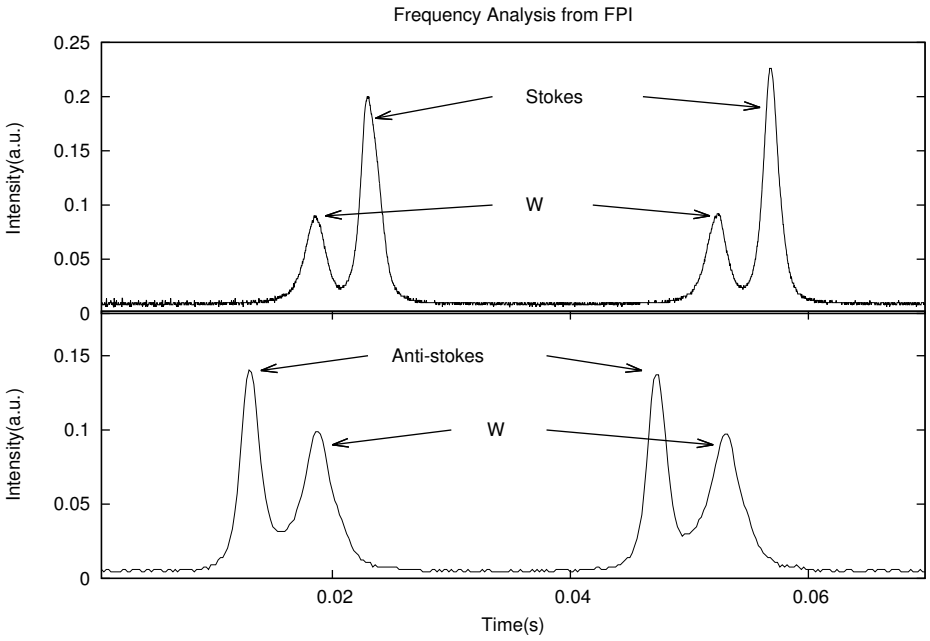

Figure 4.6. Frequency analysis of the signal detected in a Fabry-Pérot interferometer (FPI). The free spectral range (FSR) of the FPI is $8.0Ghz$. In the Stokes Raman process, the frequency of the generated field increases 9.2 GHz, which corresponds to the energy difference between ground states $6^2S_{1/2}, F = 3$ and $6^2S_{1/2}, F = 4$. In the anti-Stokes process, the frequency of the generated field decreases $9.2GHz$.

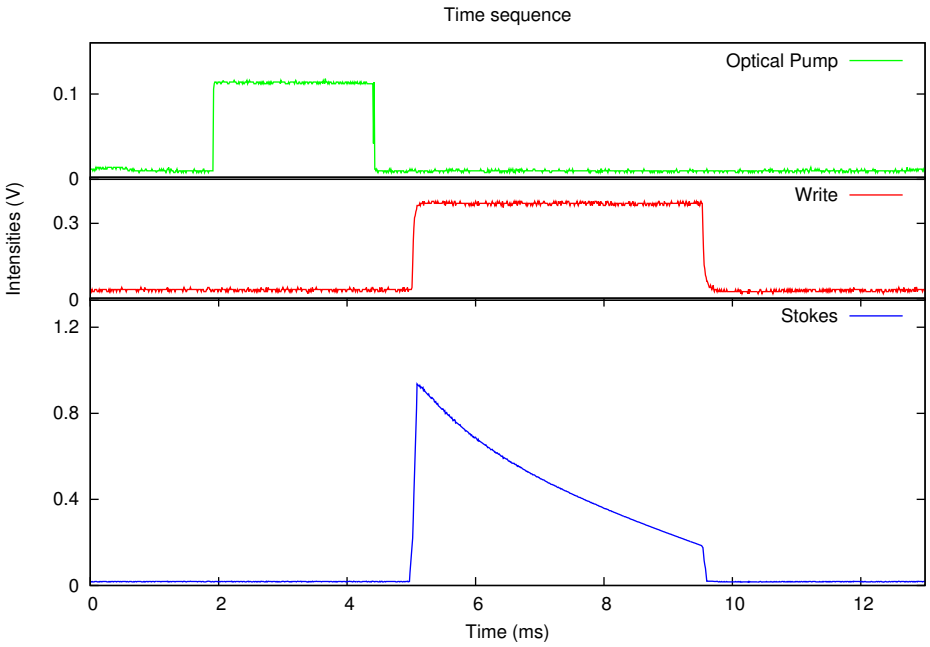

Figure 4.7. Temporal behavior of the OP, W and Stokes fields. The OP pulse is first applied for $\sim 2ms$ to pump all of the atom populations to ground state $6^2S_{1/2}, F = 3$. Shortly after the OP pulse is turned off, the W laser pulse is applied to generate the Stokes field. The Stokes field intensity peaks quickly and then decays due to atomic decoherence. The decoherence time is $\sim 1.8ms$.

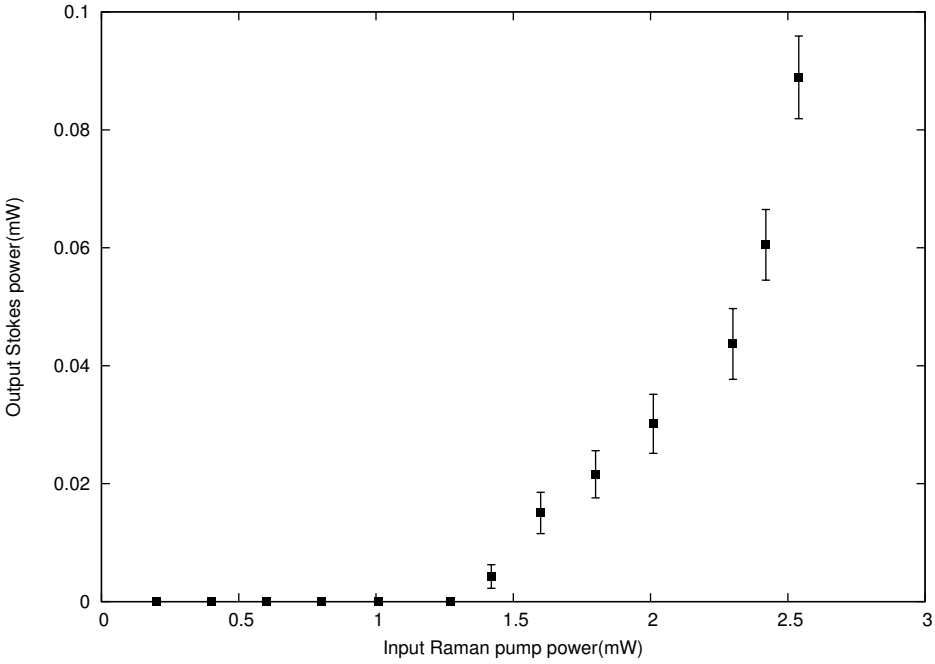

Figure 4.8. The Stokes field as a function of the Raman pump field power. It clearly shows a Raman conversion threshold. When the input Raman pump power is lower than $1.2mW$, there is no output Stokes power at all. When the input Raman power reaches the threshold at $1.2mW$, the Stokes field begins to be generated.

volume and the collisions at the glass cell. The decoherence time recorded depends on the cesium vapor density and the detuning of the W laser. A typical value of the decoherence time of our system is $\sim 1.8ms$.

We further investigated the system by changing the Raman pump field power while monitoring the output power of the Stokes field. Figure 4.8 shows the Stokes field output power as a function of input Raman pump power. It shows a laser-like power threshold for the Raman conversion. The value of the threshold depends on the frequency detuning of the Raman pump and the temperature of the vapor cell. The threshold power ranges from $300\mu W$ to $3mW$ in our experiment. This can be understood that when the power of the W beam is low, only spontaneous Raman photons are generated. When the W power reaches the threshold, the Raman process takes place first in the form of spontaneous Raman scattering and is subsequently

amplified by the coherent stimulated Raman process. Because of the low coupling coefficient between the atoms and the laser beams, generally large power is required to initiate the Raman conversion. As a comparison, the threshold power required for other gas-phase systems can be as large as $\sim 1MW$ [39].

Note that the system we have here is similar to a Raman laser but without reflecting mirrors. So it is a single-pass, mirrorless Raman laser. Single-pass lasers require a strong pump field, typically in a pulse mode and is focused to have high power density. In contrast, our system works with a low power Raman pump in the cw mode and without focus of the laser beam.

To understand the laser-like low threshold phenomenon, a new theory was developed based on a general three-wave mixing process [40]. Besides the Raman pump field and Stokes fields, the atomic spin wave operator was introduced as a third wave. As the the Raman pump field and Stokes field propagate through the medium, the atomic spin wave stays inside but dephases with a given decoherence coefficient. It was found that the threshold of such a system is inversely proportional to the atomic decoherence time and independent of the optical feedback, which plays a critical role in other laser systems. Because of the long coherence time of our atomic ensemble ($\sim 2ms$), the pump threshold required to generate Stokes field becomes quite low.

Next, we compare the efficiency of Raman conversion when the W laser double passes the cesium with that when the W laser passes the Cesium only once. The double-pass scheme is shown in Figure 4.2. The single-pass experiment can be simply done by replacing the reflecting mirror behind the vapor cell with a PBS and a photodetector. The Stokes beam is separated from the W beam because the polarizations of them are orthogonal to each other. The experimental result is plotted in Figure 4.9. A quick observation of the plot informs us that the efficiency increase for the double-pass is more than two-fold of that for the single-pass. It shows that the second passage is not a simple repeat of the single-pass experiment. Instead, it is a coherent enhancement process. In other words, the conversion efficiency is not an intensity sum

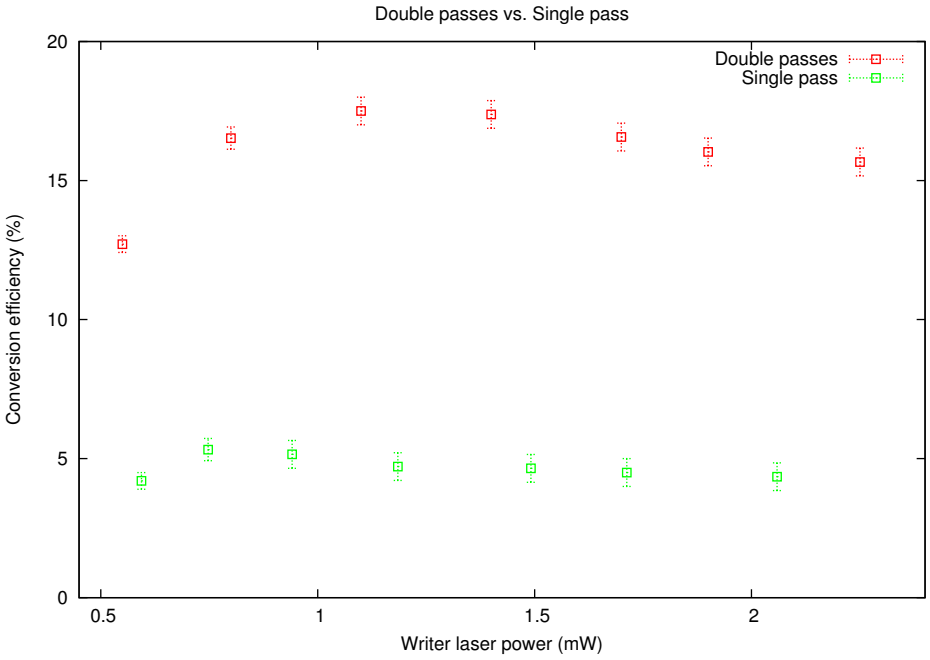

Figure 4.9. Comparison of Raman conversion efficiency, defined as the ratio of the generated Stokes field power to the input Raman pump field power. The red bar represents the efficiency for a double passes of the W field and the generated Stokes field. The green bar represents the efficiency for a single pass of the W field.

of that of each single-pass $I_{net} \neq I_1 + I_2$, but a coherent sum of probability amplitudes $I_{net} = |A_1 + A_2|^2$. Here A is the amplitude and I is the intensity $I_1 = |A_1|^2$, $I_2 = |A_2|^2$.

Magnetic field shielding is crucial for the success of the experiment. This is because even a magnetic field as small as the earth's magnetic field can cause splitting in the degenerate energy levels due to the Zeeman effect. As a result, the Raman frequency generated from each Zeeman sub-levels differs slightly. Thus the Raman intensities generated from each sub-levels no longer contribute coherently. Take the energy level $6^2S_{1/2}, F = 4$ for example, there are 9 Zeeman sub-levels under the influence of magnetic field, $m_F = -4, -3, ..., 4$. Assume a uniform population distribution among the sub-levels and the same coupling coefficient of each Raman process, the overall intensity of a Raman generation would be a sum of each sub-level, $I_{total} = \sum_{i=1}^{9} I_i = 9I_1$. Without the magnetic field, the energy levels are degenerate, and the total intensity is a coherent sum of intensities of each sub-level, $I_{total} = (\sum_{i=1}^{9} A_i)^2 = 81I_1$. We see the intensity in degenerate case is 9 times higher than the non-degenerate case. This analysis is based only on the splitting in the $F = 4$ energy level. Raman conversion is a two-photon process and two energy levels are coupled. As a result, the energy splitting would dramatically reduce the Raman conversion efficiency.

To test this effect, we wrapped a coil around the glass cell as a solenoid and place the cell inside the magnetic shielding. The coil is connected to a power supply and an ammeter. With a current input between $-0.01A$ and $0.01A$, the Stokes signal maintains at the same value. However, as soon as the current passes more than $0.01A$ or less than $-0.01A$, the Stokes field suddenly disappears. A quick calculation shows that a supply of $0.01A$ current corresponds to a magnetic field value $B = 2\mu T$, or a tenth of earth's magnetic field. The negative current just means a magnetic field with opposite direction. In anti-Stokes generation, the same phenomenon is observed with the breakup point measured at $B = 6\mu T$.

To see how different parts of the system contribute coherently to the Stokes field generation, we refer back to the three wave mixing process equations derived in the

chapter "Nonlinear Optics." The input-output relations of the Stokes operator and atomic spin wave operator at a strong Raman pump can be written as

$$\hat{a}_{s,out} = \cosh(|\eta A_w|t)\hat{a}_{s,in} - e^{i\varphi}\sinh(|\eta A_w|t)\hat{a}^{\dagger}_{asw,in} \tag{4.13}$$

$$\hat{a}_{asw,out} = \cosh(|\eta A_w|t)\hat{a}_{asw,in} - e^{i\varphi}\sinh(|\eta A_w|t)\hat{a}^{\dagger}_{s,in} \tag{4.14}$$

Here $\hat{a}_{s,in}$ and $\hat{a}_{asw,in}$ are Stokes and atomic spin wave inputs. $\hat{a}_{s,out}$ and $\hat{a}_{asw,out}$ are the Stokes and atomic spin wave outputs after some interaction time t. η is the coupling coefficient. Subscripts s and asw represent the Stokes and the atomic spin wave respectively. φ is relative phase. The strong and undepleted W field is represented by a classical amplitude A_w. Decoherence of the atomic spin wave and spatial change of the Stokes field are not considered. Under those conditions, the output intensity of the Stokes field can be written as

$$I_{s,out} = \alpha\hbar\omega\left\langle \hat{a}^{\dagger}_{s,out}\hat{a}_{s,out}\right\rangle \tag{4.15}$$

α is the overall coefficient that depends on the strength of the field, density of the atomic ensemble and coupling coefficient between the Stokes field and the atomic spin wave.

By plugging Equation 4.13 into Equation 4.15, we have

$$\begin{aligned} I_{s,out} =& \alpha\hbar\omega\Big(\sinh^2(|\eta A_w|t)\left\langle \hat{a}_{asw,in}\hat{a}^{\dagger}_{asw,in}\right\rangle \\ &+ \cosh^2(|\eta A_w|t)\left\langle \hat{a}^{\dagger}_{s,in}\hat{a}_{s,in}\right\rangle \\ &+ e^{-i(\varphi+\pi)}\sinh(|\eta A_w|t)\cosh(|\eta A_w|t)\left\langle \hat{a}_{asw,in}\hat{a}_{s,in}\right\rangle \\ &+ e^{i(\varphi+\pi)}\sinh(|\eta A_w|t)\cosh(|\eta A_w|t)\left\langle \hat{a}^{\dagger}_{asw,in}\hat{a}^{\dagger}_{s,in}\right\rangle \Big) \end{aligned} \tag{4.16}$$

Note the creation and annihilation operators in the first term of Equation 4.16 are not in the normal order. Following the commutation relation, we have

$$\left\langle \hat{a}_{asw,in}\hat{a}^{\dagger}_{asw,in} \right\rangle = \left\langle \hat{a}^{\dagger}_{asw,in}\hat{a}_{asw,in} + 1 \right\rangle \tag{4.17}$$

By putting Equation 4.17 into Equation 4.16, we obtain four terms for $I_{s,out}$

$$I_{s,out} = I_1 + I_2 + I_3 + I_4 \tag{4.18}$$

I_1 corresponds to the spontaneous Raman emission.

$$I_1 = \alpha\hbar\omega \sinh^2(|\eta A_w|t) \tag{4.19}$$

I_2 corresponds to the Raman conversion contributed by the atomic spin wave.

$$I_2 = \alpha\hbar\omega \sinh^2(|\eta A_w|t) \left\langle \hat{a}^{\dagger}_{asw,in}\hat{a}_{asw,in} \right\rangle \tag{4.20}$$

I_3 corresponds to the stimulated Raman conversion produced by the seeded Stokes field.

$$I_3 = \alpha\hbar\omega \cosh^2(|\eta A_w|t) \left\langle \hat{a}^{\dagger}_{s,in}\hat{a}_{s,in} \right\rangle \tag{4.21}$$

I_4 corresponds to the Stokes and atomic spin wave correlation enhancement mechanism [50].

$$I_4 = \frac{\alpha\hbar\omega}{2}\left(e^{-i(\varphi+\pi)} \sinh(2|\eta A_w|t) \left\langle \hat{a}_{asw,in}\hat{a}_{s,in} \right\rangle + H.c\right) \tag{4.22}$$

Note with an undepleted Raman pump field, the Hamiltonian of the Raman process is the same as that of spontaneous parametric down-conversion. Thus the Stokes and atomic spin wave would have the same correlation found in the signal field and idle field in spontaneous parametric down-conversion. This correlation contributes to the Raman conversion in term I_4.

To see more clearly how each of the terms contributes to the Raman conversion, an illustrative figure is shown in Figure 4.10. In the first passage of the Raman pump field, the intensity of the Stokes field is the sum of the initial spontaneous Raman scattering and the subsequent stimulated Raman process. In the second passage,

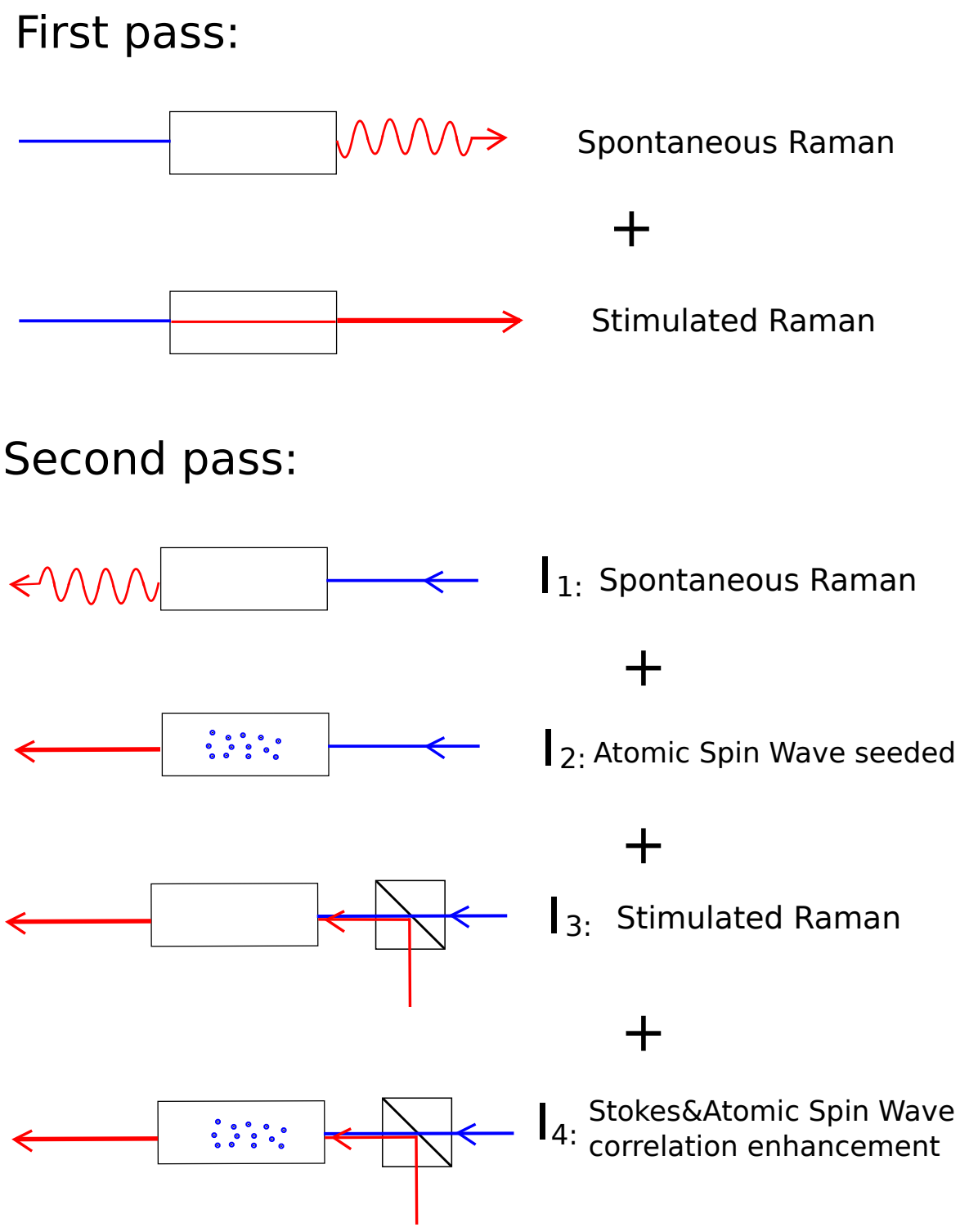

Figure 4.10. An illustrative figure that shows how each term enhances the Stokes field generation. In the first passage, it has only spontaneous Raman and stimulated Raman generation. In the second pass, besides the spontaneous Raman and stimulated Raman, the atomic spin wave generated from the first passage contributes to the third term (I_3) and fourth terms (I_4) in the expression for Stokes field output.

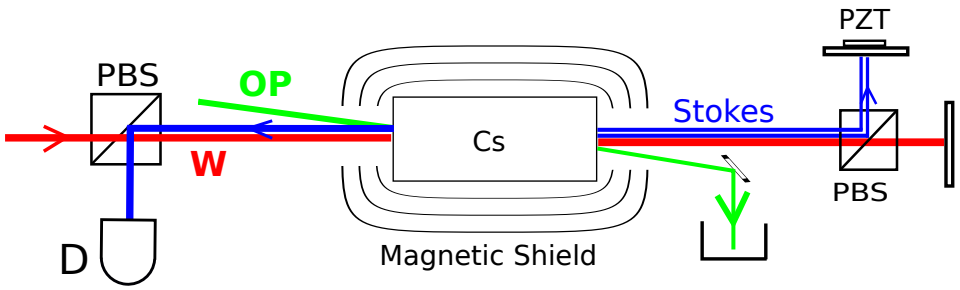

Figure 4.11. Schematic drawing for the phase dependence experiment. The Stokes and the W beams are separated by a PBS. A PZT is applied to the W beam to scan the relative phase between the W and the Stokes fields. OP: optical pump beam. W: writer beam. PBS: polarized beam splitter. D: photo-detector. PZT: piezo transducer.

along with the spontaneous Raman scattering (I_1) and Stimulated Raman process (I_2), the atomic spin wave created in the first passage is seeded to enhance the Raman process (I_3). Moreover, the correlation between the Stokes and atomic spin wave adds extra enhancement to the Raman process (I_4).

From Equation 4.22 we see that I_4 is phase sensitive. The Stokes field intensity contributed from I_4 is dependent on the relative phase of the Raman pump field and the seeded Stokes field. In the case of $\varphi = \pi$, both terms in Equation 4.22 are positive and constructively contributes to the overall Stokes intensity. In the case of $\varphi = 0$, both terms in Equation 4.22 are negative and destructively contribute to the overall Stokes intensity.

To observe the phase dependence effect, we separated the Stokes and W fields after the fist pass and scanned the phase of the W beam before the second pass. The experimental setup is shown in Figure 4.11. Since the W field and Stokes field have orthogonal polarizations, we inserted a polarized beam splitter between the vapor cell and the reflecting mirror so that the Stokes and W beams are separated before both of them are reflected back. A PZT is attached to the W field mirror to scan the relative phase. The Stokes field is detected at the photo-detector (D). The result of the experiment is shown in Figure 4.12. The top graph is the voltage applied on the

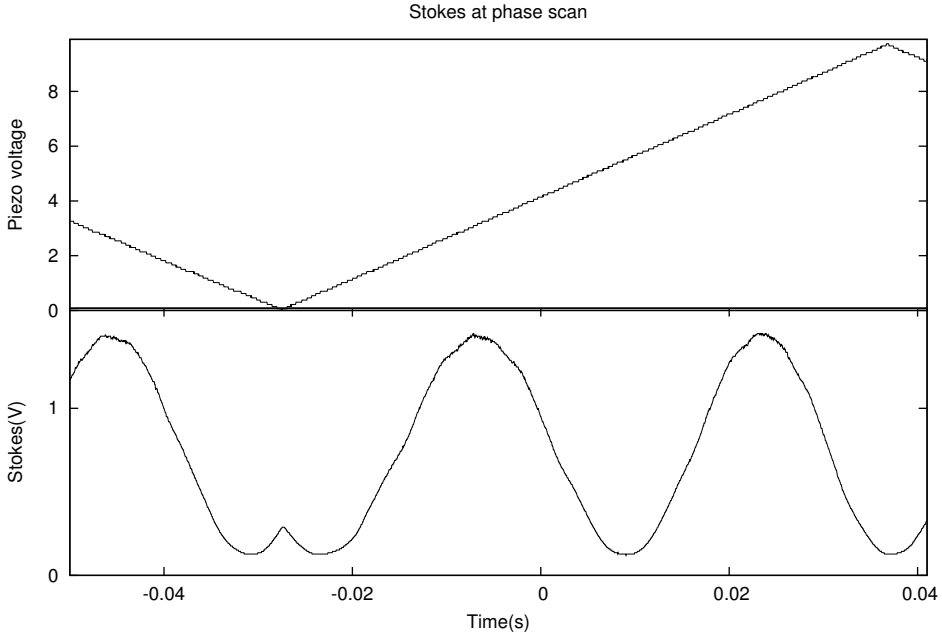

Figure 4.12. A phase scan is applied to the W field. Because there is a phase correlation between the Stokes field generated in the first pass and the atomic spin wave, the Stokes field generated in the second pass would interfere with the Stokes field generated in the first pass. Top trace: A ramp voltage is applied to the W field. Bottom graph: An interference fringe is detected at the photo-detector.

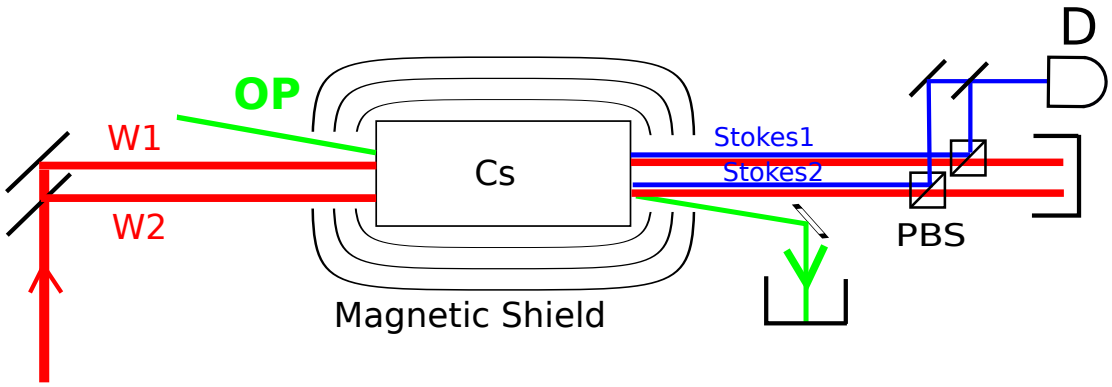

Figure 4.13. Two W beams (W1 and W2) pass through the same cesium vapor cell. Two Stokes fields (Stokes1 and Stokes2) are generated from each W beam and are superimposed at the photo-detector (D). A beat signal is detected due to the AC Stark effect. OP: Optical pump laser. W1, W2: Writer lasers. PBS: Polarized beam splitter. Cs: Cesium vapor cell.

PZT. The bottom graph is the corresponding Stokes field intensity. The interference pattern clearly shows the phase dependence of the Stokes field.

The interference fringe can be interpreted as follows: After the fist passage of the Raman pump field, the Stokes field and the atomic spin wave have a phase correlation. It is the same correlation that the signal field and idler field have in parametric down-conversion process. After the first passage, the phase information is stored in the atomic spin wave and is later retrieved when the Raman pump is reflected back and passes the atoms the second time. This phase information is carried by the Stokes field generated in the second pass and then interferes with the Stokes field generated in the first pass that is reflected back from the the flat mirror.

Finally, we check the coherence of the generated Stokes fields. We first split the W laser into two beams and allow them to pass through the cesium vapor cell separately as shown in Figure 4.13. The two Stokes fields (Stokes1 and Stokes2 in the Figure) generated each from the two W fields (W1 and W2) are then superimposed to check the interference.

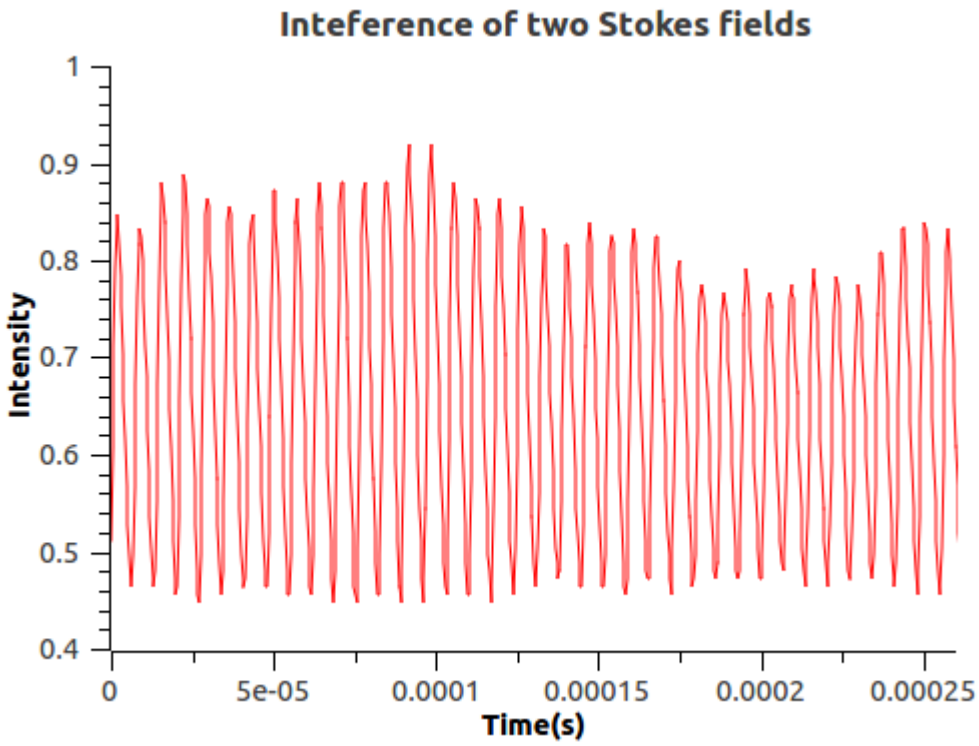

Figure 4.14. The two generated Stokes fields are superimposed to interfere. The beat signal is due to the AC Stark effect.

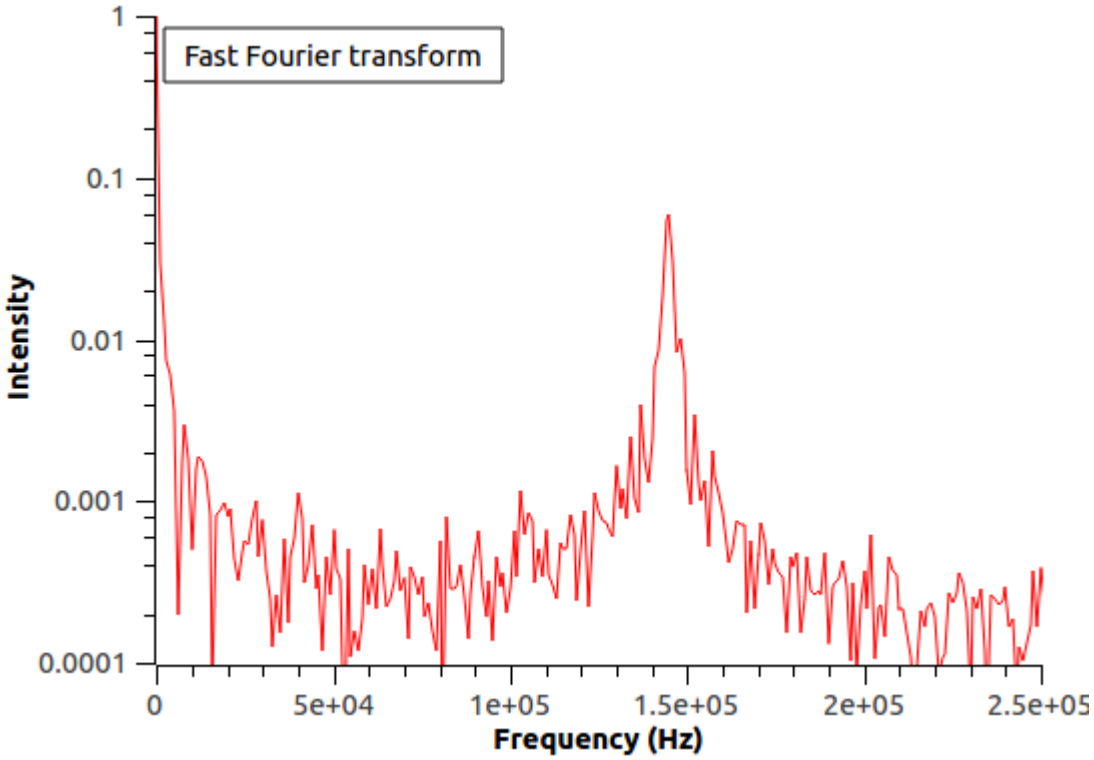

Figure 4.15. A fast Fourier transform is applied to the beat signal collected from the two superimposed Stokes fields. The peak shows the frequency difference between the two Stokes fields. The linewidth of the peak shows the coherence time of the Stokes field to be about $0.2ms$.

Data from the experiment recorded by an oscilloscope are shown in Figure 4.14. A beat signal is observed. This is because the energy levels of the atoms shift due to the AC Stark effect under the influence of high laser power. Because of the unbalanced power of the W field on each conversion, the shift of the energy levels is slightly different. Thus the frequencies of the converted Stokes fields in different geometry are also slightly different from one to another. So the superposition of these two fields leads to a beat signal. The interference signal in the time domain can be transformed to the frequency domain by a fast Fourier transform (FFT). The signal in the frequency domain is plotted in Figure 4.15. A peak is found at the frequency of $\sim 150kHz$, which corresponds to the frequency difference between the two generated Stokes fields. The Full Width at Half Maximum (FWHM) of the peak is found to be $\sim 5kHz$. This corresponds to a coherence time $\tau \simeq 0.2ms$. This coherence time is about the same order of magnitude as the coherence time we found in the temporal behavior experiment.

It is worth noting that a similar beat signal is detected in the double pass experiment. Basically, in the double pass experiment, it is required that the beam of the second pass has a spatial overlap with the beam of first pass in order to enhance the Raman conversion efficiency. However, when the forwarded beam and reflected beam are slightly misaligned, they can be treated like two partially separated beams and thus the same beat signal can be observed in the detector. As a result, this beat signal accidentally becomes a tool in our experiment to check the spatial overlap between the two counter-propagating beams.

In conclusion, we showed an experimental demonstration for efficient Raman conversion with a coherent feedback in a low density cesium vapor cell. Compared with other traditional methods to increase the Raman conversion efficiency, we take advantage of the atomic spin wave created by the Raman conversion in the first passage and coherently enhance the later Raman conversion in the second passage. We also find a laser-like threshold but with a much lower threshold power than other similar Raman systems. This low threshold can be attributed to the long coherence time of

the atomic spin wave. And finally, a beat signal due the AC Stark effect between the two Stokes fields is shown. A Fourier transform is applied to check the frequency difference and coherence time of the fields. Such techniques have potential applications in nonlinear optics and quantum information science. For example, traditionally electro-optic modulators (EOM) are used to modulate the phase of the light beams and create sidebands at higher or lower frequencies. With an easy implementation, the double pass Raman conversion can function like an EOM with a better conversion rate.

5. PRECISION PHASE MEASUREMENT VIA NONLINEAR INTERFEROMETERS

5.1 Research Background

In 1887, Michelson and Morley performed an interferometric experiment [83] to detect the so-called "aether wind." The negative results made room for alternative theories that eventually lead to Einstein's special relativity. Since then, interferometry has been investigated and applied broadly in the fields of astronomy, metrology, spectroscopy. As technologies advance, the measurement scale has become more and more precise and now enters the regime of single photons and single atoms.

On the other hand, nature puts some ultimate restrictions on how precise a physical measurement can be reached. In particular, when measuring microscopic objects, the laws of quantum mechanics govern the measurement processes. One of the fundamental laws in quantum mechanics is the Heisenberg uncertainty principle, which imposes a fundamental limit on measuring two incompatible observables simultaneously, $\Delta x \cdot \Delta p \geq \frac{\hbar}{2}$. Other than that, measurement is also constrained by limited resources. Given a certain amount of energy, the Margolus-Levitin theorem imposes a fundamental limit on measurement precision [84].

Traditionally, the precision of an interferometric phase measurement is limited by classical statistics. Consider the Mach-Zehnder interferometer in Figure 5.1 Part (a). Light fields enter the input through ports A and B. In a typical Mach-Zehnder interferometer, port B is set at vacuum mode. Input beam A is first divided into a reflected part and a transmitted part by a beam splitter BS1 as shown in the figure. These two components are recombined by a second beam splitter BS2. The phase difference φ between these two paths can be recovered by measuring the photon intensity at output port C or D. For a classical coherent state input with intensity

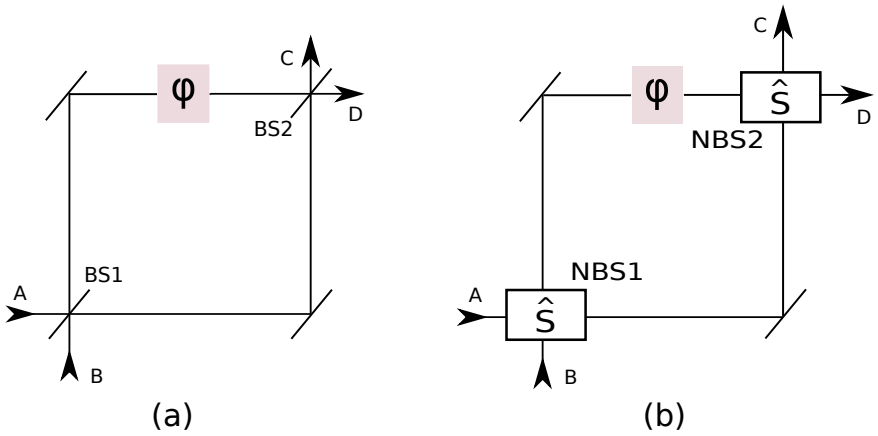

Figure 5.1. A traditional Mach-Zehnder interferometer and its nonlinear counterpart. A, B are the two input ports. C, D are the two output ports. φ is the phase delay on one branch of the divided beams. BS1 and BS2 are two beam splitters. In a nonlinear interferometer, the traditional beam splitters are replaced by nonlinear beam splitters (NBS1 and NBS2). The input-output relation of a NBS can be expressed as a scattering matrix S.

I_A at port A, the output intensity I_D at port D is a function of φ, that is $I_D = cos^2(\varphi/2)I_A$. Because of the quantized nature of electromagnetic waves, the quantity I_D is measured by counting the number of photons detected at port D. As a result, the phase measurement $cos^2(\varphi/2)$ is estimated as $\sum_{i=1}^{N} x_i/N$. Here x_i only takes two values, 0 or 1. x_i is zero if the photon is not detected at port D, and x_i is one if one photon is detected at port D. N is the total number of photons at input A. It can be easily shown that the statistical error is $\Delta(\sum_{i=1}^{N} x_i/N) = \Delta x/\sqrt{N}$. The dependence of $1/\sqrt{N}$ for the phase measurement error is known as Standard Quantum Limit (SQL) or shot noise limit [77],

$$\Delta\varphi = \frac{1}{\sqrt{N}}. \tag{5.1}$$

The $1/\sqrt{N}$ limit is only applicable for standard measurement techniques that use classical quantum states such as the coherent state. The standard quantum limit can be circumvented by preparing the input quantum states as non-classical states such

as squeezed states [74–76], or entangled states [78]. One of the entangled states that is of particular interest is the NOON state [79].

$$|NOON\rangle = \frac{|N\rangle_a |0\rangle_b + |0\rangle_a |N\rangle_b}{\sqrt{2}} \tag{5.2}$$

The NOON state is a superposition state of N-photon state in mode a with vacuum state in mode b, and vice versa. So far $N = 5$ has been realized experimentally [80,81]. Unlike the classical coherent state, the correlation in such entangled states can not be explained by any classical statistical models. The conclusion of the $1/\sqrt{N}$ dependence drawn from statistical analysis is thus not applicable.

By taking advantage of the non-classical properties of quantum states, the sensitivity of the phase measurement can surpass the shot noise limit and further approach the so-called Heisenberg limit [78]

$$\Delta\varphi = \frac{1}{N}. \tag{5.3}$$

The Heisenberg limit is governed by the Heisenberg uncertainty principle and is believed to be the ultimate quantum limit of phase measurement.

While most reports focus on approaches of using non-classical quantum states to increase the phase measurement precision, it has been reported that the change of interferometer structures can also increase the phase measurement precision [85, 86]. To see how it works, a more general scheme of interferometer is drawn in Figure 5.1 Part (b). The idea of traditional beam splitters (Figure 5.1 Part (a)) is extended to a more general nonlinear beam splitter (NBS). The function of a general beam splitter is to transform input modes to output modes by a scattering matrix S. For a traditional lossless beam splitter, as shown in Figure 5.2, the input-output relationship can be written as [73]

$$\begin{pmatrix} \hat{a}_{out} \\ \hat{b}_{out} \end{pmatrix} = S \begin{pmatrix} \hat{a}_{in} \\ \hat{b}_{in} \end{pmatrix} = \begin{pmatrix} \alpha & -\overline{\beta} \\ \beta & \overline{\alpha} \end{pmatrix} \begin{pmatrix} \hat{a}_{in} \\ \hat{b}_{in} \end{pmatrix} \tag{5.4}$$

Here the scattering matrix belongs to a special unitary group $SU(2)$:

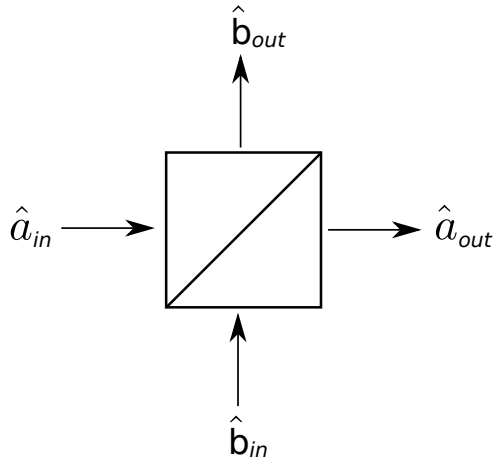

Figure 5.2. Beam splitter geometry and its input-output ports. $\hat{a}_{in}$ and $\hat{b}_{in}$ are the input modes and $\hat{a}_{out}$ and $\hat{b}_{out}$ are the output modes.

$$SU(2) = \left\{ \begin{pmatrix} \alpha & -\overline{\beta} \\ \beta & \overline{\alpha} \end{pmatrix} : \quad \alpha, \beta \in \mathbf{C}, |\alpha|^2 + |\beta|^2 = 1 \right\} \tag{5.5}$$

Yurke and his coworkers proposed a class of interferometers characterized by the group $SU(1,1)$ [85]. In such an interferometer, the passive role of beam splitters is replaced by active media such as parametric amplifiers. As a result, in contrast to conventional $SU(2)$ interferometers that have to use squeezed states or entangled states to surpass the standard quantum limit, $SU(1,1)$ interferometers can achieve a phase sensitivity of 1/N with only vacuum state and coherent state as inputs.

Here we give a comparison of the signal-to-noise ratio (SNR) between conventional linear interferometers and nonlinear interferometers realized by parametric amplifiers. The input-output relationship for a general interferometer (Figure 5.1 Part (b)) can be written as

$$\begin{pmatrix} \hat{a}_{out} \\ \hat{b}_{out} \end{pmatrix} = S \begin{pmatrix} e^{i\varphi} \\ 1 \end{pmatrix} S \begin{pmatrix} \hat{a}_{in} \\ \hat{b}_{in} \end{pmatrix} \tag{5.6}$$

For a 50:50 beam splitter, the scattering matrix is

$$S = \frac{1}{\sqrt{2}} \begin{pmatrix} 1 & 1 \\ -1 & 1 \end{pmatrix} \tag{5.7}$$

With a coherent state $|\alpha\rangle$ input at $\hat{a}_{in}$ and vacuum state input at $\hat{b}_{in}$, the output of the interferometer can be found as

$$\langle \hat{b}^{\dagger}_{out} \hat{b}_{out} \rangle_{linear} = I_{ps}(1 - cos\varphi) \tag{5.8}$$

Here I_{ps} is the amplitude of the phase-sensing field, i.e., the field that passes through the section where the phase delay φ is imposed.

A nonlinear interferometer can be realized by replacing beam splitters by parametric amplifiers. Parametric amplification is a three wave mixing process. Its interaction Hamiltonian is given by Equation 2.27. Under the condition of an undepleted pump field, the Hamiltonian becomes

$$\hat{H} = i\hbar\eta A_p \hat{a}_s^\dagger \hat{a}_i^\dagger - i\hbar\eta^* A_w^* \hat{a}_s \hat{a}_i. \tag{5.9}$$

Here η is the coupling coefficient and subscripts p, s, i stands for pump field, signal field and idler field respectively. By plugging the Hamiltonian into Heisenberg's equations of motion (Equation 2.29) and using the commutation relations (Equation 2.30), we can solve the equations and determine the input-output relations for the parametric amplifier.

$$\begin{pmatrix} \hat{a}_{out} \\ \hat{b}_{out}^\dagger \end{pmatrix} = \begin{pmatrix} \cosh(|\eta A_p t|) & -i\sinh(|\eta A_p t|) \\ i\sinh(|\eta A_p t|) & \cosh(|\eta A_p t|) \end{pmatrix} \begin{pmatrix} \hat{a}_{in} \\ \hat{b}_{in}^\dagger \end{pmatrix} \tag{5.10}$$

Here t is the interaction time between the light fields and the nonlinear crystal. The gain of the parametric amplifier is $G = \cosh(|\eta A_p t|)$. The function of a parametric amplifier is represented by a unitary operator that belongs to a special unitary group $SU(1,1)$:

$$SU(1,1) = \left\{ \begin{pmatrix} \alpha & \overline{\beta} \\ \beta & \overline{\alpha} \end{pmatrix} : \quad \alpha, \beta \in \mathbf{C}, |\alpha|^2 - |\beta|^2 = 1 \right\} \tag{5.11}$$

The input-output relation for the nonlinear interferometer can be obtained by inserting Equation 5.10 into Equation 5.6.

$$\begin{pmatrix} \hat{a}_{out} \\ \hat{b}_{out}^\dagger \end{pmatrix} = \begin{pmatrix} G(\varphi)e^{-i\varphi} & g(\varphi)e^{-i\varphi} \\ \overline{g}(\varphi) & \overline{G}(\varphi) \end{pmatrix} \begin{pmatrix} \hat{a}_{in} \\ \hat{b}_{in}^\dagger \end{pmatrix} \tag{5.12}$$

Here $G(\varphi) = \cosh^2(|\eta A_p t|)e^{i\varphi} + \sinh^2(|\eta A_p t|)$ and $g(\varphi) = \cosh(|\eta A_p t|)\sinh(|\eta A_p t|)(1 + e^{i\varphi})$. The same pump amplitude and interaction time for the two parametric amplifiers is assumed. With a coherent state input at a_{in} and vacuum state input at b_{in}, we can find the output intensity as

$$\langle \hat{b}_{out}^\dagger \hat{b}_{out} \rangle \approx 2G^2 I_{ps}(1 + cos\varphi) \tag{5.13}$$

Here I_{ps} is the same phase sensing intensity as in the linear interferometer. Comparing the output intensity of a nonlinear interferometer in Equation 5.13 with that

in a linear interferometer in Equation 5.8, we see the intensity increases by a factor of $2G^2$. With a homodyne detection scheme (not implemented in the current experiment), the precision of quadrature component measurement can surpass the standard quantum limit by a factor of $2G^2$. With no injection of coherent state input $|\alpha|^2 = 0$, the precision of quadrature component measurement could reach the Heisenberg limit $1/N$ [90].

5.2 Wave-equation Description of Nonlinear Interferometers

From the chapter "Nonlinear Optics," we derived three coupled equations for a general three-wave mixing process, i.e., Equations 2.21, 2.22 and 2.20. In the specific case of parametric amplification process, ω_1, ω_2 and ω_3 are signal, idler and pump fields respectively. Under the condition of strong and undepleted pump field input, we can treat A_3 as a constant and the set of three equations becomes a set of two equations

$$\frac{dA_1}{dx} = \frac{i\chi^{(2)}_{xxx}\omega_1^2}{k_1 c^2} A_3 A_2^* e^{-i\Delta k x} \tag{5.14}$$

$$\frac{dA_2}{dx} = \frac{i\chi^{(2)}_{xxx}\omega_2^2}{k_2 c^2} A_3 A_1^* e^{-i\Delta k x} \tag{5.15}$$

Let us consider the case when the phase matching condition is satisfied, i.e., $\Delta k = 0$. By solving for A_1 and taking the complex conjugate in Equation 5.14 and substituting A_1 into Equation 5.15, we obtain a second order differential equation

$$\frac{d^2 A_2}{dx^2} = \frac{(\chi^{(2)}_{xxx})^2 \omega_1^2 \omega_2^2}{k_1 k_2 c^4} |A_3|^2 A_2 \tag{5.16}$$

By setting the coefficient

$$\frac{(\chi^{(2)}_{xxx})^2 \omega_1^2 \omega_2^2}{k_1 k_2 c^4} |A_3|^2 = \kappa^2, \tag{5.17}$$

the equation simply becomes

$$\frac{d^2A_2}{dx^2} = \kappa^2 A_2. \tag{5.18}$$

The general solution is

$$A_2(x) = C\sinh\kappa x + D\cosh\kappa x \tag{5.19}$$

C and D are constants that are determined by the initial conditions. For arbitrary values of $A_1(0)$ and $A_2(0)$, the solutions to Equation 5.14 and 5.15 are found to be

$$A_1(x) = A_1(0)cosh\kappa x + i(\frac{\omega_1 n_2}{\omega_2 n_1})^{1/2}\frac{A_3^*}{|A_3|}A_2^*(0)\sinh\kappa x \tag{5.20}$$

$$A_2(x) = i(\frac{\omega_2 n_1}{\omega_1 n_2})^{1/2}\frac{A_3^*}{|A_3|}A_1^*(0)\sinh\kappa x + A_2(0)cosh\kappa x \tag{5.21}$$

In the case of no initial input of the idler field

$$A_2(0) = 0, \tag{5.22}$$

the solution becomes

$$A_1(x) = A_1(0)cosh\kappa x \tag{5.23}$$

$$A_2(x) = i(\frac{\omega_2 n_1}{\omega_1 n_2})^{1/2}\frac{A_3^*}{|A_3|}A_1^*(0)\sinh\kappa x \tag{5.24}$$

In the following section of this chapter, we present several experimental implementations of nonlinear interferometers. The first nonlinear interferometer presented consists of a second harmonic generation and parametric down-conversion process. It corresponds to the case of no initial input of the idler field. The second nonlinear interferometer presented consists of two parametric amplifiers, the second of which corresponds to the case of arbitrary initial amplitudes of the signal and idler fields.

5.3 Experiment Implementation and Results

The first nonlinear interferometer is consists of a second-harmonic generator as the first nonlinear beam splitter (NBS) and a parametric down-conversion process as the second NBS. Consider the two illustrations in Figure 5.1. Part (a) is a traditional Mach-Zehnder interferometer. In Part (b), the two beam splitters are replaced by two nonlinear beam splitters (NBS). In general, the Hamiltonian of the nth NBS can be expressed as [88]

$$\hat{H} = \hbar\Omega_n[\hat{a}(\hat{b}^\dagger)^n + \hat{a}^\dagger(\hat{b})^n]. \tag{5.25}$$

Here $\hat{a}$ and $\hat{b}$ are the annihilation operators for the two input modes, and Ω_n is the coupling strength. In the special case of n=1, the NBS becomes a traditional beam splitter, and the interferometer is simply a Mach-Zehnder interferometer. In the case of $n = 2$, the Hamiltonian becomes

$$\hat{H} = \hbar\Omega_2[\hat{a}\hat{b}^\dagger\hat{b}^\dagger + \hat{a}^\dagger\hat{b}\hat{b}]. \tag{5.26}$$

It represents a second harmonic generation or a degenerate-parametric down-conversion process: Two photons at mode $\hat{b}$ are annihilated, while simultaneously one photon at mode $\hat{a}$ is created, or vice versa.

The experiment scheme is sketched in Figure 5.3. Our source laser is a Ti:Sapphire pulsed laser at the wavelength of $800nm$ (the red lines in the scheme). The laser frequency is first doubled (the wavelength is halved) by a nonlinear crystal $KNbO_3$ to $400nm$ (the blue lines in the figure) through an SHG process. The remaining IR and the generated blue beams are divided by a Dichroic Mirror (DM1 in the scheme). On the left segment of the setup, the IR extends down and is split by a beam splitter (BS1). The two split beams propagate in separate paths and recombine at a second beam splitter (BS2). One of the beams undergoes a phase shift generated by a scanning piezoelectric transducer (PZT). A photo-detector (D1) is placed at the output to observe the interference fringe of the recombined fields. This part is a conventional Mach-Zehnder interferometer. On the right side of the setup (inside the

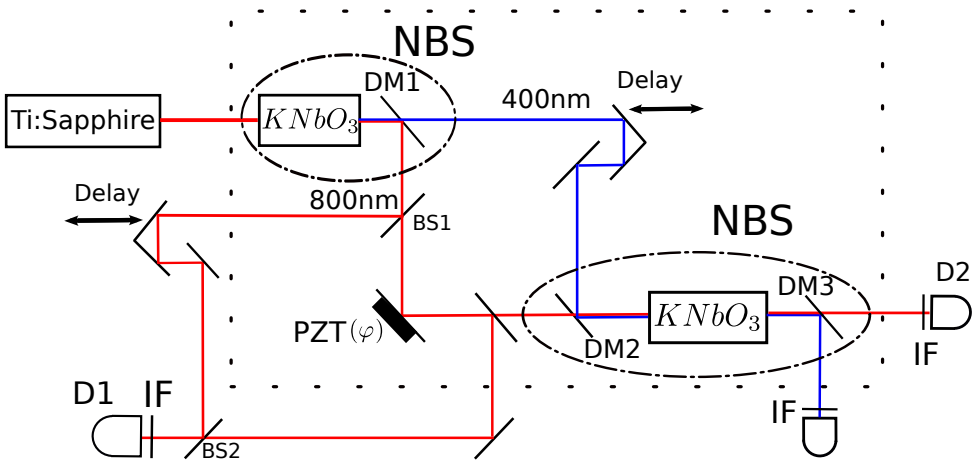

Figure 5.3. Nonlinear interferometer. BS1, BS2: beam splitters. DM1, DM2, DM3: dichroic mirrors. D1,D2: photo-detectors. PZT: piezoelectric transducer. NBS: nonlinear beam splitter. IF: interference filter.

dashed line), the IR and the blue are first divided by a dichroic mirror (DM1) and then recombined by a second dichroic mirror (DM2). Both beams collinearly pass through a second nonlinear crystal $KNbO_3$. The combination of a nonlinear crystal $KNbO_3$ and a dichroic mirror forms a nonlinear beam splitter (NBS) as shown inside the ellipses in the figure. Nonlinear beam splitters function in a way similar to conventional beam splitters. The first NBS splits the incoming IR into two beams: one IR and one blue. The second NBS recombines the two beams. The parts inside the dashed line square form a nonlinear interferometer. A second photo-detector (D2) is placed at the output of the nonlinear interferometer to observe the interference fringe.

The linear interferometer and nonlinear interferometer share a common section in the figure, i.e. the same phase scan (the PZT in the figure). This allows us to compare results from the detectors placed at D1 and D2.

For the linear interferometer, the light intensity received at the D1 detector can be written as

$$I_{D1} = |A_1 + A_2 e^{i\Delta\varphi}|^2 = I_1 + I_2 + 2\sqrt{I_1 I_2}\cos(\alpha + \Delta\varphi) \tag{5.27}$$

Here A_1 and A_2 are the amplitudes of the two electromagnetic fields at the output of the second beam splitter. I_1 and I_2 are the intensities of the two fields. α is a constant that depends on the relative phase between the two fields. $\Delta\varphi$ is the phase shift scanned by the PZT.

For the nonlinear interferometer, the two output amplitudes from the second parametric amplifier are the solutions that can be found in Equation 5.23 and 5.24. Here, we add a phase shift to the term $A_1(0) \rightarrow A_1(0)e^{i\varphi}$ and replace the variable x with a constant length L of the nonlinear crystal. The intensity received at the detector D2 can be written as

$$\begin{aligned} I_{D2} &= |A_1(L) + A_2(L)|^2 \\ &= |A_1(0)e^{i\Delta\varphi}\cosh\kappa L + A_1^*(0)e^{-i\Delta\varphi}\sinh\kappa L|^2 \\ &= I_1 + I_2 + 2\sqrt{I_1 I_2}\cos(\alpha + 2\Delta\varphi) \end{aligned} \tag{5.28}$$

Here $I_1 = |A_1(0)|^2\cosh^2\kappa L$, $I_2 = |A_1(0)|^2\sinh^2\kappa L$. Comparing Equations 5.27 and 5.28, we see a factor of 2 is multiplying the phase shift term $\Delta\varphi$ in Equation 5.28. This means for the same phase scan of $\Delta\varphi$ of the PZT, the nonlinear interferometer would have twice as many fringes and thus is twice as sensitive to the phase measurement. The experimental result is shown in Figure 5.4. The top trace is the applied voltage on PZT, the middle trace is the interference fringe recorded at D1, and the bottom trace is the interference fringe recorded at D2. The interference fringe detected at D1 is from the interferometer with the linear beam splitter ($n = 1$). The interference fringe detected at D2 is from the interferometer with the nonlinear beam splitter ($n = 2$). The experimental results match the theory well. In general, from theory the sensitivity in determining the phase shift can be increased by a factor of n in an n-th nonlinear interferometer [88].

Theoretically, there is no limit to the value of n. However, the nonlinear efficiency dramatically drops as the value of n increases in the experiment.

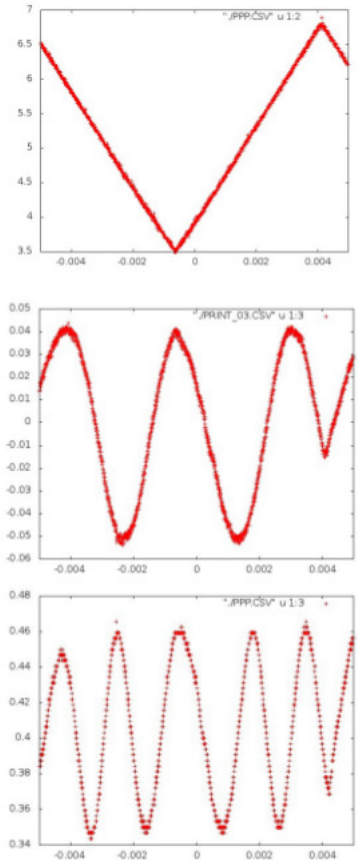

Figure 5.4. Nonlinear interferometer based on a Raman amplifier. The upper trace is the ramp signal from the high voltage applied to the PZT for phase scan. The middle trace is the interference fringe from D1 photo-detector. The bottom trace is the interference fringe from D2 photo-detector.

Such non-conventional interferometers may have applications in other areas such as biochemistry. For instance, some biological samples need to be scanned while avoiding high frequency exposure (such as UV light). By placing the samples on the IR side of the nonlinear interferometer, we can avoid such exposure and still achieve a high sensitivity phase measurement.

Based on the results of the first nonlinear interferometer, we proposed a second nonlinear interferometer experiment. The schematic drawing is shown in Figure 5.5. In this setup, we employ two parametric amplifiers as our nonlinear beam splitters.

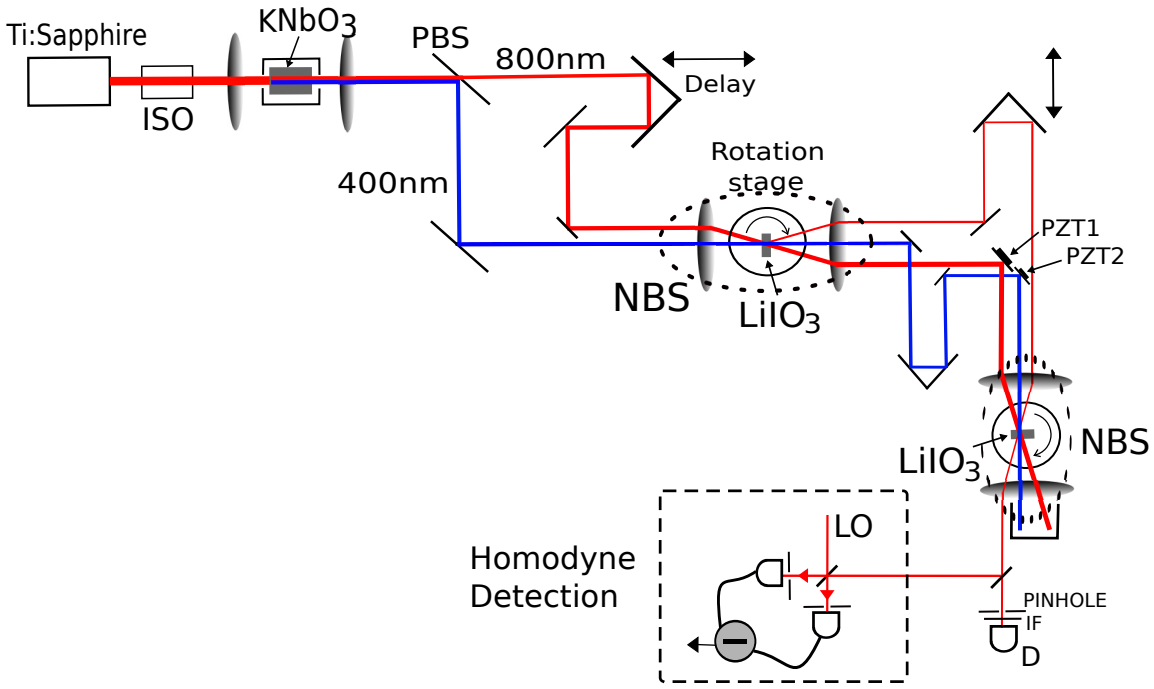

Figure 5.5. A schematic drawing of a nonlinear interferometer that is composed of two parametric amplifiers representing nonlinear beam splitters (NBS). Homodyne detection is used to measure the quadrature-phase amplitudes of the idler field (not implemented in current experiment). ISO: optical isolator. PBS: polarized beam splitter. PZT1,PZT2: piezoelectric transducers. IF: interference filter. D: photo-detector. LO: local Oscillator.

The source laser is a Ti:Sapphire pulse laser at the wavelength of $800nm$ (the red lines in the scheme). The laser frequency is first doubled (the wavelength is halved) by a nonlinear crystal $KNbO_3$ to $400nm$ (the blue lines in the figure) through an SHG process. The remaining IR and the generated blue are separated by a polarizing beam splitter (PBS in the figure).

The nonlinear beam splitters are realized by a noncollinear parametric down-conversion process (inside the ellipses in the figure). To set up the parametric amplification process in the experiment, three steps were taken on each crystal. These three stages are described in detail in the chapter "Frequency Down-conversion For

a Quantum Network." Note that the blue light only plays the role of pump beam. Only the input IR and the generated idler IR are considered as far as the nonlinear interferometer is concerned. These two IRs are first separated by the first NBS and then recombined in the second NBS. A PZT phase scan is applied to the idler field. Nonlinear crystal $LiIO_3$ is used in this experiment. Although its conversion efficiency is not as good as other nonlinear crystals such as $KNbO_3$, its angle tuning phase-matching method is preferred in noncollinear interactions. A photo-detector (D) is placed at the output to observe the interference fringes of the recombined fields.

From the solutions we found out in Equation 5.21, we obtain the intensity at D

$$\begin{aligned} I_D &= |A_2(L)|^2 \\ &= |i\frac{A_3^*}{|A_3|}A_1^*(0)e^{-i\Delta\varphi}\sinh\kappa L + A_2(0)\cosh\kappa L|^2 \\ &= I_1 + I_2 + 2\sqrt{I_1 I_2}\cos(\alpha+\Delta\varphi) \end{aligned} \tag{5.29}$$

Here $I_1 = |A_1(0)|^2\sinh^2\kappa L$, $I_2 = |A_2(0)|^2\cosh^2\kappa L$. α is a constant that depends on the relative phase between the two fields.

We calibrate the two PZTs (PZT1 and PZT2 shown in Figure 5.5) so that they scan the same length. Since $\Delta\varphi = \frac{2\pi\Delta L}{\lambda}$, and $\Delta L = \Delta L'$,$\lambda = 2\lambda'$, we find $\Delta\varphi'$=$2\Delta\varphi$. Here ΔL is the length scan on PZT1, and $\Delta L'$ is the length scan on PZT2. λ is the wavelength of the idler field, λ' is the wavelength of the pump field. $\Delta\varphi$ is the phase scan when PZT1 is used, and $\Delta\varphi'$ is the phase scan when PZT2 is used.

Now instead of scanning the idler field, we scan the pump field. So the phase term $\Delta\varphi'$ would be added to A_3, i.e., $A_3 \to A_3 e^{i\Delta\varphi'}$. The intensity at D then becomes

$$\begin{aligned} I'_D &= |A_2(l)|^2 \\ &= |i\frac{A_3^* e^{-i\Delta\varphi'}}{|A_3|}A_1^*(0)\sinh\kappa l + A_2(0)\cosh\kappa l|^2 \\ &= I_1 + I_2 + 2\sqrt{I_1 I_2}\cos(\alpha-2\Delta\varphi) \end{aligned} \tag{5.30}$$

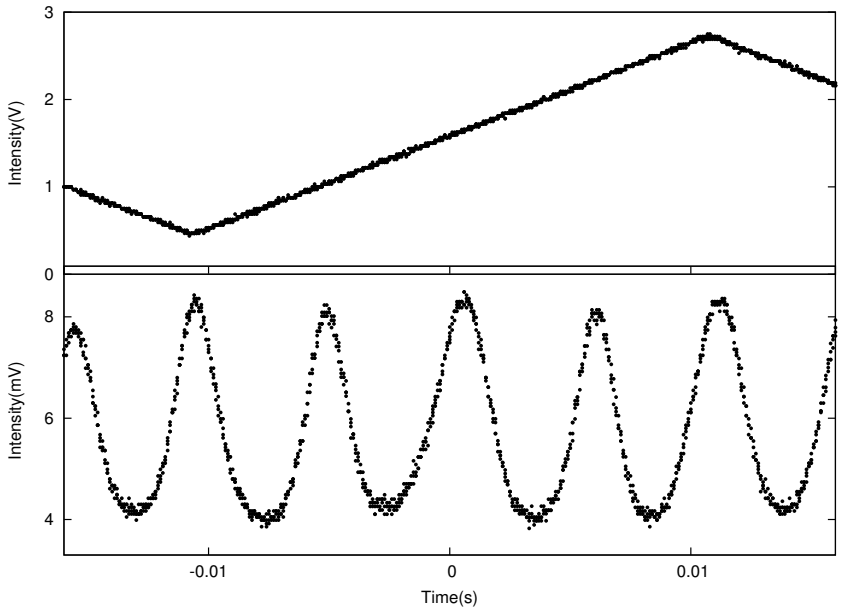

Figure 5.6. An interference fringe is observed when phase scan is applied to the IR mirror. Top trace: Ramp voltage (the output voltage is 1% of the real voltage) applied to PZT. Bottom trace: The signal is aligned to a photo-detector and interference fringes are seen on an oscilloscope.

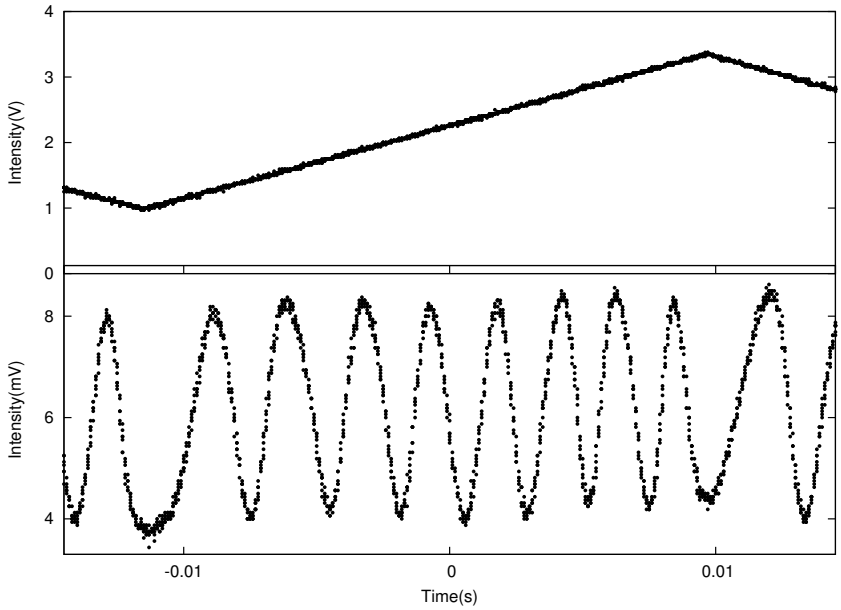

Figure 5.7. Two piezos, PZT1 on the signal field mirror and PZT2 on the pump field mirror, are calibrated to scan the same length. Twice as many as fringes are observed when PZT2 is scanned, compared with that when the scan is on PZT1.

The experimental results are shown in Figure 5.6 and 5.7. Figure 5.6 is a scan of PZT1, and Figure 5.7 is a scan of PZT2. With the same scan length, a scan on the pump field has twice an many fringes compared with a scan on the idler field.

As discussed in the section "Research Background" in this chapter, the precision phase measurement is enhanced by a factor of $2G^2$. In our proof-of-principle experiment, the parametric amplifier factor G is measured at about 1.01 with a strong signal field input. There is some room for improvement on the experimental setup to increase the G factor. First, with a relatively weaker signal field and stronger pump field inputs, the parametric amplification could be improved. However, lowering the power of the signal field may negatively influence the homodyne detection. If the power is low for homodyne detection, the electronic shot noise of the detector may play a bigger role than that of photon signal. Second, the pulse duration of the fields is prolonged significantly during the first SHG process and later transmission through media such as crystals and lenses. A rough measurement of the pulse duration shows that it extends from $100fs$ to more than $1ps$. The extension of the pulse length disperses the power and deteriorates the conversion efficiency inside nonlinear crystals, making the G factor much lower. A group-velocity-dispersion compensation method could be considered to improve the parametric amplifier conversion efficiency [92].

In the nonlinear interferometers discussed so far, two nonlinear beam splitters are used in analogy to the two beam splitters used in Mach-Zehnder interferometer. In contrast to a simple beam splitter, each nonlinear beam splitter such as one with a parametric amplifier adds much complexity to the system. Basically, it would take three stages of operations to find the signal for each parametric amplifier as described in the chapter "Frequency Down-conversion For a Quantum Network." Plus, many degrees of freedom need to be adjusted to optimize the system: time overlap of two pulses on the order of 10^{-13}s, spatial overlap of three beams under one focal lens within 100μm, crystal rotation for best phase matching angle, etc. To simplify the experimental procedure under limited resources, we propose two alternative options for implementing this experiment.

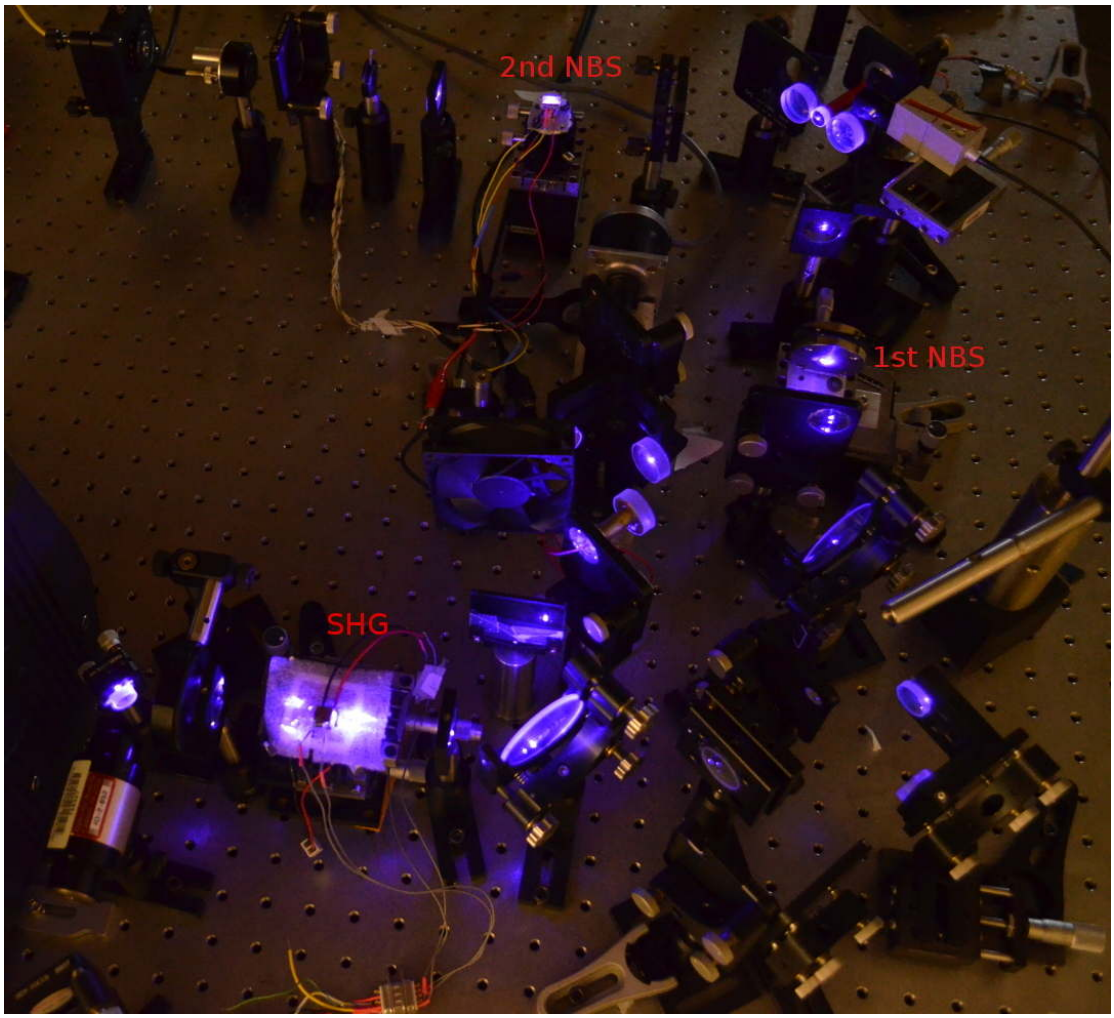

Figure 5.8. A photograph taken above the optical table while the laser is in operation for the implementation of a nonlinear Mach-Zehnder interferometer. SHG: second harmonic generation. NBS: nonlinear beam splitter.

We turn our attention from a Mach-Zehnder interferometer to a Michelson interferometer. Because in a traditional Michelson interferometer, only one beam splitter is used as shown in Figure 5.9 Part (a). The same beam splitter serves both functions of separating and recombining the beams. Following the idea of using a single beam splitter in the Michelson interferometer, we propose a nonlinear interferometer by using only one NBS as shown in Figure 5.9 Part (b).

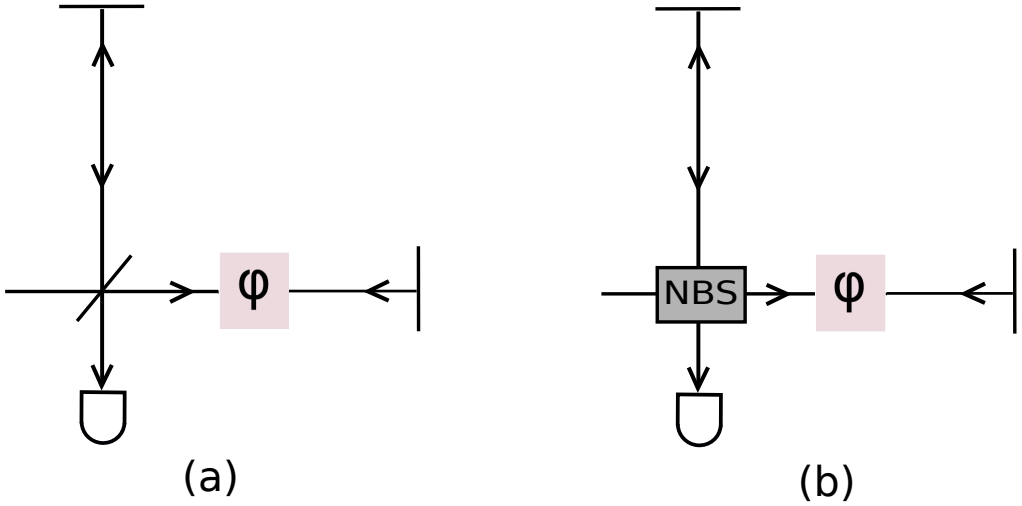

Figure 5.9. In a traditional Michelson interferometer, the same beam splitter is used for both splitting and recombining the beams. Following this idea, we implement a nonlinear interferometer with only one parametric amplifier. It reduces the complexity of the experimental setup.

The schematic figure of a nonlinear Michelson interferometer is shown in Figure 5.10. Instead of using two different parametric amplifier crystals to split and recombine the beams, we only require one crystal for repeated usage. After the beams go through the crystal, mirrors are used to reflect them back into the same crystal. The laser source used in the experiment is a pulse laser at the pulse repetition of $80MHz$ and a simple calculation shows the space separation between two consecutive pulses is $3.75m$. The reflecting mirrors are placed right after the crystal so that the pulses reflected back would have no chance to interfere with the next forward pulse. PZTs are attached to the mirrors reflecting signal and pump fields to scan the phases as shown

in the figure. The same procedure is used as was used for the nonlinear Mach-Zehnder interferometer and we obtained similar results.

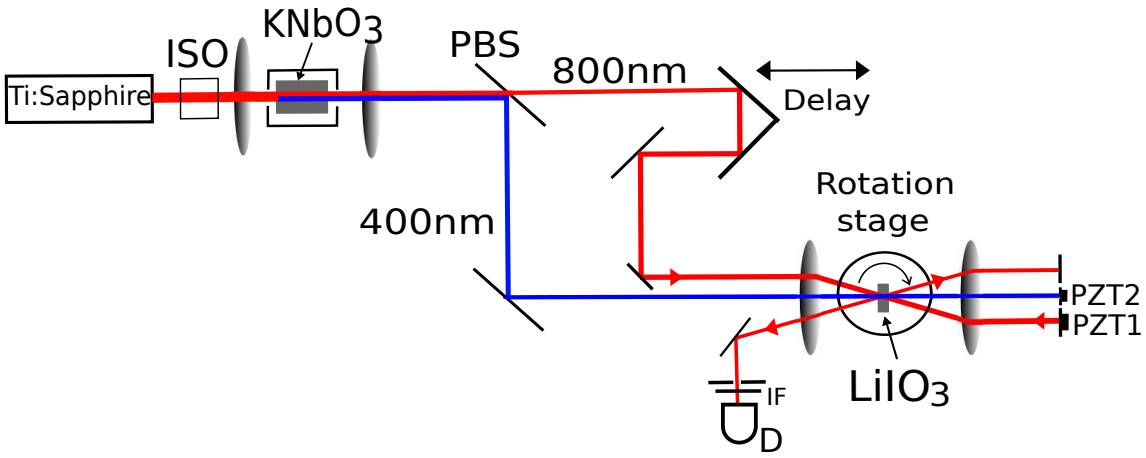

Figure 5.10. A schematic drawing of implementing a nonlinear interferometer with only one parametric amplifier representing a nonlinear beam splitter. The beams are reflected back by three separate flat mirrors and recombined in the same parametric amplifier.

A second alternative option for simplifying the experimental setup is to input the beams collinearly instead of non-collinearly. In previous experiment schemes, the nonlinear interferometer was realized by two parametric amplifiers in a noncollinear manner. The signal field and idler field have the same polarization but different spatial mode. Because the two beams are incident on the crystals with a small angle, they do not interact all the way through the whole length of the crystal. As a result, it would reduce the amplification factor of the parametric amplifier. Alternatively, we may realize a degenerate parametric amplifier by making the idler field and signal field collinear but with perpendicular polarization. We can achieve it by using a type II phase matching crystal (LBO in our lab). A type II phase matching crystal is introduced in the chapter "Frequency Down-conversion For a Quantum Network." The advantage of this method is that it can increase the interaction time of the beams inside the crystal, and thus increase the amplification factor of the parametric amplifier. The amplification increase is crucial, since the phase measurement precision

would increase by a factor of $2G^2$ in the nonlinear interferometer compared with the linear interferometer.

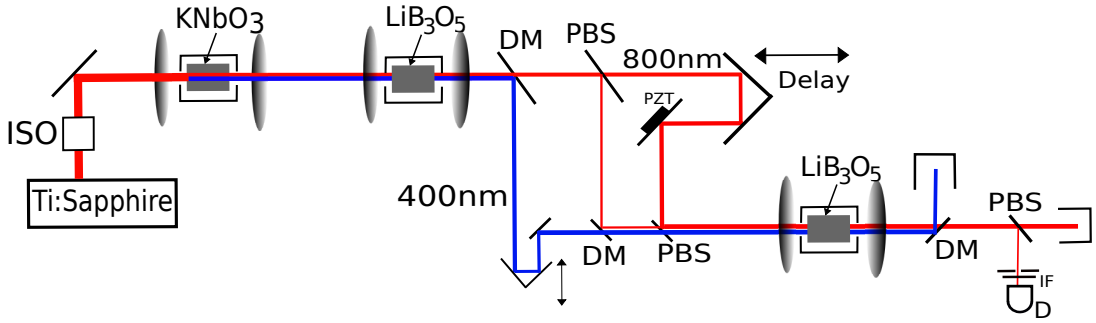

Figure 5.11. A schematic drawing of the implementation of a nonlinear interferometer using type II phase matching crystals. The signal and idler fields spatially overlap but have orthogonal polarizations. This setup could increase the interaction time of the beams and the conversion efficiency. ISO: optical isolator. PBS: polarized beam splitter. DM: dichroic mirror. D: photo-detector.

So far we have proposed the implementation of several nonlinear interferometers. Homodyne detection is not implemented in the current experiment. The most important reason is that the G factor is too small. For a small G factor, a nonlinear interferometer would have little advantage over a linear interferometer in precision phase measurement.

We extend the analysis of nonlinear interferometers from parametric amplifiers to Raman amplifiers. The Raman amplifier experimental setup is described in the chapter "Efficient Raman Conversion." We show here that the efficient Raman conversion experiment can also be interpreted as a nonlinear interferometer. Because the Raman amplifier and the parametric amplifier have the same Hamiltonian (Equation 2.27), they can be treated the same in the setup of a nonlinear inteferometer. The experiment scheme is shown in Figure 5.12, which has many similarities to the layout of Figure 5.10. This nonlinear interferometer can be interpreted as follows: In the first forwarded pass, the W beam is divided into the Stokes field and the atomic spin wave. The atomic spin wave stays in the atomic cell but the Stokes travels out. After

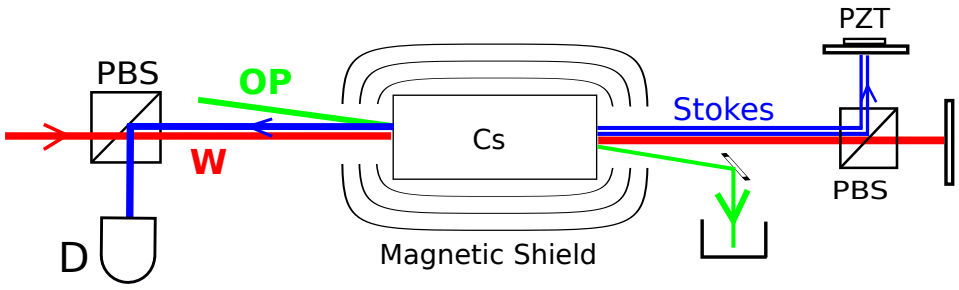

Figure 5.12. Raman conversion can be thought of as a special case of nonlinear interference. The W and Stokes fields are separated by a Raman amplifier and reflected back by two flat mirrors and recombined in the the same Raman amplifier. The Raman amplifier plays the role of a nonlinear beam splitter (NBS), just like the beam splitter in the traditional Michelson interferometer.

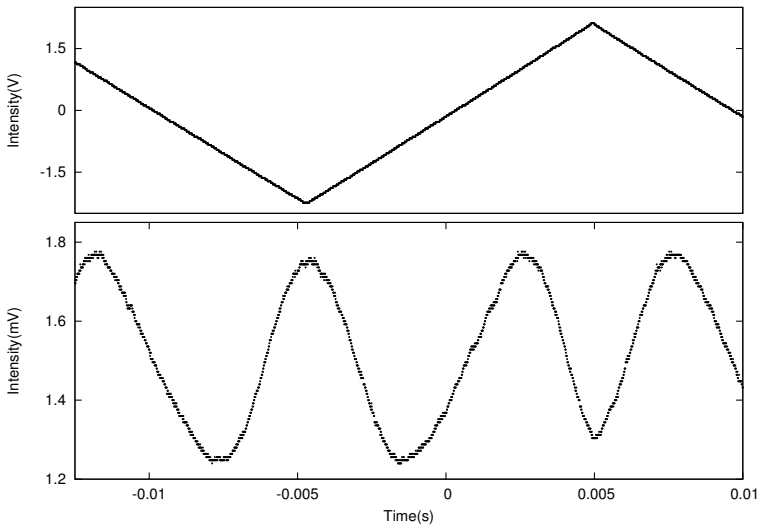

Figure 5.13. The upper trace is the applied ramp voltage. The down trace is the interference fringe from the photo-detector D.

a delay of Δt, both beams are reflected backwards and recombined with the original atomic spin wave that stays in the cell in the same Raman amplifier. Here the Raman amplifier is a NBS and plays the role of beam splitter in a traditional Michelson interferometer. The scan is applied on the PZT attached to the Raman pump mirror. The interference fringes are plotted as shown in Figure 5.13.

The interference can be interpreted as follows: In the first pass of the Raman pump beam, the phase of the Stokes field is anti-correlated with the phase of the atomic spin wave, i.e., $\varphi_s + \varphi_{asw}$=constant [82]. φ_s is the phase of the Stokes field and φ_{asw} is the phase of the atomic spin wave. This relation is the same as the signal field and idler field relation in a parametric down-conversion. After the first pass, the phase information is stored in the atomic spin wave and is later retrieved when the Raman pump beam is reflected back and passes the atoms the second time. This phase information is then carried by the Stokes field generated in the second pass. The Stokes field generated in second pass then interferes with the Stokes field generated in the first pass.

For the time it takes from the first pass to the second pass, the phase of the atomic spin wave is constant if the time is short enough for the atoms to not move appreciably. However, if we apply an external magnetic field to the atomic ensemble, the degenerate energy level will split into sub-levels due to the Zeeman effect. The energy of the system is $E = -\vec{\mu} \cdot \vec{B}$. μ is the magnetic moment of the atom and B is the applied magnetic field. By substituting the energy into the time-dependent Schrödinger equation and solving the equation, we obtain the phase evolution of the atomic spin wave state

$$|\Psi(t)\rangle = e^{-i(\vec{\mu}\cdot\vec{B}/\hbar)t} |\Psi(0)\rangle \tag{5.31}$$

Here $|\Psi(0)\rangle$ is the initial atomic spin wave state. This phase changing phenomenon is similar to the Larmor precession. Larmor precession is a precession of electron or nuclear spin. In the atomic ensemble system, however, an atomic pseudo-spin is the case. The two states $|m\rangle$ and $|g\rangle$ coupled by Raman fields represent the pseudo-spin up state $|\uparrow\rangle$ and pseudo-spin down state $|\downarrow\rangle$, respectively.

Under the condition of an external magnetic field, the spin wave state will evolve. After a delay time Δt when the Raman pump field is reflected back from the flat mirror, the spin wave state has evolved to $e^{-i(\vec{\mu}\cdot\vec{B}/\hbar)\Delta t} |\Psi(0)\rangle$. Because the phase of the Stokes field generated in the second pass has an anti-correlation with the phase of the spin wave, the Stokes field generated in the second pass will shift its phase by $e^{i(\vec{\mu}\cdot\vec{B}/\hbar)\Delta t}$. By superimposing the two Stokes fields onto the photo-detector and changing the applied magnetic field, we expect to detect a shift of the interference fringe.

To create a controllable magnetic field, we wrapped a coil around the glass cell as a solenoid and placed the cell inside the magnetic shielding. The coil was connected to a power supply and an ammeter. The magnetic field can be calculated from the solenoid equation $B = \mu n I$. n is the number of turns per unit length and I is the current. Since the phase change was proportional to the applied magnetic field, we expected to observe a shift of the interference fringe on the oscilloscope as a function

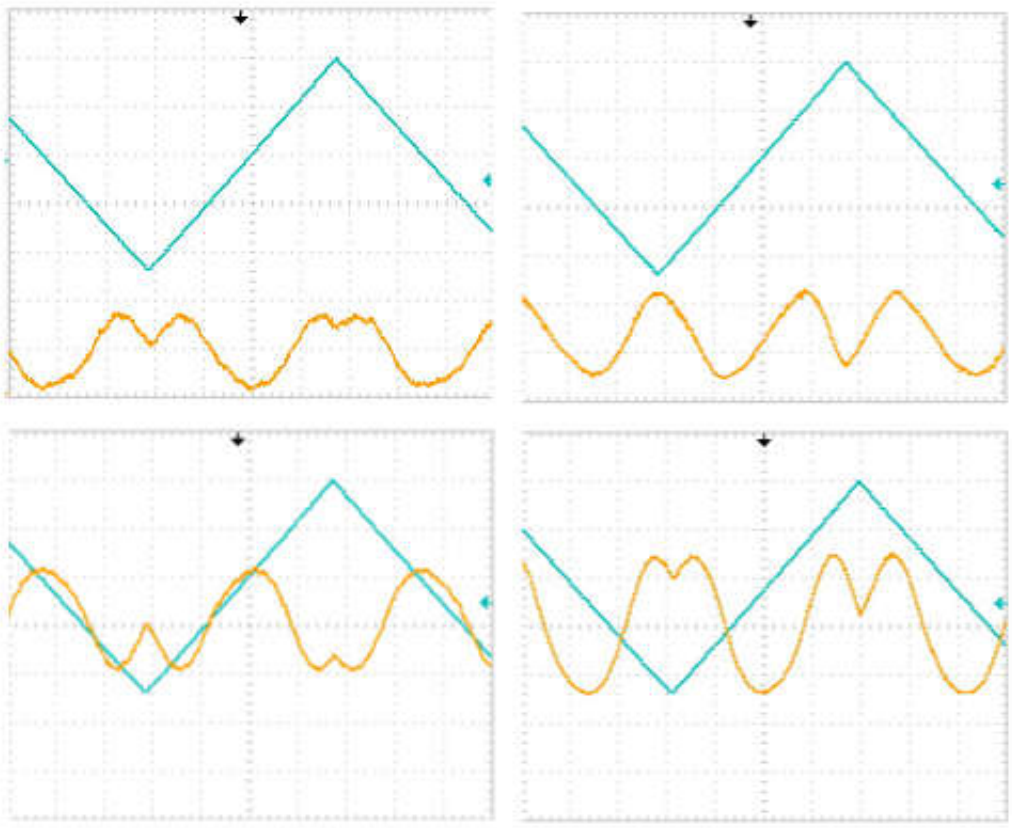

Figure 5.14. Four typical interference fringes monitored on the oscilloscope when four different magnitudes of the magnetic field are applied to the cesium atomic ensemble in the Raman nonlinear interferometer experiment. The blue ramp signals are the applied high voltages on the PZT. The yellow lines are the interference fringes.

of magnitude of the applied magnetic field. Four typical interference fringes detected are shown in Figure 5.14.

We indeed observed the phase changing effect. However, we also observed a dramatic change of the interference intensity and interference visibility, which was unexpected from the theory. This indicates that there are some other physics effects involved in the process. A close examination of each experimental component lead us to believe that the increase of the interference intensity was caused by the Faraday effect. A simple explanation is given as follows: The Raman pump field used in our experiment is a linear polarized beam. In photon language, a linear polarization is

a superposition state of the σ^+ and σ^- polarization states. Under the influence of a magnetic field, σ^+ and σ^- propagate at slightly different speeds and undergo a relative phase shift. This caused the signal to leak out of the PBS that we placed to separate the Stokes field from the Raman pump field. As a result, the signal received at the photo-detector dramatically increased.

Besides the Faraday effect caused by the magnetic field, the number of Zeeman sub-levels is also a concern. The two energy levels coupled to Raman conversion are $6^2S_{1/2}, F = 3$ and $6^2S_{1/2}, F = 4$. Under the influence of the magnetic field, the $F = 3$ state splits into 7 Zeeman sub-levels and the $F = 4$ state splits into 9 Zeeman sub-levels. Cesium has far more Zeeman sub-levels than other alkali atomic systems such as Rubidium and Lithium. This adds extra complexity to the phase measurement because the phase change is different for different pairs of Zeeman sub-levels that are coupled to the Raman conversion.

We suggest that the problems mentioned above can be solved by carefully preparing the initial state in one Zeeman sub-level using a circularly polarized σ^+ optical pump, and using selection rules to limit the the possible Raman transitions, for example, one could use the Raman transition from $F = 4, m_F = 4$ to $F = 3, m_F = 3$. Under optimal conditions, such a Raman nonlinear interferometer could be used as sensitive magnetometers.

As a final note, several thoughts are summarized regarding future nonlinear interferometer experiments: First, for the interferometer to behave optimally a high amplification factor G in the parametric amplifier is required since the interference fringe increases by a factor of $2G^2$ relative to a linear interferometer. To achieve that, a higher power pump laser is required to have stronger nonlinear interactions. Second, it would be of great interest and a potential future task to implement the phase precision measurement on nonlinear interferometers with different input quantum states, such as squeezed states, low intensity coherent states and entangled states. Third, the idea of nonlinear interferometer could be applied to atomic interferometry and may provide potential applications in gravitational wave measurement [91].

6. SUMMARY

In summary, we have demonstrated that, with a strong signal field input, frequency down-conversion from a pump photon to an idler photon can be coherent. Contrary to a common misunderstanding, we showed that the parametric process is free of quantum noise. We implemented an interference experiment to demonstrate that coherence is preserved in the parametric down-conversion process. This could lead to a high-fidelity quantum state transfer from a high-frequency photon to a low-frequency photon and connect a missing link in a quantum network. Three stages of experiment implementation are described in detail. Both Type I and Type II phase matching crystals are tested in order to improve the signal-to-noise ratio. The quantum-noise-free down-conversion process has potential application in a WDM-QKD system to generate superposition state of multiple frequencies.

Efficient Raman conversion up to 30% for Stokes generation is achieved by reflecting back both the Raman pump field and the Stokes field generated in the first passage. The temporal behavior of the Stokes field is presented when both the optical pump and W beams are prepared in a pulsed mode. A laser-like Raman threshold power of less than $1mW$ was found. This low threshold power is attributed to the long coherence time of the generated atomic spin wave. We showed that the Raman conversion efficiency for double passes is increased more than two-fold compared with that for a single pass. This indicates that the two passes are not a simple intensity sum of each pass, but a coherent sum of amplitudes. Analysis of the Raman enhancement mechanism is presented. The beat signal detected between the two generated Stokes fields is attributed to the AC Stark effect. Its Fourier transform to the frequency domain show the frequency difference and the coherence time of the signals.

Finally, we showed several experimental implementations of nonlinear interferometers. The concept of a nonlinear beam splitter was introduced and several non-

linear beam splitters were implemented. Wave-propagation equations of nonlinear interferometers were calculated. We measured the interference fringes of nonlinear interferometers as well as that of traditional interferometers. The experiment results matched the theory. As a potential sensitive magnetometer, a nonlinear interferometer based on a Raman frequency conversion process was analyzed and experimental results were discussed. The idea of nonlinear interferometers can be applied to atomic interferometers and have potential application in gravitational wave detection.

LIST OF REFERENCES

LIST OF REFERENCES

[1] M. A. Nielsen, I. L. Chuang. *Quantum Computation and Quantum Information* (Cambridge Univ. Press, Cambridge, UK, 2000).

[2] V. Giovannetti, S. Lloyd, L. Maccone, Quantum-enhanced measurements: beating the standard quantum limit. Science 306, 1330 (2004).

[3] J. I. Cirac, P. Zoller, H. J. Kimble, and H. Mabuchi. Quantum State Transfer and Entanglement Distribution among Distant Nodes in a Quantum Network. Phys. Rev. Lett. 78, 3221 (1997).

[4] D. Bouwmeester, A. Ekert, A. Zeilinger. *The Physics of Quantum Information* (Springer, Berlin, 2000).

[5] J. Huang and P. Kumar. Observation of quantum frequency conversion. Phys. Rev. Lett. 68, 2153 (1992).

[6] G. Giorgi, P. Mataloni, and F. De Martini. Frequency Hopping in Quantum Interferometry: Efficient Up-Down Conversion for Qubits and Ebits. Phys. Rev. Lett. 90, 027902 (2003).

[7] A. P. VanDevender and P. G. Kwiat, J. Mod. Opt. 51, 1433 (2004).

[8] P. Zoller, *et al.* Quantum information processing and communication: Strategic report on current status, visions and goals for research in Europe. Eur. Phys. J. D 36, 203 (2005).

[9] R. Miller, *et al.* Trapped atoms in cavity QED: coupling quantized light and matter. J. Phys. B. 38, S551 (2005).

[10] L. M. Duan, M. D. Lukin, J. I. Cirac, P. Zoller, Long-distance quantum communication with atomic ensembles and linear optics. Nature 414, 413 (2001).

[11] T. Chaneliere, D. N. Matsukevich, S. D. Jenkins, S.-Y. Lan, T. A. B. Kennedy, A. Kuzmich. Storage and retrieval of single photons transmitted between remote quantum memories. Nature 438, 833 (2005).

[12] D. N. Matsukevich, A. Kuzmich. Quantum state transfer between matter and light. Science 306, 663 (2004).

[13] P. A. Franken, A. E. Hill, C. W. Peters and G. Weinreich. Generation of Optical Harmonics. Phys. Rev. Lett. 7, 118 (1961).

[14] R. W. Terhune, P. D. Maker, and C. M. Savage. Optical Harmonic Generation in Calcite. Phys. Rev. Lett. 8, 404 (1962).

[15] P. D. Maker and R. W. Terhune. Study of Optical Effects Due to an Induced Polarization Third Order in the Electric Field Strength. Phys. Rev. A 137, 801 (1965).

[16] D. A. Steck, "Cesium D Line Data, available online at http://steck.us/alkalidata (revision 2.0.1, 2 May 2008).

[17] C. V. Raman and K. S. Krishnan, "A new type of secondary radiation, Nature 121, 501 (1928).

[18] G. Eckhardt, D. P. Bortfeld and M. Geller. Stimulated Emission of Stokes AND Anti-Stokes Raman Lines from Diamond, Calcite, and Alpha-sulfur Single Crystals. Appl. Phys. Lett. 3, 137 (1963).

[19] N. Bloembergen. The stimulated Raman effect. Am. J. Phys. 35, 989 (1967).

[20] H. Rong, R. Jones, A. Liu, O. Cohen, D. Hak, A. Fang, M. Paniccia. A continuous-wave Raman silicon laser. Nature 433, 725 (2005).

[21] D. J. Gardiner. *Practical Raman spectroscopy* (Springer-Verlag, 1989).

[22] Mark Kasevich and Steven Chu. Atomic interferometry using stimulated Raman transitions. Phys. Rev. Lett. 67, 181 (1991).

[23] L. Ricci, M. Weidemller, T. Esslinger, A. Hemmerich, C. Zimmermann, V. Vuletic, W. Knig, T. W. Hnsch. A compact grating-stabilized diode laser system for atomic physics. Optics Communications 117, 541 (1995).

[24] C. J. Hawthorn, K. P. Weber, and R. E. Scholtena. Littrow configuration tunable external cavity diode laser with fixed direction output beam. Rev. Sci. Instrum. 72, 4477 (2001)

[25] James M. Supplee, Edward A. Whittaker, and Wilfried Lenth. Theoretical description of frequency modulation and wavelength modulation spectroscopy. Appl. Opt. 33, 6294 (1994)

[26] E. Inbar, V. Mahal, and A. Arie. Frequency stabilization of nd:yag lasers to $^{133}Cs_2$ sub-doppler lines near 1064 nm. J. Opt. Soc. Am. B, 13, 1598 (1996)

[27] N. Gisin, G. G. Ribordy, W. Tittel, and H. Zbinden. Quantum cryptography. Rev. Mod. Phys. 74, 145 (2002).

[28] C. H. van der Wal, M. D. Eisaman, A. Andre, R. L. Walsworth, D. F. Phillips, A. S. Zibrov, M. D. Lukin. Atomic Memory for Correlated Photon States. Science 301, 196 (2003)

[29] X.-H. Bao, X.-F. Xu, Z. S. Yuan, C.-Y. Lu, and J.W. Pan. Quantum teleportation between remote atomic-ensemble quantum memories. Proc. Natl. Acad. Sci. U.S.A. 109, 20347 (2012)

[30] M. D. Eisaman, L. Childress, A. Andr, F. Massou, A. S. Zibrov, and M. D. Lukin. Shaping Quantum Pulses of Light Via Coherent Atomic Memory. Phys. Rev. Lett. 93, 233602 (2004)

[31] J. Simon, H. TanJI, J. K. Thompson, and V. Vuletic. Interfacing Collective Atomic Excitations and Single Photons. Phys. Rev. Lett. 98, 183601 (2007).

[32] Bao, X.-H, Reingruber, A, Dietrich, P, Rui, J, Duck, A, Strassel, T, Li, L, Liu, N. L, Zhao,B, Pan, J.-W. Nature Phys. 8, 517 (2012).

[33] C. H. Yuan, L. Q. Chen, J. Jing, Z. Y. Ou, and W. P. Zhang. Coherently enhanced Raman scattering in atomic vapor. Phys. Rev. A 82, 013817 (2010).

[34] L. Q. Chen, G. W. Zhang, C. H. Yuan, J. Jing, Z. Y. Ou, and W. P. Zhang. Enhanced Raman scattering by spatially distributed atomic coherence. Appl. Phys. Lett. 95, 041115 (2009).

[35] P. Berman, *Cavity Quantum Electrodynamics* (Academic, San Diego, 1994).

[36] T. Wilk, S.C. Webster, A. Kuhn, G. Rempe. Single-atom single-photon quantum interface. Science 317, 488 (2007).

[37] E. E. Mikhailov, Y. V. Rostovtsev and G. R. Welch. Group velocity study in hot ^{87}Rb vapour with buffer gas Journal of Modern Optics, 50, 2645 (2003).

[38] S. Brandt, A. Nagel, R. Wynands, and D. Meschede. Buffer-gas-induced linewidth reduction of coherent dark resonances to below 50 hz. Phys. Rev. A 56, R1063 (1997).

[39] F. Couny, F. Benabid, and P. S. Light. Subwatt Threshold cw Raman Fiber-Gas Laser Based on H_2-Filled Hollow-Core Photonic Crystal Fiber. Phys. Rev. Lett. 99, 143903 (2007).

[40] Kai Zhang, Jinxian Guo, Chun-Hua Yuan, L. Q. Chen, Chengling Bian, Bing Chen, Z. Y. Ou, and Weiping Zhang. Mirrorless parametric oscillation in an atomic Raman process. Phys. Rev. A 89, 063826 (2014).

[41] L. Allen and J. H. Eberly, *Optical Resonance and Two-Level Atoms* (Dover: New York, 1987).

[42] R. H. Dicke. Coherence in spontaneous radiation processes. Phys. Rev. 93, 99 (1954).

[43] Y. O. Dudin, L. Li, F. Bariani, A. Kuzmich. Observation of Many-body Rabi Oscillations. Nature Physics 8, 790 (2012).

[44] M. Fleischhauer, A.Imamoglu, J.P. Marangos. Electromagnetically induced transparency:optics in coherent media. Rev. Mod. Phys. 77, 633 (2005).

[45] Maneesh Jain, Hui Xia, G. Y. Yin, A. J. Merriam, and S. E. Harris. Efficient Nonlinear Frequency Conversion with Maximal Atomic Coherence. Phys. Rev. Lett. 77, 4326 (1996).

[46] A. J. Merriam, S. J. Sharpe, M. Shverdin, D. Manuszak, G.Y. Yin, and S. E. Harris. Efficient Nonlinear Frequency Conversion in an All-Resonant Double-Δ System. Phys. Rev. Lett. 84, 5308 (2000).

[47] L. Q. Chen, G. W. Zhang, C. H. Yuan, J. Jing, Z. Y. Ou, and W. P. Zhang. Enhanced Raman scattering by spatially distributed atomic coherence. Appl. Phys. Lett. 95, 041115 (2009)

[48] M. A. Bouchiat and J. Brossel. Relaxation of Optically Pumped Rb Atoms on Paraffin-Coated Walls. Phys. Rev. 147, 41 (1966).

[49] L.Q. Chen, Guo-Wan Zhang, Cheng-ling Bian, Chun-hua Yuan, Z.Y. Ou, and Weiping Zhang. Observation of the Rabi Oscillation of Light Driven by an Atomic Spin Wave. Phys. Rev. Lett. 105, 133603 (2010).

[50] Chun-Hua Yuan, L.Q. Chen, Z.Y. Ou, and Weiping Zhang. Correlation-enhanced phase-sensitive Raman scattering in atomic vapors. Phys. Rev. A 87,053835 (2013).

[51] J. I. Cirac, P. Zoller, H. J. Kimble, and H. Mabuchi. Quantum State Transfer and Entanglement Distribution among Distant Nodes in a Quantum Network. Phys. Rev. Lett. 78, 3221 (1997).

[52] A. D. Boozer, A. Boca, R. Miller, T. E. Northup, and H. J. Kimble. Reversible State Transfer between Light and a Single Trapped Atom. Phys. Rev. Lett. 98, 193601 (2007).

[53] K. C. Kao and G. A. Hockham. Dielectric-fibre surface waveguides for optical frequencies. Proc. IEEE 113, 1151 (1966).

[54] F. Zernike, J.E. Midwinter. *Applied Nonlinear optics* (Dover Publications, 2006).

[55] Y. R. Shen. *Principles of Nonlinear Optics* (Wiley, 1984).

[56] R. W. Boyd, *Nonlinear Optics,Third Edition* (Academic press,2008).

[57] L. Mandel and E. Wolf. *Optical Coherence and Quantum Optics* (Cambridge University Press, New York, 1995).

[58] W. H. Louisell, A. Yariv, and A. E. Siegman. Quantum Fluctuations and Noise in Parametric Processes. Phys. Rev. A 124, 1646 (1961).

[59] R. Loudon, *The quantum theory of light* (Oxford University Press,Oxford,1978).

[60] Z.Y. Jeff Ou, *Multi-Photon Quantum Interference* (Springer,2007)

[61] A. Kuzmich, W. P. Bowen, A. D. Boozer, A. Boca, C. W.Chou, L.-M. Duan, and H. J. Kimble. Generation of nonclassical photon pairs for scalable quantum communication with atomic ensembles. Nature 423, 731 (2003).

[62] M. Fleischhauer and M. D. Lukin. Dark-State Polaritons in Electromagnetically Induced Transparency. Phys. Rev. Lett. 84, 5094 (2000).

[63] D. F. Phillips, A. Fleischhauer, A. Mair, R. L. Walsworth, and M. D. Lukin. Storage of Light in Atomic Vapor. Phys. Rev. Lett. 86, 783 (2001).

[64] A. Mair, J. Hager, D. F. Phillips, R. L. Walsworth, and M. D. Lukin. Phase coherence and control of stored photonic information. Phys. Rev. A 65, 031802(R) (2002).

[65] K. S. Choi, H. Deng, J. Laurat, and H. J. Kimble. Mapping photonic entanglement into and out of a quantum memory. Nature 452, 67 (2008).

[66] C. Liu, Z. Dutton, C. H. Behroozi, and L. V. Hau. Observation of coherent optical information storage in an atomic medium using halted light pulses. Nature 409, 490 (2001).

[67] A. V. Turukhin, V. S. Sudarshanam, M. S. Shahriar, J. A.Musser, B. S. Ham, and P. R. Hemmer. Observation of Ultraslow and Stored Light Pulses in a Solid. Phys. Rev. Lett. 88, 023602 (2001).

[68] Y. Ding and Z. Y. Ou. Frequency downconversion for a quantum network. Opt. Lett. 35, 2591 (2010)

[69] M. A. Albota and F. N. C. Wong. High efficiency single photon detection via frequency up-conversion. Opt. Lett. 29, 1449 (2004).

[70] U. Leonhardt. Quantum statistics of a lossless beam splitter: SU(2) symmetry in phase space. Phys. Rev. A. 48, 3265 (1993).

[71] R. V. Roussev, C. Langrock, J. R. Kurz, and M. M. Fejer. Periodically poled lithium niobate waveguide sum-frequency generator for efficient single-photon detection at communication wavelengths. Opt. Lett. 29, 1518 (2004).

[72] S. Tanzilli, W. Tittel, M. Halder, O. Alibart, P. Baldi, N. Gisin, and H. Zbinden. A photonic quantum information interface. Nature 437, 116 (2005).

[73] R. A. Campos, B. E. A. Saleh, and M. C. Teich. Quantum-mechanical lossless beam splitter: SU(2) symmetry and photon statistics. Phys. Rev. A 40, 1371 (1989).

[74] C. M. Caves. Quantum-mechanical noise in an interferometer. Phys. Rev. D 23, 1693 (1981).

[75] M. Xiao, L. A. Wu, and H. J. Kimble. Precision measurement beyond the shot-noise limit. Phys. Rev. Lett. 59, 278 (1987).

[76] S. M. Barnett, C. Fabre, A. Maitre. Ultimate quantum limits for resolution of beam displacements. Eur. Phys. J. D 22, 513 (2003).

[77] H. P. Yuen and V. W. S. Chan. Noise in homodyne and heterodyne detection. Opt. Lett. 8, 177 (1983).

[78] J. P. Dowling. Correlated input-port, matter-wave interferometer: Quantum-noise limits to the atom-laser gyroscope. Phys. Rev. A 57, 4736 (1998).

[79] P. Kok, H. Lee, and J. P. Dowling. Creation of large-photon-number path entanglement conditioned on photodetection. Phys. Rev. A 65, 052104 (2002).

[80] I. Afek, O. Ambar and Y. Silberberg. High-NOON States by Mixing Quantum and Classical Light. Science 328, 879 (2010).

[81] Y. Israel, I. Afek, S. Rosen, O. Ambar, and Y. Silberberg. Experimental tomography of NOON states with large photon numbers. Phys. Rev. A 85, 022115 (2012).

[82] C. L. Bian, L. Q. Chen, G. W. Zhang, Z. Y. Ou and W. P. Zhang. Retrieval of phase memory in two independent atomic ensembles by Raman process. EPL, 97, 34005 (2012).

[83] A. A. Michelson and E. W. Morley. On the Relative Motion of the Earth and the Luminiferous Ether. Am. J. Sci. 34, 333(1887).

[84] N. Margolus, L. B. Levitin. The maximum speed of dynamical evolution. Physica D 120, 188 (1998).

[85] B. Yurke, S. L. McCall, and J. R. Klauder. SU(2) and SU(1,1) interferometers. Phys. Rev. A 33, 4033 (1986).

[86] B. Yurke, S. L. McCall, and J. R. Klauder. Creation of large-photon-number path entanglement conditioned on photodetection. Phys.Rev. A 65, 052104 (2002).

[87] Z. Y. Ou. Fundamental quantum limit in precision phase measurement. Phys. Rev. A 55,2598 (1997).

[88] D. Leibfried, B. DeMarco, V. Meyer, M. Rowe, A. Ben-Kish, J.Britton, W.M. Itano, B. Jelenkovic, C. Langer, T. Rosenband, and D.J. Wineland. Trapped-Ion Quantum Simulator: Experimental Application to Nonlinear Interferometers. Phys. Rev. Lett. 89, 247901 (2002).

[89] M.D. Reid. Demonstration of the Einstein-Podolsky-Rosen paradox using non-degenerate parametric amplification. Phys. Rev. A 40 913 (1989).

[90] Z. Y. Ou. Enhancement of the phase-measurement sensitivity beyond the standard quantum limit by a nonlinear interferometer. Phys. Rev. A 85,023815 (2012).

[91] A.D.Cronin, J.Schmiedmayer, D.E. Prichard. Optics and interferometry with atoms and molecules. Rev. Mod. Phys. 81, 1051 (2009).

[92] F. Wagner, M. Feuerhake, P. Simon. Group-velocity-dispersion-compensated femtosecond optical parametric amplifier. Optical and Quantum Electronics 29,811 (1997).

VITA

VITA

Name: Yu Ding

Email: ding2@iupui.edu

Education

- Ph.D., Physics, Purdue University, December 2014.
- M.S., Physics, Purdue University, June 2008.
- B.S., Physics, Zhejiang Uninversity, P.R. China, June 2006.

Awards

- Research Investment Fund Fellowship in Purdue University, 2006-2007
- Outstanding Teaching Assistant of The Year by American Association of Physics Teachers (AAPT)

Teaching Experience

- Laboratory Teaching Assistant (2007-2013).
- Joined the Upward Bound program by United States Department of Education to help perspective first-generation college students from low income families (2009-2011)
- Math Tutoring at University College Bepko Learning Center (2012)
- Physics General Tutoring (2013)
- Recitation Teaching Assistant (2014)

Publication

- Yu Ding and Z. Y. Ou. Frequency down-conversion for a quantum network. Opt. Lett. 35, 2591 (2010).